UNIVERSITY OF CALIFORNIA

Santa Barbara

Design and Optimization of Phased-Array Metasurfaces for Applications in Light Emission and Quantum Optics

A dissertation submitted in partial satisfaction

of the requirements for the degree

Doctor of Philosophy

in

Materials

by

Larry K. Heki

Committee in charge:

Professor Jon A. Schuller, Co-Chair

Professor Michael L. Chabinyc, Co-Chair

Professor John W. Harter

Professor Steven P. DenBaars

March 2024

The dissertation of Larry K. Heki is approved.

_____

John W. Harter

_____

Steven P. DenBaars

_____

Michael L. Chabinyc, Co-Chair

_____

Jon A. Schuller, Co-Chair

February 2024

Design and Optimization of Phased-Array Metasurfaces for Applications in Light Emission and Quantum Optics

by

Larry K. Heki

For Megan

ACKNOWLEDGEMENTS

I would like to thank everyone who has made this possible. I recognize that this section can never exhaustively acknowledge all of you. I apologize for the unintentional slight. In an effort to make amends, I hope that I can be more mindful of you in the future.

Thank you, Megan. You have been a bright spot in an often-dreary world. You have helped me more than I knew was possible. It makes all the difference to have someone be happy that you came home. You are so smart and incredibly capable. Thank you for being the first pass for most of my ideas. Marrying you was the best decision of my life.

I would also like to thank my parents: Scott and Charlotte, and my siblings: Hayden, Eric, Aaron, Daniel, Christine, Brandon, and Amber. You all, more than anyone, are foundational to my view of self. Thank you for shaping me and lending me an ear during the difficult times.

Thank you, Jon. You have given me the freedom and opportunity to explore and experiment. No matter the problem I brought you, you had useful ideas for next steps. You have helped me refine my thinking.

I also want to thank my lab mates: Ryan, Yahya, Roark, Zihad, Kumar, and Wesley. Some of you trained me, some of you let me train you. All of you listened to and helpfully critiqued my ideas. I am a better scientist because of you. Yahya and Roark, thank you for your collaboration on many of my projects.

Speaking of collaborators, thank you Jake, Alejandro, and Andrie. The samples you provided were critical. The expertise you shared with me was equally valuable. I wouldn't be where I am without our conversations about growth defects, metasurface applications,

and atom trapping.

Curriculum Vitæ

Larry K. Heki

Education

2024	Ph.D. in Materials (Expected), University of California, Santa Barbara
2018	B.S. in Chemistry, Brigham Young University

Awards/Honors

2018	*Magna cum laude,* Brigham Young University
2016-2018	Undergraduate Research Award, 8 semesters total, Brigham Young University
2012-2016	Dean's List, 4 semesters, Brigham Young University
2012-2018	Brigham Young Scholarship recipient, 5 years total, Brigham Young University

Leadership/Teaching/Mentorship

2021-2023	Trained and mentored 1 undergraduate researcher and 3 graduate researchers, University of California, Santa Barbara
2019	Teaching Assistant, 1 course, University of California, Santa Barbara
2017-2018	President of the student chapter of the American Chemical Society, Brigham Young University
2016-2018	Trained 3 fellow undergraduate researchers, Brigham Young University
2015-2018	Teaching Assistant, 5 courses, Brigham Young University

First and Co-first Author Publications

Heki, L. K., Mohtashami, Y., Chao, R., Isichenko, A., Chauhan, N., Blumenthal, D., & Schuller, J. A. (2022). High Efficiency Large Angle Retroreflecting Metasurface for Magneto-Optical Traps. *In Preparation*.

Heki, L. K., Mohtashami, Y., Chao, R., Ewing, J. J., Quevedo, A., Nakamura, S., DenBaars, S. P., & Schuller, J. A. (2024). Optimizing Polarization Selective Unidirectional Photoluminescence from Phased-Array Metasurfaces. *Advanced Optical Materials,* 2303186.

Heki, L. K., Mohtashami, Y., DeCrescent, R. A., Alhassan, A., Nakamura, S., DenBaars, S. P., & Schuller, J. A. (2022). Designing Highly Directional Luminescent Phased-Array Metasurfaces with Reciprocity-Based Simulations. *ACS Omega*, *7*(26), 22477-22483.

Valdivia-Berroeta, G. A., Heki, L. K., McMurray, E. A., Foote, L. A., Nazari, S. H., Serafin, L. Y., ... & Johnson, J. A. (2018). Alkynyl pyridinium crystals for terahertz generation. *Advanced Optical Materials*, *6*(21), 1800383.

Valdivia-Berroeta, G. A., Heki, L. K., Jackson, E. W., Tangen, I. C., Bahr, C. B., Smith, S. J., ... & Johnson, J. A. (2019). Terahertz generation and optical characteristics of P-BI. *Optics Letters*, *44*(17), 4279-4282.

Conference Presentations

Inverse Design of High Efficiency Large Angle Polarization Insensitive Retroreflecting Metasurface for Magneto-Optical Traps. *CLEO: Fundamental Science*, (2023, May)

Numerical Prediction of Unidirectional Luminescence from Light-Emitting Metasurfaces. *Metamaterials 2021,* (2021, September)

Organic crystals for THz generation. *ACS Spring Meeting,* (2018, March).

Abstract

Design and Optimization of Phased-Array Metasurfaces for Applications in Light Emission and Quantum Optics

by

Larry K. Heki

Phased-array metasurfaces offer a wide design space to arbitrarily shape the wavefront of light. As such, metasurfaces have been used to create various miniature and light-weight optical components such as lenses and beam steerers with applications ranging from augmented reality to space flight and LiDAR. Metasurface optical elements typically transform a well-defined incident light beam into a desired output waveform. Luminescent emission, on the other hand, is not well-defined in either space or momentum. Thus, light emitting metasurfaces offer intriguing opportunities to study fundamental light-matter interactions and further miniaturize optical components. To date, most luminescent metasurfaces have been uniform arrays of scatterers and are therefore unable to provide granular control over the wavefront of emitted light. Recent work demonstrating wavefront control of spontaneous emission using phased-array metasurfaces, on the other hand, suffer low efficiency and peculiar polarization dependencies.

In this work, we develop and verify a reciprocal simulation strategy to explain the polarization disparity and improve unidirectional emission efficiency of phased-array metasurfaces. We then use these reciprocal simulations to design metasurfaces to steer light from systems where emission originates from alternate quantum mechanical processes. Additionally, we pair these reciprocal simulations with Bayesian optimization to facilitate the

design of highly unidirectional photoluminescent metasurfaces capable of directive p-, s-, or combined p- and s- polarized emission at arbitrary angles. Our inverse design approach enables 54% improvement in directivity and the first-ever simultaneous directional emission of s- and p-polarized light.

We expand the optimization tools developed for light emitting metasurface and apply them to quantum optics. Magneto-optical atomic traps are a critical part of modern science, but future applications in gravity mapping and space-based atomic clocks require smaller, more robust traps. We design a metasurface retroreflector to replace two bulk optical components and eventually reduce trap volume by three orders of magnitude. The metasurface is designed for polarization insensitive retroreflection of 780 nm circularly polarized light at 54.7°. The proof-of-concept device retroreflects circularly polarized 736 nm light at 50.3°. We discuss oxidation mitigation strategies for future devices and propose a corrective optic for the currently fabricated device.

With a better understanding of light-matter interactions and sophisticated modeling and optimization tools, this work represents a step toward smaller, more efficient devices. Full control over the polarization and momentum of light emitted by incoherent sources will lead to lighter, more energy efficient displays whereas the miniaturization of magneto-optical traps will allow the expansion of cold-atom science beyond the laboratory.

Contents

Chapter 1: Introduction

In the most general sense, a metasurface is a collection of subwavelength elements on some substrate with the purpose of transforming incident or emitted light. Metasurfaces can operate in transmission, reflection, or emission mode to steer, focus, or change the angular momentum of light. Metasurfaces have been applied to imaging[1,2], holography[3,4], vortex beam generation[5,6], and invisibility cloaking[7,8], among others[9–15]. We can imagine metasurfaces as a technology platform to allow arbitrary manipulation of light. Control is granted by judicious placement of appropriate metaelements.

In the most easily visualized case, an array of identical metaelements or scatterers can be arranged on a square lattice. The properties of this scatterer (refractive index, size, shape, etc.) can be carefully tuned such that the electric and magnetic multipole modes overlap, resulting in suppression of back reflection. This type of metasurface would function as an anti-reflective coating[16,17], similar to what could be produced with a quarter-wavelength thick film of appropriate refractive index.

A slightly more complex metasurface geometry, i.e. a phased-array, allows for a more useful optical component. Consider an optical wedge as used to steer light. The conventional bulk optic is usually made of glass where one face has been ground such that there is a small angle between the two faces (exaggerated in Figure 1.1). Refraction at the non-normal face causes deflection of the beam, i.e. beam steering. On a microscopic level, the wedge functions by controlling the phase of transmitted light. Light that transmits through a thicker region of glass acquires more transmission phase, and, over some characteristic distance, the phase varies linearly between 0 and 2π. When this spatially varying wavefront is transmitted into

air, the beam deflects. Similar functionality can be achieved with a phased-array metasurface[18].

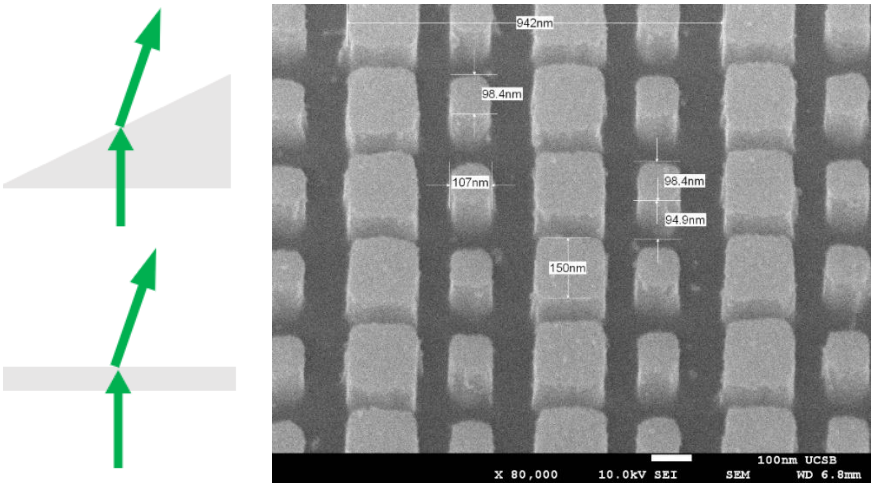

Figure 1.1: (top left) A schematic representation of an optical wedge steering incident light. (bottom left) A schematic representation of a phased-array metasurface steering incident light. (right) An off-axis scanning electron micrograph (SEM) of a phased-array metasurface. The metasurface is composed of a repeating unit cell of two square prims.

In a phased-array metasurface, we replace the transmission phase through bulk material with transmission phase through the various metaelements. Consider nanopillars of varying widths on a fixed period (such that the fill fraction varies from 0 to 1). The effective medium approximation tells us that as nanopillar width increases (fill fraction increases), the effective index increases and more transmission phase is acquired. Assuming sufficiently tall nanopillars are used, transmission phase can be varied between 0 and 2π for a given set of pillar widths. (Such phase coverage can also be achieved by detuning from a Mei-like resonance of shorter pillars.) The 2π phase coverage granted by varying nanopillar width is functionally identical to the 2π phase coverage granted by varying the thickness of a bulk optic.

Metaelements of appropriate width are then placed over a characteristic distance. For the sake of illustration, the smaller element in Figure 1.1 (right) adds π transmission phase,

whereas the larger element adds 2π transmission phase. Formally, the metaelements are arranged such that the transmission phase, φ, is a linear function of lateral position, x: $\varphi(x) = \frac{2\pi}{\Delta}x$, where Δ is the metasurface period. Alternatively, a beam steering metasurface imparts metasurface momentum, $k_M = \frac{d\varphi}{dx} = \frac{2\pi}{\Delta}$, and arbitrary final momentum can be achieved according to: $k_{||,f} = k_{||,i} + k_M$, where $k_{||,f/i}$ is the final/initial transverse momentum.

Each optical component requires its own metaelement arrangement. For example, a half (quarter) waveplate can be achieved using an array of identical scatterers that delay x-polarized light π ($\pi/2$) more than y polarized light[19], similar to a birefringent crystal. A vortex beam can be generated by arranging metaelements such that $\varphi_{VB}(x,y) = l\,\Phi = l\,\mathrm{atan}(y/x)$, where x, y are the coordinates of the metaelement, l is the desired orbital angular momentum, and Φ is the azimuthal angle[20]. A metalens employs a hyperbolic phase profile: $\varphi_L(x,y) = \frac{2\pi}{\lambda_o}\left(f - \sqrt{f^2 + (x^2+y^2)}\right)$, where f is the desired focal length of the lens. An axicon[21] of angle θ requires $\varphi_A(x,y) = \frac{2\pi}{\lambda_o}\sqrt{x^2+y^2}\sin(\theta)$.

It is worth noting that the decades of work in this field have resulted in many variations on these general concepts. Some applications, e.g. wearables, demand a nonplanar substrate and conformal metasurfaces[22,23]. Some require no substate at all, replacing metaelements with nanoholes[24]. Some utilize geometric phase, as opposed to transmission phase[25,26]. As discussed above, transmission phase is accumulated by propagation through differently shaped metaelements. Geometric phase, i.e. Pancharatnam-Berry phase, on the other hand, is accumulated by propagating light through a birefringent metaelement at different orientations[27,28]. This has the advantage of constant amplitude across the metasurface, as the shape and size of the metaelement does not need to change in a geometric phase structure like

they must in a transmission phase structure. Thus, Pancharatnam-Berry phase metasurfaces often have very high efficiency. Many excellent reviews exist to detail the various applications and types of metasurfaces[9–14,29–36].

With a thorough overview of 'passive' metasurfaces, we now analyze luminescent metasurfaces. Whereas 'passive' metasurfaces transform a well-defined incident light beam into a desired output waveform, luminescent metasurfaces must contend with light that is not well-defined in either space or momentum. Most light emitting metasurfaces either 1) sacrifice the generalizability of phased-array metasurfaces and take advantage of Rayleigh anomalies in uniform arrays of metaelements[37–47] or 2) increase the lateral or vertical extent of the system to spatially separate light emission and metasurface functions[48–52]: i.e., integrating distributed Bragg reflectors or metalenses to collimate the emission before imparting the desired phase profile using a separate passive beam deflector. These steps are reasonable considering that spontaneous emission is generally spread across momentum space such that a unique input momentum cannot be specified. Nonetheless, recent demonstrations of near-field mediated light emitting metasurfaces show that generalizable phased-array control of emission can be achieved by considering the majority of input light to be traveling near the critical angle and then otherwise employing common metasurface design heuristics[53,54]. However, these designs often exhibit strong polarization dependencies and significant background emission that isn't successfully mediated via the metasurface interaction.

In this work we leverage physics-based design intuition and machine learning to develop a robust design process for next-generation optical devices with state-of-the-art properties. In Chapter 3, we develop a reciprocal simulation strategy to explain the polarization disparity. We determine that the polarization disparity is partially due to the

difference in phase of induced dipoles from disparately oriented source dipoles. We then validated the accuracy of reciprocity-based simulations and use our new design tool to predict momentum resolved emission patterns from luminescent metasurfaces with a variety of emitter types, including out of plane electric dipoles. Finally, we identify the importance of QW position in ensuring directional emission for each polarization and emitter type.

In Chapter 4, we combine the reciprocal simulation strategy from Chapter 3 with a Bayesian optimization to facilitate the design of highly unidirectional photoluminescent metasurfaces capable of directive p-, s-, or combined p- and s- polarized emission at arbitrary angles. We then fabricate and characterize five metasurfaces, achieving a 54% improvement in p-polarized directivity and the first demonstration of highly directive s-polarized emission, including first-ever simultaneous directivity for s- and p-polarized emission. Using these optimized metasurfaces, we expand and refine intuitive design heuristics for unidirectional emitters.

In Chapter 5, we expand the optimization tools developed for light emitting metasurface and apply them to quantum optics. We design a polarization insensitive anomalous reflector for the miniaturization of magneto-optical traps. The metasurface is designed for polarization insensitive retroreflection of 780 nm circularly polarized light at 54.7°. The proof-of-concept device retroreflects circularly polarized 736 nm light at 50.3°. We discuss oxidation mitigation strategies for future devices and propose a corrective optic for the currently fabricated device.

1.1 Permissions and Attributions

Chapter 2: Simulation and Optimization Tools

This chapter provides a succinct conceptual overview of reciprocity and the efficient global optimization (EGO) algorithm. Reciprocity is critical to the simulation of luminescent metasurfaces whereas EGO is the basis of the optimizations performed in this work. More detailed explanations, intended as an instructional resource, can be found in Appendix A and B.

2.1 Reciprocity

A key aspect of the following research is the principle of reciprocity. Reciprocity states that the relationship between a localized oscillating current and the resultant electric field remains unchanged when the location of the current source and measurement are swapped. Alternatively, it states that antennas work equally well in transmission and reception modes. Reciprocity is valid for linear media with symmetric dielectric permittivity and permeability, including absorptive media. It states that for a localized source distribution, $\vec{J}_1$, emitting electric field, $\vec{E}_1$,

$$\iiint \vec{J}_1 * \vec{E}_2 \, d^3\vec{r} = \iiint \vec{J}_2 * \vec{E}_1 \, d^3\vec{r}. \tag{2.1}$$

In the case where the source is a point-like dipole, i.e. $\vec{J}_i = -i\omega p_i \delta(\vec{r} - \vec{r_i})$, where p_i is the dipole moment, then Equation 2.1 reduces to

$$p_1 * \vec{E}_2(\vec{r_1}) = p_2 * \vec{E}_1(\vec{r_2}). \tag{2.2}$$

The application of this becomes clear if we place p_1 in the device under study, here a metasurface emitter, and we place p_2 far away along some direction θ. $\vec{E}_1(\vec{r_2})$ is the electric field emitted by p_1 at the position of p_2, i.e. the far field emission into the direction θ. Equally,

$\vec{E}_2(\vec{r_1})$ is the electric field at the metasurface as a result of the electric field emitted by the second dipole at θ. Practically, we use Equation 2.2 to draw equivalence between the two, i.e. we can understand the far-field radiation at angle θ (position $\vec{r_2}$) by measuring the electric field in the metasurface, (position $\vec{r_1}$), caused by a plane wave incident at angle $\vec{E}_2(\vec{r_1})$, see Figure 2.1. A full derivation of the reciprocity theorem is available in Appendix A.

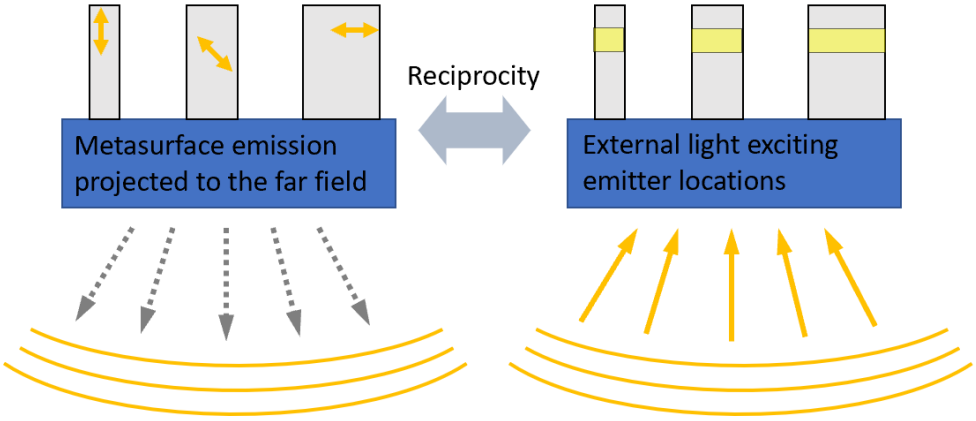

Figure 2.1: The concept of reciprocity. Equivalent information can be obtained by (left) incoherently summing the far field projections of the emission of an ensemble of incoherent dipole emitters and (right) integrating the electric field induced at the emitter location by a series of incident plane waves.

The advantages of reciprocal simulations can be understood in contrast to forward simulations. In a forward simulation, an ensemble of emitters would be simulated individually, and their far field radiation pattern would be incoherently summed together. Accurate results can require many hundreds of dipole locations and orientations. This is made more computationally taxing by the need to simulate a sufficiently large region of the device[34] such that each unique emitter position can be probed without introducing spurious coherent sources by using periodic boundary conditions. Reciprocal simulations allow us to calculate the same information (far field radiation of a collection of dipoles) for a fraction of the computational cost. The number of required simulations is defined by the desired angular

resolution and simulation size is reduced owing to allowed use of periodic boundary conditions. An additional benefit that should be stressed is that reciprocal simulations allow for emitter location multiplexing. In the case of QW emitters, forward simulations would require an assumption of the emitter location. New simulations would have to be performed for each QW location. Reciprocal simulations allow for the electric field to be measured across the entire device and a QW to be 'placed after the fact'.

2.2 Efficient Global Optimization

Efficient Global Optimization (EGO), like most machine learning algorithms, seeks to fit a response surface to a multidimensional objective function. The response surface (or model) can then be used to deduce input-output relationships, estimate maxima, and suggest additional evaluation points[55].

A key difference between EGO and other machine learning algorithms is that stochastic (or random/Gaussian) processes are used to model the objective function (or sampled data). This provides EGO one of its major advantages: an uncertainty estimate regarding any prediction. This uncertainty estimate is critical in balancing the mutually exclusive needs of exploration and exploitation inherent in any optimization problem. The uncertainty is combined with the expected value of any prediction to arrive at an expected improvement (EI)[55]. This type of acquisition function encourages exploration of highly uncertain regions, even when those regions are expected to perform poorly.

Other advantages of this Bayesian optimization algorithm are that EGO, unlike traditional neural networks, is moderately interpretable. We can, for instance, readily identify the relative importance of the different dimensions (or parameters/variables) under study and thereby assess the practicality of a design. Discussion of the mechanics of the interpretation

can be found in Appendix B. Additionally, as opposed to tools like gradient descent, EGO can interpolate and extrapolate over large distances in parameter space, i.e. it does not need to investigate step-by step along a given trajectory, and thus converges more quickly[56].

Methods of applying stochastic processes to predict optima were developed in the 1960 in the interest of identifying promising mineral extraction locations. These mathematical geology approaches are often referred to as Kriging[57]. Such specialized approaches were developed with fixed dimensionality and assumed noisy input data. Such assumptions are not applicable to modeling the results of computer simulations where the inputs are noiseless and many dimensional. Thus, the approach used in this work for the optimization of unidirectional emission and the optimization of polarization-insensitive retroreflection are based on the work of Jones, et al.[55] whose work lays out an algorithm assuming noiseless inputs of arbitrary dimension. It also establishes a method to validate the model and thereby establish the 'reasonableness' of the uncertainty and EI values that are critical to its function.

A detailed analysis and guide to the EGO algorithm is provided in Appendix B, but it is valuable to overview a typical optimization flow, as seen in Figure 2.2. The first step of the optimization is the design of experiment which involves defining parameter space and generating training data. Next, simulations are built, evaluated, and tabulated. The gaussian model is trained, new sampling points are predicted, and convergence is checked, that is, EI is calculated for each point in parameter space and the point with the largest EI is recommended for simulation. If EI is below some threshold, then the optimization is said to have converged and the optimization ends.

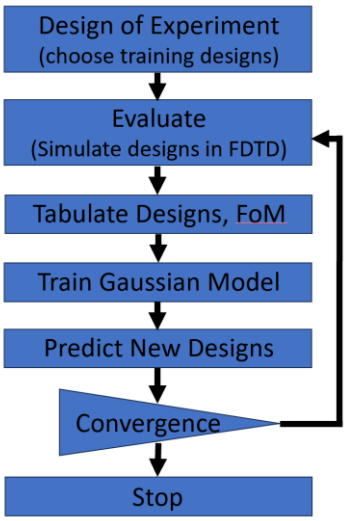

Figure 2.2: A typical optimization flow using the EGO algorithm

Chapter 3: Designing Highly Directional Luminescent Phased-Array Metasurfaces with Reciprocity Based Simulations

3.1 Abstract

Phased-array metasurfaces grant the ability to arbitrarily shape the wavefront of light. As such, they have been used as various optical elements including waveplates, lenses, and beam deflectors. Luminescent metasurfaces, on the other hand, have largely comprised uniform arrays, and are therefore unable to provide the same control over the wavefront of emitted light. Recently, phased-array control of the wavefront of spontaneous emission has been experimentally demonstrated in luminescent phased-array metalenses and beam deflectors. However, current luminescent metasurface beam deflectors exhibit unidirectional emission for only p-polarized light. In this paper, we use a reciprocal simulation strategy to explain the polarization disparity and improve the directionality of incoherent emission from current quantum-well emitting phased-array metasurfaces. We also design complementary metasurfaces to direct emission from systems where emission originates from alternate quantum mechanical processes.

3.2 Introduction

Traditional phased-array metasurfaces grant control over the propagation of transmitted and reflected light by engineering the shape and size of their constituent meta-elements to impart a desired phase profile to a spatially coherent incident beam. Owing to

their ability to arbitrarily shape the wavefront of coherent light, traditional phased-array metasurfaces have seen use as beam deflectors[18,35], polarizing elements[58,59], lenses[1,60], holographic phase masks[61,62], and vortex beam generators[5,63]. In this sense, most traditional phased-array metasurfaces are optical elements which require a coherent incident light source. Luminescent metasurfaces, on the other hand, are integrated with their own generally incoherent light source. Although early work coupling emitters to plasmonic nanoantenna showed luminescent phased functionality[64–67], much of the subsequent work has focused on metasurfaces with uniform arrays[45,68–71]. Although uniform metasurfaces impact the spectrum, radiation patterns, and emission intensity of the coupled lumophore, they are unable to impart the phase-control necessary for arbitrary wavefront shaping.

Recently, luminescent phased-array metasurface lenses, axicons, and beam deflectors comprising GaN nanopillars embedded with InGaN quantum wells (QWs) have been experimentally demonstrated[54,72]. Because these luminescent phased-array metasurfaces are a relatively new outgrowth of the more traditional transmissive and reflective metasurfaces, many questions remain as to their operation and design. In particular, although the luminescent beam deflectors produced by Ilyer et al. exhibited both p- and s-polarized unidirectional transmission, unidirectional photoluminescence was only observed for p-polarized light[54]. Further, although an accompanying analytical model accurately explained the most striking features of the emission patterns, it lacks the granularity to enable robust design of future luminescent metasurfaces.

In this work, we validate the results of a reciprocity-based simulation scheme against experimental results measured by momentum-resolved photoluminescence. Subsequently, we employ these reciprocal simulations to predict the emission patterns of luminescent beam

deflectors, identify important parameters for achieving directionality, and develop heuristics for metasurface design. These tools allow us to investigate the highly polarized nature of the directional emission seen in experiment. Lastly, we use the simulation tools and heuristics to improve the directionality of existing beam deflectors, design beam deflectors capable of highly directional s-polarized emission, design metasurfaces for directional air-side emission, and identify metasurface designs for directing emission from other quantum-well systems with different underlying quantum mechanical transitions. These results aid in our practical understanding of unidirectional emission from luminescent phased-array metasurfaces and allow the optimization of future devices.

3.3 Results and Discussion

In a beam-deflecting metasurface, a coherent plane wave with a transverse momentum of $k_{||,i} = k_0 \sin(\theta_i)$ is redirected into a unidirectional transmission lobe with a transverse momentum of $k_{||,t} = k_0 \sin(\theta_t)$, where k_0 is the free space momentum and θ_i and θ_t are the angles of incidence and transmission, respectively. The difference between the momenta of the transmitted and incident waves is equal to the "metasurface momentum", $k_M = k_{||,t} - k_{||,i}$. Assuming a linear metasurface phase gradient, $k_M = \frac{d\varphi}{dx} = \frac{2\pi}{\Delta}$, where φ is the phase profile with respect to position, x, is the free space wavelength, and Δ is the metasurface macroperiod. Using the above principles, a beam deflecting metasurface can achieve unidirectional transmission according to $k_{||,t} = k_{||,i} + \frac{2\pi}{\Delta}$. This description breaks down when we consider that spontaneous emission is generally spread across momentum space and a well-defined input momentum cannot be ascribed to the emitted light. However, spontaneous

emission from in-plane electric dipoles in InGaN/GaN QW thin films, has a strong distinct peak just beyond the critical angle at $k_{||,i} = \pm 1.06 k_0$, as seen in Figure 3.1a. Although this ray is ordinarily trapped in the substrate, metasurface patterning can redirect the emission and facilitate extraction into air.

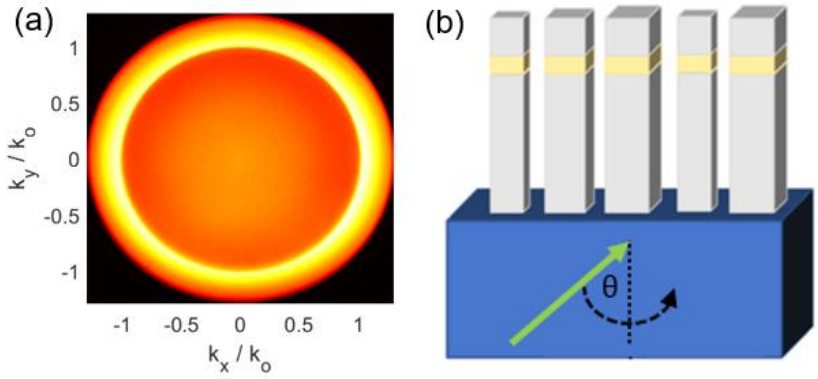

Figure 3.1. (a) Momentum resolved radiation pattern of InGaN QWs in an unpatterned GaN thin film. (b) Schematic representation of a beam deflector simulation. The yellow layer in the nanopillars represents the QW region and the green arrow represents the input plane wave which is then swept across momentum space.

To investigate the observed polarization dependence, find metasurface designs capable of directional s-polarized emission from in-plane electric dipoles, and investigate directional emission from alternate quantum emitters, we employ and evaluate a reciprocity-based numerical simulation scheme[45,53,73]. We simulate beam deflectors comprising arrays of square cross-section, 1450 nm tall GaN nanopillars of varying width with InGaN QWs embedded 113-148 nm below the air/GaN interface. Nanopillars are spaced 250 nm apart and sit atop a sapphire substrate. The nanopillars widths are chosen to give a linearly varying transmission phase, as discussed in our previous work[54,72]. An angled plane wave is sourced within the semi-infinite sapphire substrate and propagates towards the metasurface (Figure 3.1b). The incident angle for both p- and s- polarized light is swept to predict the far field

emission pattern as a function of angle. By reciprocity, the integrated electric field component, $\int |E_i(x,y)|^2 dxdy$, in the QW region is proportional to the emitted far-field photoluminescence intensity at the same angle from a dipole source oriented along i[74]. Thus, we are able to quickly simulate p- or s- polarized emission from hypothetical QWs at any arbitrary position in the nanopillar with the same angle dependent simulations by integrating the appropriate electric field component at the desired z coordinate. The reciprocal method also allows us to simulate a small periodic region of the metasurface as opposed to a large, finite array as would be needed in a local dipole source method[34], giving us both smaller simulation domains and QW position multiplexing. Details of the simulation settings can be found in Chapter 3.5.

Figure 3.2 shows experimental (solid line) and simulated (circles) emission patterns of 540 nm light as a function of transverse momentum. Results are shown for both p- (left) and s-polarized (right) light for two different 1D beam deflectors, one designed to emit at -0.41 k_0 (top) and another at -0.08 k_0 (bottom). Emission patterns from other 1D beam deflectors are given in Figure 3.9. Calculations and measurements agree very well for p-polarized emission—the simulations accurately predict the location and intensity of the main metasurface-mediated unidirectional emission lobes. Calculations and measurements also agree for s-polarized emission—predicting all the major emission features, including the local minimum at the target emission momentum.

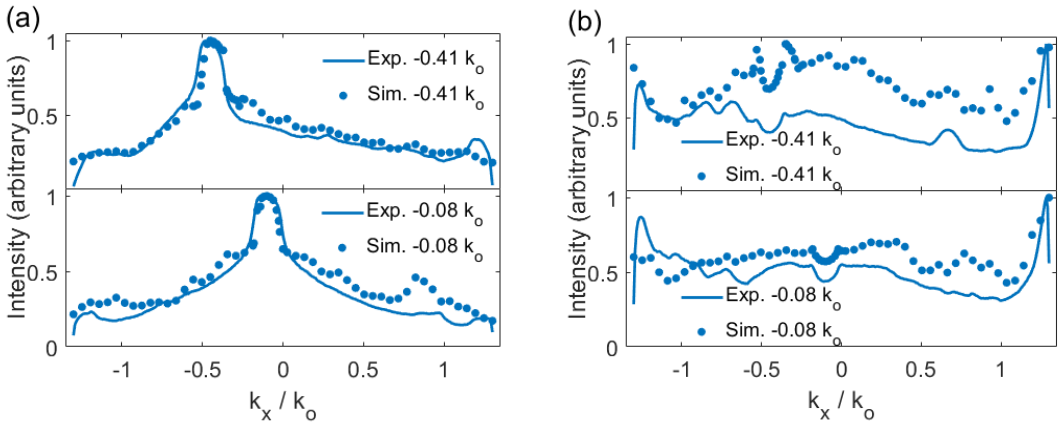

Figure 3.2. Simulated (circles) and measured (lines) emission at 540 nm for (a) p-polarized and (b) s-polarized light from two beam deflectors designed to emit at either -0.41 k_0 (top) or -0.08 k_0 (bottom).

The variance seen for p- and s-polarized emission from these metasurfaces is dramatic. Whereas p-polarized emission shows a maximum at the target momentum, s-polarized emission shows a local minimum. To understand this polarization dependence, which is nearly absent in transmission[54], it is important to understand the fundamentally different mechanisms by which metasurfaces impart directionality to transmitted versus emitted light. In transmission, each nanopillar is "sourced" by an incident plane wave which creates a defined phase relationship between the different nanopillars. As the light propagates down, each nanopillar imparts a different phase shift producing the desired output phase. In this abstraction, interpillar coupling—whereby source dipoles in one nanopillar generate induced polarization dipoles in neighboring nanopillars—produces a small perturbation of the desired results. If interpillar coupling is ignored, the four-fold nanopillar symmetry produces identical results for s- and p-polarization. In the case of luminescent metasurfaces however, interpillar coupling is *essential* to achieving directional emission.

In luminescent operation, a single source dipole in one nanopillar induces polarization dipoles in neighboring nanopillars with a well-defined phase relationship. The interference between waves generated via source and induced dipoles leads to directional emission. The emission from varying source dipoles is summed incoherently, as necessitated in spontaneous emission. Thus, p-polarized emission—which is driven by dipoles oriented parallel to the phase gradient—will exhibit different interpillar coupling phase relative to s-polarized emission—which is driven by in-plane dipoles oriented perpendicular to the phase gradient. Figure 3.3 shows the phase of 540 nm light emitted from dipoles placed 120 nm below the air/GaN interface of a uniform array of 1450 nm tall, 170 nm wide nanopillars - other nanopillar widths show similar patterns. We see that p-polarized light accumulates approximately π radians of phase between neighboring nanopillars whereas s-polarized light accumulates approximately 0.5 π radians of phase between the source dipole and an induced dipole. Details of this simulation can be found in Section 3.5.

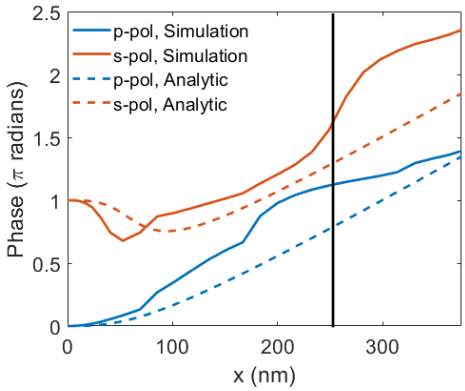

Figure 3.3. Phase of light emitted from dipoles placed at the QW location of a uniform array of nanopillars – vertical line marks the center of the neighboring nanopillar.

Having first experimentally validated our numerical simulations, we subsequently use them to optimize existing luminescent metasurface designs. In an effort to standardize and

expedite our simulations, we chose to simulate luminescent beam deflectors comprised of 1000 nm tall nanopillars with metasurface momentum $k_M = 0.72k_o$. Naturally, changing the nanopillar height necessitates recalculating the relationship between nanopillar width and phase response, see Section 3.5 for details.

As these reciprocal simulations allow for QW position multiplexing, emission patterns of p-polarized light were simultaneously calculated for QWs spanning from 0 to 400 nm below the GaN/air interface. The emission pattern for 540 nm was extracted as described above and the directivity at the target angle ($\theta_t = 0.193$ rad), $D(\theta) = \frac{I(\theta_t)\ [\max(\theta) - \min(\theta)]}{\int I\, d\theta}$, was calculated as a function of normalized QW position. Consistent with our previous experimental design intuition, maximum directivity occurs for QWs placed nearly 0.5 λ_0/n below the GaN/air interface. Specifically, we see that maximum directivity occurs at 0.477 λ_0/n (110 nm). Similar simulations were carried out using 480-560 nm incident light. These wavelengths roughly correspond to the InGaN QW emission band, (Figure 3.4a inset). The directivity as a function of QW position for all source wavelengths is shown Figure 3.4a. We see a clear sinusoidal pattern for each wavelength, and a marked increase in directivity as source wavelength decreases from 540 nm to 500 nm. A maximum directivity of $D = 5.59$ is seen with a 500 nm source for QWs placed 0.328 λ_0/n (70 nm) below the air/GaN interface. Since our simulations use non-dispersive optical constants, this increase in directivity is achievable for our design wavelength of 540 nm (the wavelength of maximal emission for InGaN QWs) by scaling all metasurface dimensions by 540/500. When we simulate a metasurface that accounts for both QW position and the wavelength-based isotropic scaling, we see that we can achieve a 60% increase in directionality over the initial unscaled

metasurface design where we place the QW 0.5 λ_0/n (115 nm) below the air/GaN interface, see Figure 3.4b. We see that in addition to QW position, moderate isotropic scaling can have a powerful impact on directionality. Interestingly, this improved design represents a 90% increase in directionality over the best metasurface produced by Ilyer, et al.[54].

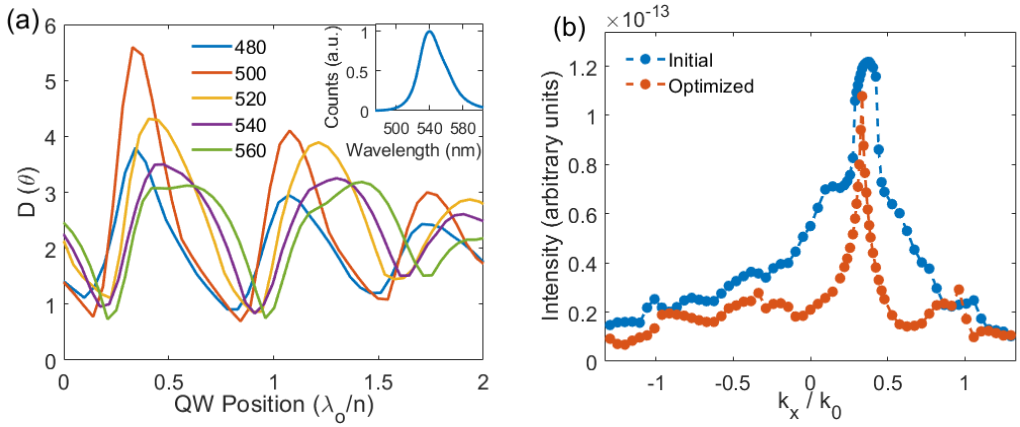

Figure 3.4. (a) Simulated directivity of p-polarized emission as a function of QW position for a variety of wavelengths. Inset shows emission spectrum of a luminescent metasurface peaking at 539.5 nm. (b) Simulated emission for p-polarized light from a beam deflector with a target momentum of 0.34 k_0 at 540 nm before (blue) and after (red) QW relocation and dimension rescaling.

In addition to improving unidirectional p-polarized emission, we can use our simulation technique to identify metasurface designs for unidirectional s-polarized emission. Just as with p-polarized light, the directivity of s-polarized light has a sinusoidal relationship with QW position. The s-polarization cycle is approximately 180 degrees out of phase with the p-polarization cycle: the s-polarization maxima occur near p-polarization minima (Figure 3.5a). This is important in explaining the difference in directionality between p- and s-polarization in experimental metasurfaces. The experimental metasurfaces had their QWs located at approximately 0.5 λ_0/n. This QW location corresponds to sub-unity directionality,

whereas high directivity occurs near 0.9 λ_0/n. In an attempt to improve directionality, we again rescale to the initial metasurface design as described above. We see that directivity is maximized ($D = 2.81$) at the original scale (540 nm) for a QW located 0.867 λ_0/n (200 nm) below the air/GaN interface. The directional s-polarized emission pattern is shown in Figure 3.5b alongside the original emission pattern corresponding to QWs placed 120 nm below the air interface. (Note the similarities between the initial trace in Figure 3.5b and the s-polarized traces in Figure 3.2b.) By appropriately relocating the QWs, undesired emission at high momenta is minimized while emission at the target momentum transforms from a local minimum to a global maximum, as desired for unidirectional emission.

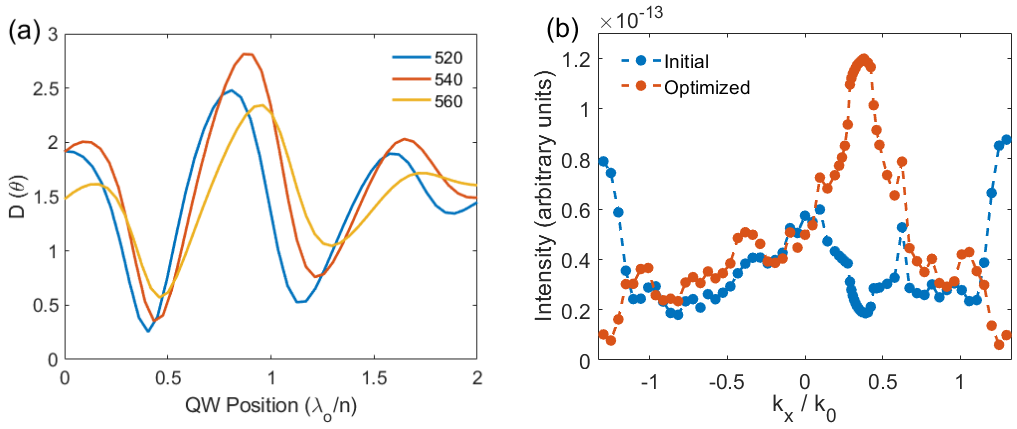

Figure 3.5. (a) Simulated directivity of s-polarized emission as a function of QW position for a variety of wavelengths. (b) Simulated normalized emission for 540nm s-polarized light from a beam deflector with a target momentum of 0.34 k_0 at 540 nm before (blue) and after (red) relocating the QWs.

All simulations thus far have utilized a plane wave source originating within the substrate. This was originally done to compare simulation with experiment (Figure 3.2), but emission does not need to be collected from the substrate. We can easily simulate emission directly into air by sourcing the plane wave in air. Naturally, the QWs of an air side emitter

should be located near the sapphire/GaN interface, such that appreciable transmission phase can accumulate through the nanopillar. Balancing this need for QW depth with growth defects caused by a lattice mismatch between sapphire and GaN, we performed a new phase-width calibration for QWs located about halfway up the nanopillars. As above, our air side luminescent beam deflector is designed for a target output momentum $k_x = 0.34\ k_o$. Running corresponding simulations for a variety of scaling factors and measuring directivity, we obtain Figure 3.6a. Although the directivity is not quite as high, the same sinusoidal pattern is seen here as in the case of substrate-side emission. Figure 3.6b shows the maximally directional emission, corresponding to a metasurface that has had its dimensions scaled by 540/530, its QW buried 2.74 λ_0/n (560 nm) below the air/GaN interface, and a directivity of $D = 2.47$.

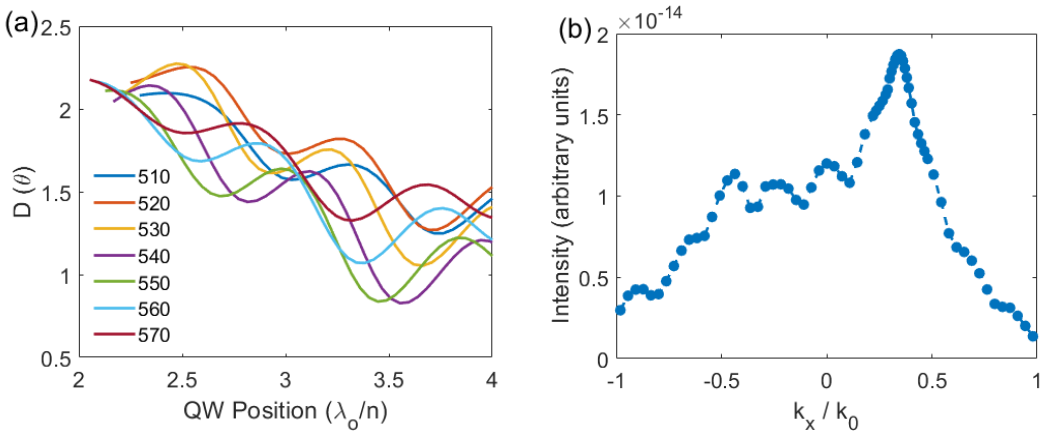

Figure 3.6. (a) Simulated directivity of p-polarized emission as a function of QW position for a variety of wavelengths. (b) Simulated normalized emission for an air-side beam deflector with a target momentum of 0.34 k_0.

Finally, we can use these simulations to move beyond in-plane oriented electric dipoles characteristic of InGaN/GaN QWs. Specifically, we can investigate metasurface emission from *out-of-plane* electric dipoles by considering the out-of-plane electric field component from p-polarized sources in substrate-side simulations. Using the same design as

for other substrate-side simulations, we see unidirectional emission at the target wavelength for out-of-plane electric dipoles located about 0.9 λ_0/n below the air-GaN interface of the default structures, see Figure 3.7a. As above, we rescale the simulation to improve directionality. We see that a 540/510 isotropic scaling provides maximal directionality, $D = 3.82$, when the QW is placed 0.826 λ_0/n (180 nm) below the air/GaN interface. Simulated emission results corresponding to the maximal directionality can be seen in Figure 3.7b.

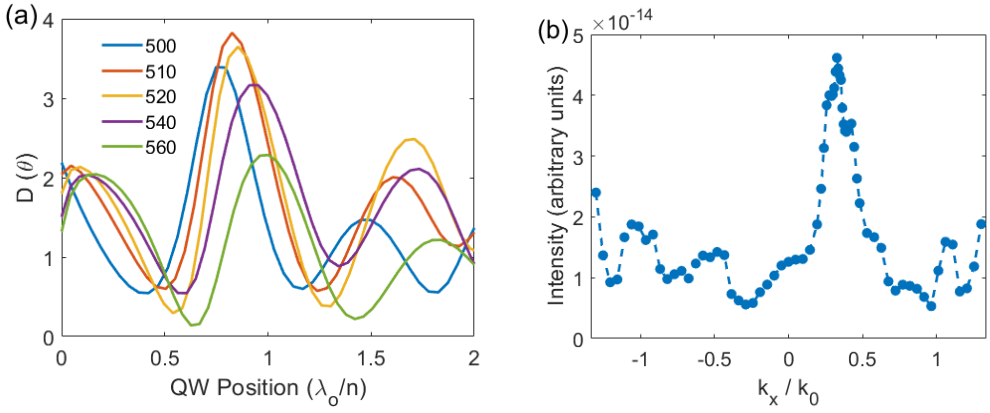

Figure 3.7. (a) The directivity of simulated p-polarized emission from out-of-plane electric dipoles as a function of emitter position for a variety of wavelengths. (b) Simulated normalized emission for p-polarized light from a beam deflector with a target momentum of 0.34 k_0.

3.4 Conclusion

Luminescent phased-array metasurfaces grant the ability to shape the wavefront of spontaneous emission. However, owing to the lack of sophisticated modeling tools, questions of how to achieve unidirectional emission from the various types and orientations of quantum emitters were unanswerable. In this paper, we determine the polarization-based disparity in emission from luminescent phased-array beam deflecting metasurfaces is partially due to the difference in phase of induced dipoles from disparately oriented source dipoles. We employ a

powerful simulation strategy to predict the momentum resolved emission patterns from luminescent metasurfaces and identify the importance of QW position in ensuring directional emission. We also see that minor isotropic scaling can result in marked improvement of directionality. We have designed new luminescent beam deflecting metasurfaces with highly directional p- and s- polarized emission from in-plane electric dipoles. We similarly designed metasurfaces capable of directional air-side emission. And finally, we design metasurfaces capable of directional substrate-side p-polarized emission from out-of-plane electric dipoles. The simulation tools and heuristics developed here will dramatically improve the design and efficiency of luminescent beam deflectors and provide a launching point for the further exploration of luminescent phased-array metasurfaces.

3.5 Supporting Information

Lumerical FDTD was used for all simulations.

Phase Delay Calculations

A unit cell consisting of a nanopillar atop a sapphire substrate was illuminated by a 540 nm dipole placed 100 nm below the top of the nanopillar. Bloch boundary conditions were used in the lateral planes and perfectly matched layers were used above and below the nanopillar. The phase of the transmitted electric field was measured one wavelength below the nanopillar. The nanopillar width was altered in subsequent simulations to obtain a phase-width response as seen in Figure 3.8.

The phase response of various nanopillar widths and heights is plotted in Figure 3.8. It is worth noting that the choice of where to wrap the phase response is arbitrary. We chose to wrap the 1000 nm phase in such a way that it is roughly similar to the phase relationship

for 1450 nm nanopillars used by Ilyer et al.[1] At the extremes of nanopillar widths, emission patterns are nondirectional (small nanopillars) or begin to approximate a thin film (large nanopillar). Based on this phase relationship, Figures 3.4, 3.5, and 3.7 rely on simulations using 1000 nm tall square nanopillars that are 137, 163, and 192 nm on a side.

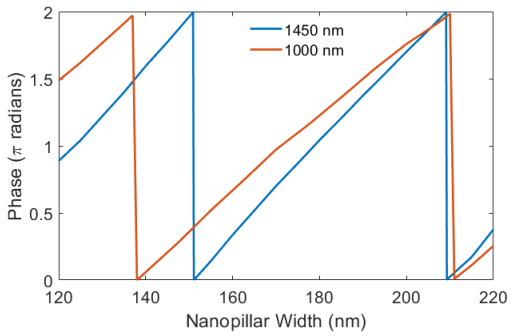

Figure 3.8: Transmission phase as a function of nanopillar width for either 1450 nm (blue) or 1000 nm (red) tall nanopillars with an interpillar spacing of 250 nm.

Metasurface Emission Simulations

The desired metasurface was constructed as described in the text. Bloch boundary conditions were used along the lateral planes while perfectly matched layers were used above and below the metasurface. An auto non-uniform mesh type a 24-layer steep angle PML boundary was used. An additional override mesh with 13 nm resolution was used throughout the hypothetical QW region. The electric field intensity at the QW was determined via a frequency domain power monitor. Integration excluded the outermost 26 nm of the nanopillar, bringing simulation into agreement with experiment.

Dipole Phase Simulations

A 7x7 array of nanopillars, with dimensions as indicated in the text, on sapphire were simulated with PML boundaries on all sides. A 540 nm dipole source was placed at the QW location and an additional override mesh with was placed near the source dipole to increase

resolution. The phase of emitted light was measured across the plane of the QW using a frequency domain power monitor.

Reciprocal Simulation Validation

In Figure 3.9, we show normalized results for both experiment (solid line) and simulation (dots) along a line cut corresponding to p-polarized and s-polarized 540 nm light for eight devices. Experimental devices are intended to emit at 0.91, 0.74, 0.58, 0.44, 0.31, 0.22, 0.14, 0.10 k_0. Owing to a strict periodic boundary condition in the simulations, simulated devices are intended to emit at 0.88, 0.72, 0.56, 0.41, 0.29, 0.20, 0.12, 0.08 k_0. The p-polarized line-cut shows excellent agreement in both the location of the main emission lobe and its prominence relative to the rest of the emission pattern. The s-polarized line cut also shows good agreement concerning major features, but the relative intensity is skewed.

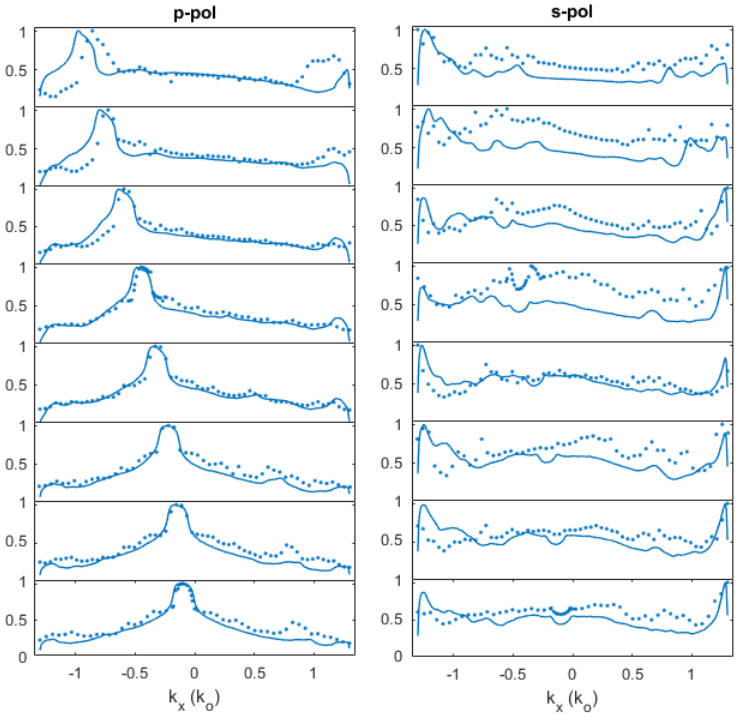

Figure 3.9: Simulated and measured emission at 540 nm for (a) p-polarized and (b) s-polarized light from a series of deflectors.

Chapter 4: Optimizing Polarization Selective Unidirectional Photoluminescence from Phased-Array Metasurfaces

4.1 Abstract

Metasurface-based optical elements offer a wide design space for miniature and light-weight optical applications. Typically, metasurface optical elements transform an incident light beam into a desired output waveform. Recent demonstrations of light-emitting metasurfaces highlight the potential for directly producing desired output waveforms via metasurface-mediated spontaneous emission. In this work, we use reciprocal FDTD simulations and machine learning to enable the inverse design of highly unidirectional photoluminescent III-Nitride quantum well metasurfaces capable of directive p-, s-, or combined p- and s- polarized emission at arbitrary angles. In comparison with previous intuition-guided designs using the same quantum well architectures, the inverse design approach enables new polarization capabilities and experimentally demonstrated improvements in directivity of 54%. We conclude with an analysis of ways in which the inverse design both validates and contradicts previous intuition-guided design heuristics. Ultimately, the combination of reciprocal simulations and efficient global optimization (EGO) grants us remarkable improvements in emission directivity and results in full control over the polarization and momentum of emitted light, including simultaneous directional emission of s- and p-polarized light.

4.2 Introduction

Phased-array metasurfaces have enabled a host of flat and low-weight optics including beam deflectors[75–78], lenses[79–82], axicons[24,83], hologram generators[3,4,84], and more[5,85–88]. In all these cases, core functionality is achieved by imparting a desired spatial phase profile onto an incident beam via judicious placement of metaelements. Beam deflecting metasurfaces aim to steer incident light into a unidirectional output and have immediate applications in technologies such as augmented reality and LiDAR[13,89]. In the case of passive beam deflectors, metaelements are placed to create a linearly varying spatial phase delay of the incident plane wave where the angle of anomalous deflection (steering) is set by the metasurface phase-gradient[90]. Light emitting metasurfaces offer intriguing opportunities to study fundamental light-matter interactions and further miniaturize optical components[15,33,34]. Most light emitting metasurfaces either 1) sacrifice the generalizability of phased-array metasurfaces and take advantage of Rayleigh anomalies in uniform arrays of metaelements[37–47] or 2) increase the lateral or vertical extent of the system to spatially separate light emission and metasurface functions[48–52]: i.e., integrating distributed Bragg reflectors or metalenses to collimate the emission before imparting the desired phase profile using a separate passive beam deflector. These steps are reasonable considering that spontaneous emission is generally spread across momentum space such that a unique input momentum cannot be specified. Nonetheless, recent demonstrations of near-field mediated light emitting metasurfaces show that generalizable phased-array control of emission can be achieved by considering the majority of input light to be traveling near the critical angle and then otherwise employing common metasurface design heuristics[53,54]. However, these designs often exhibit strong

polarization dependencies and significant background emission that isn't successfully mediated via the metasurface interaction. Given the complexity of metasurface-mediated light emission, initial results highlight the possibility for achieving far superior performance using more sophisticated design approaches. For instance, recent work has demonstrated directional emission by from III-V quantum dots in a uniform array of nanopillars by use of a spatially modulated pump beam[91]. A generative model, paired with active learning, has also been used to increase emission directivity by tuning the pump beam pattern[92].

Similarly, the performance of passive metasurfaces has been optimized using many techniques including the adjoint gradient method[82,88,93], genetic algorithms[76,94], neural networks[95], and Bayesian optimization in the form of efficient global optimization (EGO)[75]. Regardless of the optimization method, the efficiency of any passive beam deflecting metasurface geometry can be predicted using a single forward simulation where a plane wave of definite momentum interacts with the surface and is projected into the far field. Photoluminescent metasurfaces, on the other hand, inherently require many simulations to capture the wide angular distribution of emission. This can be done with either a set of forward simulations - where the radiation pattern of an ensemble of dipoles is projected into the far field and incoherently summed, or in a set of backward (reciprocal) simulations - where the electric field intensity resulting from plane waves of varying incident angles is equivalent to the far-field emission pattern[34]. The reciprocal method has shown excellent agreement with experiment and necessitates fewer simulations (than the forward method) as reciprocity allows for emitter position multiplexing[96]. However, simulating a single metasurface design still requires performing dozens of simulations—one for each output angle. This marked increase in simulation number requires efficient optimization strategies. EGO has been shown to

outperform various evolutionary optimization algorithms for many passive metasurfaces[56] including the case of a passive beam deflecting metasurface[75].

Previous intuition-guided designs based on the generalized law of refraction[21] have been used to demonstrate photoluminescent unidirectional emitters[53,54], axicons, and lenses[72,97]. Despite these successes, intuitively designed unidirectional emitters experimentally demonstrate directional emission for only p-polarized light with a rounded emission profile – resulting in moderate directivity values ($D \approx 3$). Intuitive design further falls short in accounting for the drastic effects of QW position. In this paper, we overcome these challenges and demonstrate the design, fabrication, and characterization of five optimized unidirectional light emitting phased-array metasurfaces, including a metasurface capable of simultaneous directional emission of s- and p-polarized light. We experimentally demonstrate arbitrary control of emission angle and polarization at 540 nm with excellent directivity ($D = 5.5$) enabled by inverse design under EGO rather than intuitive design heuristics.

4.3 Results and Discussion

4.3.1 Metasurface Simulation and Optimization

The metasurfaces studied in this work comprise periodic arrays (along the x-axis) of 1000 nm tall GaN nanoribbons atop a sapphire substrate. Each nanoribbon contains a single embedded InGaN/GaN quantum well (QW). The nanoribbons extend semi-infinitely along the z-axis and have varying widths along the x-axis. Optimizations were carried out for semi-infinite nanoribbons to reduce computational cost via decreased dimensionality. Momentum-resolved photoluminescence intensity is simulated (Section 4.5) simultaneously from a

multitude of hypothetical single QWs in the yellow region of Figure 4.1b. We optimize the metasurface for downward emission at 540 nm into the substrate across k_x along $k_z = 0$, see Figure 4.1b, using an inverse design-based EGO algorithm[55]. The EGO algorithm has two major steps: first, it builds a probabilistic surrogate model from a database of fitness observations, second it uses this surrogate model to inform an acquisition function (infill criterion) to determine which new designs should be tested.

As EGO is a parametric optimization tool, we must define our metasurface parameter space and figure of merit (Section 4.5). The parameters comprise each of the nanoribbons' position and width as well as the metasurface periodicity. We stress that the reciprocal simulation method allows us to determine directivity for any QW height in a given geometry. In doing so, we determine the optimal QW height via a brute force search over all possible positions, reducing the dimensionality of the EGO algorithm. As shown in Figure 4.1b, this results in seven free parameters for the case where there are three nanoribbons per metasurface period. The figure of merit is a function of these free parameters.

Five optimizations were pursued: Case 1 and Case 2 optimized directivity of p-polarized emission at $0.00\ k_0$ and $-0.34\ k_0$ ($0°$ and $-20°$ exitance), respectively. Case 3 and Case 4 optimized directive emission at the same angles for s-polarized light. Finally, Case 5 simultaneously optimized directivity of p- and s- polarized emission at normal exitance. The figure of merit is the maximum directivity at the target angle in sapphire, θ_t, for all hypothetical QW positions across the y-axis, i.e. $\max\left[D_{\theta_t}(y)\right]$. For cases 1, 2, and 3, directivity was calculated straightforwardly as $D_{\theta_t}(y) = \frac{I(\theta_t,y)\ [\max(\theta)-\min(\theta)]}{\int I(\theta,y)\ d\theta}$ where $I(\theta, y)$ is the simulated intensity (Section 4.5) as a function of plane wave input angle in sapphire, θ,

and QW position, y. During the course of the optimization, Case 4 began to display highly directional, but symmetric emission. Although bidirectional emission could be useful, such emission was not the goal of this study. Thus, the figure of merit for Case 4 was changed to punish symmetric emission. This was accomplished by finding the correlation coefficient, C, of the simulated emission profile, $I(\theta, y)$ with $I(-\theta, y)$. $C\big(I(\theta, y), I(-\theta, y)\big)$ varies between $[-1, 1]$ for anti-symmetric and symmetric emission, respectively. Thus, the figure of merit for Case 4 is $\max\big[D_{\theta_t}(y) * \big(1 - \max\big[C\big(I(\theta, y), I(-\theta, y)\big), 0\big]\big)\big]$. Case 5 required a modification to the figure of merit to account for the simultaneous optimization of both polarizations. In this case, the figure of merit was a normalized addition: $\frac{D_{p,\theta_t}(y)}{D_{p,max}} + \frac{D_{s,\theta_t}(y)}{D_{s,max}}$ where $D_{p/s,max}$ is the maximum directivity found in Case 1 and 3, respectively. Normalization encouraged simultaneous directional emission by accounting for the fact that the figure of merit for p-polarized emission was always higher than the figure of merit for equivalent s- optimized structures. Ultimately, the approach demonstrated here is e.g., material-, exitance angle-, wavelength-, and polarization-agnostic and provides a valuable tool in the future design of photoluminescent metasurfaces beyond these specific cases.

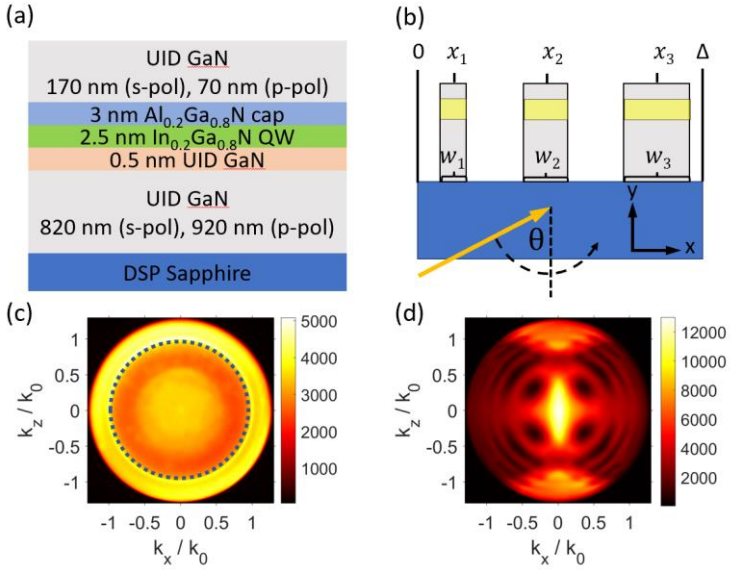

Figure 4.1. (a) Schematic of the unpatterned InGaN/GaN QW thin films. Individual InGaN quantum wells are buried below an unintentionally doped (UID) GaN layer whose thickness is determined via numerical optimization. (b) A schematic showing the metasurface simulation and optimization scheme. Light is incident from the substrate at a series of angles such that $|k_{||}| \leq 1.3\, k_o$. Momentum-dependent emission intensity is determined by integrating the resultant electric field within the QW (yellow) region as a function of position along the y-axis. The nanopillar positions and widths are uniquely determined by allowing x_i and w_i to be free parameters. Cases 2, 4, and 5 use three nanoribbons within a unit cell of period Δ, whereas Cases 1 and 3 use two nanoribbons within a unit cell of period Δ. (c) Experimentally measured unpolarized momentum resolved emission pattern of an unpatterned thin film. The pattern is typical of all the thin films used here, exhibiting an emission peak beyond the critical angle (dotted circle at 1.0 k_0). (d) Experimentally measured z-polarized momentum resolved emission pattern of Case 3 after fabrication.

4.3.2 Fabrication and Characterization

After determining optimized parameters (see Table 5.2), QW emitters were grown by MOCVD (Section 4.5). Optimizations indicated maximally directive p-polarized (s-polarized) emission for QWs buried 70 nm (170 nm) below the air/GaN interface regardless of the target output momentum. For combined s- and p- unidirectional emission a QW depth

of 120 nm was optimal. Interestingly, p-polarized metasurfaces converged on wider nanoribbons (widths ranging from 140 nm to 215 nm), than s-polarized metasurfaces (widths ranging from 50 nm to 135 nm). After QW growth, samples were fabricated (Section 4.5) and photoluminescence characterized using energy-momentum spectroscopy (Section 4.5). Measured and simulated 540 nm momentum-resolved intensity profiles are shown in Figure 4.2. It is important to note that our figure of merit, directivity, is conventionally defined in terms of angle. Nonetheless, the experimental setup measures emission intensity as a function of momentum. As such, we report experimental data in momentum space, but transform the measured data to angle space in sapphire for the purpose of determining directivity. We see excellent agreement between simulation and experiment in all cases regarding the momentum of maximum emission (or target output momentum) and good agreement between simulation and experiment for line shape in most cases.

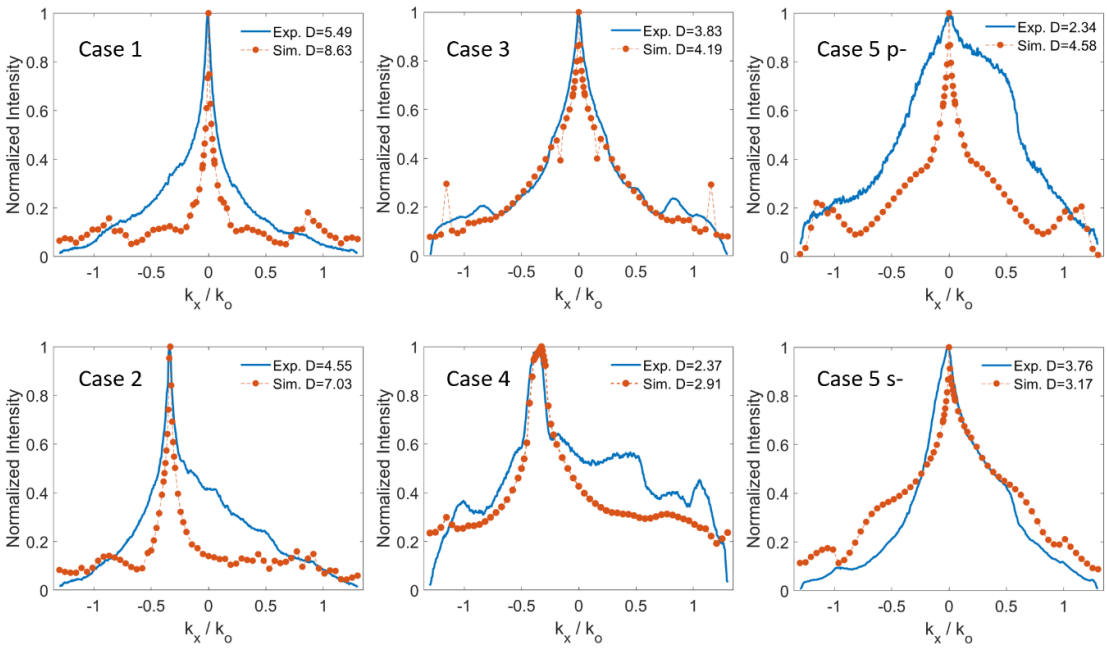

Figure 4.2. Measured and simulated momentum-resolved intensity profiles for 540 nm emission for all 5 Cases. Cases 1 and 2 show p-polarized emission, Cases 3 and 4 show s-polarized emission, and Case 5 shows both p- and s-polarized emission.

These experiments demonstrate a number of advancements compared to previous work within this class of metasurface architecture. Firstly, these are the first demonstrations of s-polarized (Case 3 and Case 4) and "unpolarized" (Case 5) metasurface emitters in GaN QW metasurfaces. Secondly, we see improved emission directivities of at least 54% compared to previous work (Figure 4.5). This improvement was enabled by the pairing of reciprocal simulations with the EGO algorithm. While the reciprocal simulations determined ideal QW placement, this machine learning approach efficiently found the ideal metaelement size and location as well as unit cell periodicity (Figure 4.6). The disagreement between simulation and experiment likely originates from inevitable growth/fabrication errors. In particular, emission directivity is highly sensitive to QW position[96]. A shift of 20 nm between design position and growth position could explain the discrepancy between simulation and experiment in Cases 1-4, whereas the discrepancy in Case 5 is due to fabrication errors coincidentally increasing s-polarized directivity at the cost of p-polarized directivity.

4.3.3 Comparison with Previous Design Heuristics

Our previous design heuristics begin with an effort to redirect emission lobes in unpatterned thin films (Figure 4.1c) that lie just beyond the critical angle, $|k_{||,i}| \approx 1.12\, k_0$. This is initially achieved by choosing a metasurface period, Δ, such that first-order diffraction brings this lobe to the desired final momentum, $k_{||,f} = k_{||,i} + \frac{2\pi}{\Delta}$ (Section 4.3). Our metasurface optimizations qualitatively validate this choice. Table 5.1 compares our five metasurfaces in terms of Δ, $k_{||,f}$ (as seen in Figure 4.2), $k_{||,i}$ (as implied by the value of Δ),

and the momentum of maximum emission from each respective unpatterned thin film, see Figure 4.7. In all cases, the metasurface periodicity implies an initial momentum exactly at (Cases 1, 2, 3, and 5) or very near (Case 4) the critical angle but does not correlate precisely with the thin film emission maxima, which had been an intuitive choice for $k_{||,i}$.

Table 4.1: Final and implied initial emission momentum values for the five metasurfaces fabricated in this work along with the momentum of maximum emission for the thin films from which each metasurfaces was fabricated.

Case	Δ (nm)	$k_{\|\|,f}/k_0$	Implied $\|k_{\|\|,i}\|/k_0$	Thin Film $\|k_{\|\|,i}\|/k_0$
1	540	0.00	1.00	1.05
2	805	-0.33	1.00	1.05
3	540	0.00	1.00	1.12
4	745	-0.35	1.07	1.12
5 p-	540	0.00	1.00	1.24
5 s-	540	0.00	1.00	1.01

The value that the optimization provides in selecting a good choice of metasurface period can be seen when we attempt to intuitively design a metasurface for normal exitance of s-polarized emission. The thin film optimized for s-polarized emission exhibits a bright emission lobe at $1.12\ k_0$, but setting the periodicity to shift this lobe to normal exitance ($\Delta = 482$ nm) results in a simulated dual-peak emission feature as seen in Figure 4.3a, rather than the single-peak cusp in the simulated optimized design ($\Delta = 540$ nm). This local minimum is reminiscent of experimental results seen in other work[54,96] and results in a 36% decrease in directivity relative to the EGO optimized structure.

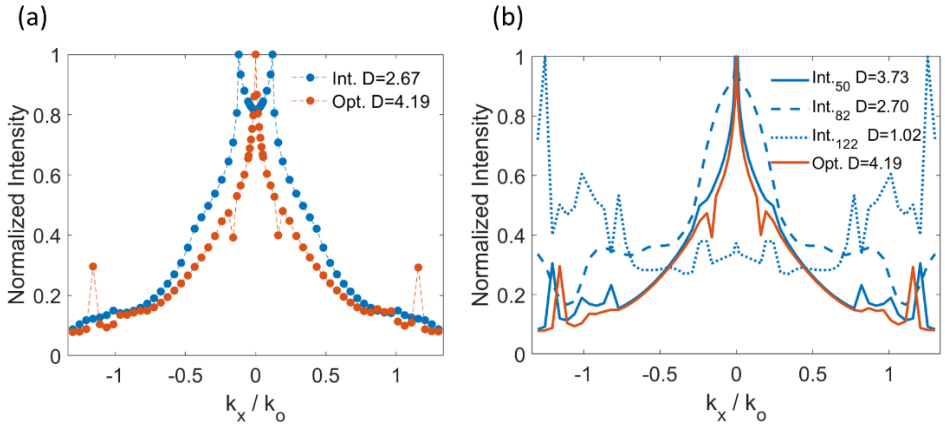

Figure 4.3. Simulated emission profiles for intuitive designs seeking to achieve s-polarized emission at normal exitance given a GaN thin film with a QW buried 170 nm below the surface. The intuitive design in (a) shows the emission resulting from choosing $\Delta = 482$ nm based on the thin film emission compared to the optimized design ($\Delta = 540$ nm), whereas (b) shows emission profiles with an optimal $\Delta = 540$ nm, but the phase response has been zeroed at 50 nm (blue solid), 82 nm (dashed), and 122 nm (dotted) compared to the optimized design.

Having determined the metasurface periodicity, the second stage of the intuition-guided design heuristic is to establish a linear phase gradient corresponding to 2π phase evolution across one period. Importantly, this phase evolution represents a *relative* change between metaelements—there is no *unique* choice of phase. This metasurface system spans 4.5π in phase space, (Figure 4.8); the width (phase) of the 1st nanoribbon is arbitrary but has large effects on emission directivity. EGO-based design resolves this ambiguity. To demonstrate this, we again intuitively design a metasurface for normal exitance of s-polarized emission – this time using the optimal metasurface period of $\Delta = 540$ nm. Figure 4.3b shows the simulated emission profile of intuitive designs where the phase response arbitrarily starts with nanoribbons of 50 nm (blue solid), 82 nm (blue dashed), and 122 nm (blue dotted). We see that the intuitive design whose phase response was zeroed at 50 nm has the highest

directivity and that directivity quickly dies off as nanoribbon width increases. EGO-based design nicely handles this 'starting phase' ambiguity.

The optimized design in Figure 4.3b shows improvement above and beyond choice of Δ and phase-zeroing. This is due to small, non-intuitive changes in nanoribbon position and size which our optimization allows. Inverse design enables deviation from a linear, evenly-spaced, 2π-spanning phase-gradient. Figure 4.4 shows the spatial phase profile of an idealized, continuous unidirectional emitter (blue line) and the optimized, discrete design for each of the five cases (red dots) with vertical lines indicating where an intuitive design would discretize the continuous distribution to place a nanoribbon. Case 5 exemplifies the difficulty of the intuitive design approach. In this metasurface system, p- and s-polarized light (electric field perpendicular and parallel to the semi-infinite axis, respectively) experience different phase delays when transmitting through the same nanoribbon, see Figure 4.8. Thus, under intuitive design, some balance would need to be struck between the two phases-width calibration curves. EGO-based design allows us to sidestep this issue and design a directive emitter. Case 5 uses neither the intuitive pitch nor 2π-spanning phase gradient. In particular, Case 5 s- is much steeper than we would expect whereas Case 5 p- has a marked deviation from linear phase gradient. It is therefore unsurprising that very few works achieve simultaneous p- and s- polarized directional emission in luminescent metasurfaces.

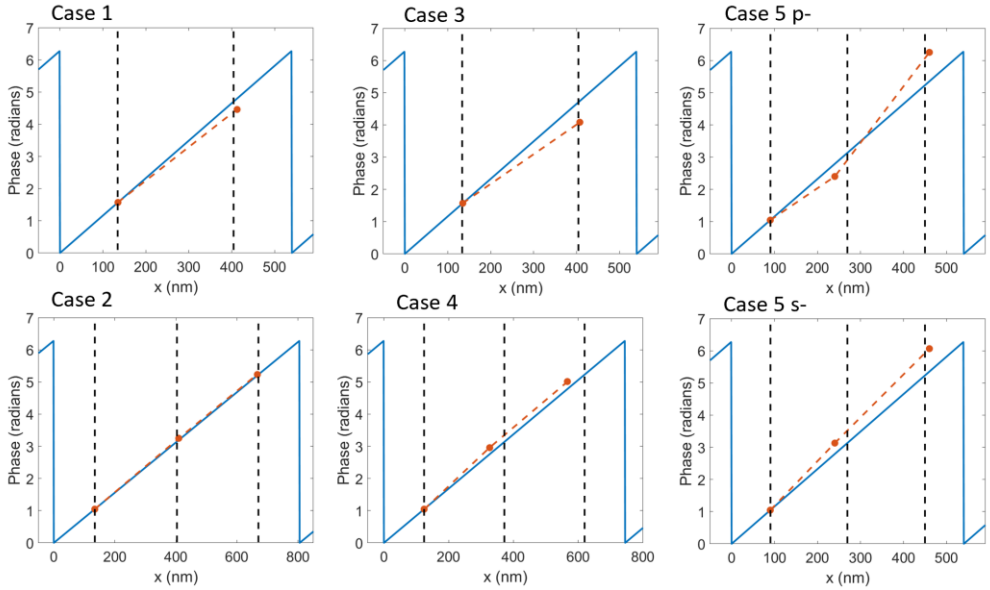

Figure 4.4. Phase maps showing a continuous linear phase distribution as well as nanoribbon location and phase for Cases 1-5.

4.4 Conclusion

In conclusion, we use reciprocal FDTD simulations and EGO to design, fabricate, and characterize highly unidirectional photoluminescent emitters. These tools grant us great control in selecting the momentum of the emission lobe and the polarization of directed emission. We achieve a 54% improvement in directivity over previous metasurfaces for p-polarized emission and first demonstrations of highly directive s-polarized emission. Further, we see that although the expanded intuitive design approach is useful for p-polarized emission, future photoluminescent metasurfaces could be better served by imagining an input momentum of $k_{||,i} = 1.00\, k_0$. Finally, we detail the non-intuitive choices that the EGO algorithm converges on to enable these highly directive metasurfaces—namely, judicious choice of Δ, first pillar size, and QW position, followed by minor changes in nanoribbon size and location.

4.5 Supporting Information

Reciprocal FDTD Simulations

Two-dimensional reciprocal simulations were performed using Ansys Lumerical FDTD. Bloch boundary conditions were used along the x axis, whereas a 24-layer, steep-angle PML boundary was used along the y axis. An override mesh was used in the QW region with 5 nm resolution along the x axis and 10 nm resolution along the y axis. Because the QW is optically thin (~5 nm) and of a similar refractive index to GaN[98] ($n_{GaN} = 2.34$ vs. $n_{QW} = 2.38$) we are able to treat the entire nanoribbon as having the index of GaN. Photoluminescence is simulated using a reciprocal method wherein a 540 nm plane wave of appropriate polarization is injected from the substrate and the resultant electric field is measured throughout the top portion of the nanoribbons (allowing us to multiplex the emission pattern of a given geometry for all QW positions via a brute force search). Because InGaN/GaN QWs can be modeled as in-plane (x-z) electric dipoles[54,96,99], only the in-plane component of these electric fields, $|E_x|^2$ for p-polarized emission and $|E_z|^2$ for s-polarized emission, are integrated across the x dimension for every quantum well position across the y-axis, i.e. $I(\theta, y) = \int |E_i(x, y)|^2 dx$. The integration excluded the outermost 10 nm of each nanoribbon, as done elsewhere[96] to account for damage to the QW during fabrication. This procedure is done for a series of plane wave source angles, $|k_x| \leq 1.3\, k_o,\ k_z = 0$, allowing us to simulate momentum-resolved emission intensity from a multitude of QW locations simultaneously.

Design of Optimization Experiment

Optimal QW position was found to strongly couple with nanoribbon height. Because this reciprocal simulation scheme interrogates many QW positions without additional time cost, nanoribbon height was fixed at 1000 nm. Parameter space was discretized into 5 nm steps and constrained such that each successive nanoribbon was wider than the last and that there was a minimum 60 nm separation between nanoribbons and 30 nm separation between the minimum (maximum) of the first (last) nanoribbon and the Bloch boundary. Periodicity, Δ, was constrained to be within ±20% of $\frac{\lambda_o}{\Delta k_{||,f} - k_{||,i}}$, where λ_o is the free space wavelength. Cases 1 and 3 (2 and 4) were chosen to have two (three) nanoribbons per unit cell to facilitate the fabrication of that number of nanoribbons within a period. The optimization of Case 5 was found to be unsatisfactory with two nanoribbons but improved when the number of nanoribbons increased to three. The training set used for the EGO model was comprised of roughly $11N$ structures, where N is the number of free parameters. These sets were randomly picked from parameter space. The algorithm calculates expected improvement for each combination of parameters based on expected value and uncertainty. A distribution of the parameter sets, including the set with maximum expected improvement were simulated and the EGO model was retrained. This process continued until convergence.

Growth

The growth of the s-polarized and p-polarized samples for photoluminescence was done by metal-organic chemical vapor deposition (MOCVD) on double side polished (DSP) sapphire. The GaN growth starts with a nucleation step at a thermocouple (TC) temperature of 560 ˚C which forms the initial 2D GaN islands on sapphire. Subsequently, 800 nm of high temp unintentionally doped (UID) GaN was grown (TC temp = 1220 ˚C) with

trimethylgallium as the Ga source. Prior to quantum well (QW) growth Ga source was switched to triethylgallium and the growth rate was reduced to promote better morphology. The single quantum well was grown at TC temp of 808 ˚C. It consists of a 0.5 nm UID GaN layer to repair surface damage during temperature ramps, a 2.5 nm $In_{0.2}Ga_{0.8}N$ QW, and a 3 nm $Al_{0.2}Ga_{0.8}N$ cap to help keep the Indium for desorbing from the QW. Subsequent, UID GaN layers were grown above the QW with slow growth rate and successive temperature ramps to promote as smooth a surface as possible. The top UID GaN thickness was adjusted such that the QW was 170 nm below the surface for the s- polarized sample, 70 nm for the p-polarized sample, and 120 nm for the both-polarized sample.

Fabrication

Samples were ultrasonically cleaned with acetone, isopropanol, and deionized water. PECVD was used to deposit approximately 400 nm of SiO_2 on the samples to serve as the hard mask for the GaN etch. An adhesion layer of titanium, followed by 30 nm of ruthenium, and another adhesion layer of titanium were sputtered on top of the SiO_2 layer to act as a hard mask for the SiO_2 etch. Subsequently, a layer of electron beam resist (2% hydrogen silsesquioxane) was spun on at 5000 revolutions/minute and the samples were baked at 110 °C for 45 s. After exposure, the samples were developed in a 25% tetramethylammonium hydroxide solution for 60 s and rinsed with deionized water. The ruthenium hard mask was removed using inductively coupled plasma with O_2/Cl_2 chemistry. The SiO_2 hard mask was removed using inductively coupled plasma with CF_4/CHF_3 chemistry. We then repeated the same ruthenium etch as before and etched the GaN using N_2/Cl_2 chemistry. This etch recipe resulted in extremely vertical nanoribbons[72]. The remaining SiO_2 hard mask was removed using buffered hydrofluoric acid.

Energy-Momentum Resolved Measurements

Samples were optically pumped with uniform illumination through a 1.3-NA oil-immersion objective (Nikon 100x 1.3 NA Plan Fluor) using a 405-nm LED (ThorLabs M405L3). Photoluminescence was collected through the same objective and pump light was filtered using a a 405-nm long-pass filter cube set (Semrock). Energy-momentum images of photoluminescent emission were produced by re-imaging the back-focal-plane onto the entrance slit of an imaging spectrometer (Princeton Instruments Iso Plane SCT320 with Princeton Instruments PIXIS 1024BRX) after passing through an analyzing polarizer.

Phase Delay Calculations

Two-dimensional simulations were performed using Ansys Lumerical FDTD. Periodic boundary conditions were used along the x axis, whereas a 24-layer, steep-angle PML boundary was used along the y axis. An override mesh was used with 5 nm resolution along the x-axis and a 540 nm plane wave of appropriate polarization is injected from above a single nanoribbon. The phase of the appropriate electric field is measured in the sapphire substrate. This procedure is done for a series of nanoribbon widths.

Table 4.2: Parameters of optimized metasurfaces and their calculated directivity where $k_{||,t}$ is the target final momentum

Case	$k_{\|\|,t}$ (k_0)	x_1 (nm)	w_1 (nm)	x_2 (nm)	w_2 (nm)	x_3 (nm)	w_3 (nm)	Δ (nm)	D (sim.)	D (exp.)
1	0.00	133	145	410	190			540	8.63	5.49
2	-0.34	120	140	395	170	662	235	805	7.03	4.55
3	0.00	65	50	338	75			540	4.19	3.83
4	-0.34	135	70	338	95	578	135	745	2.91	2.37
5 p-	0.00	65	50	215	70	435	110	540	4.58	2.34
5 s-	0.00	65	50	215	70	435	110	540	3.17	3.76

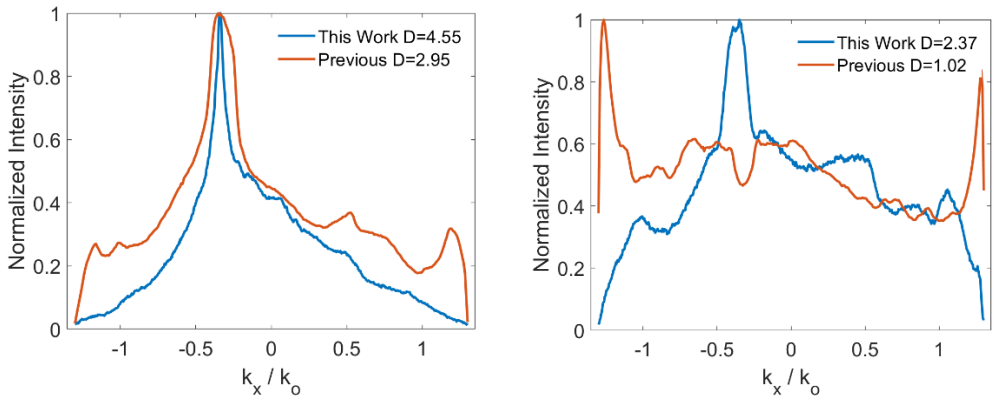

Figure 4.5: Emission patterns for metasurfaces intended to emit at 20°. p-polarized emission (left) for Case 3 (blue) shows a 54% increase in directivity over previous work in a similar system (red). s-polarized emission (right) for Case 4 (blue) shows a 232% increase in directivity over previous work in a similar system (red).

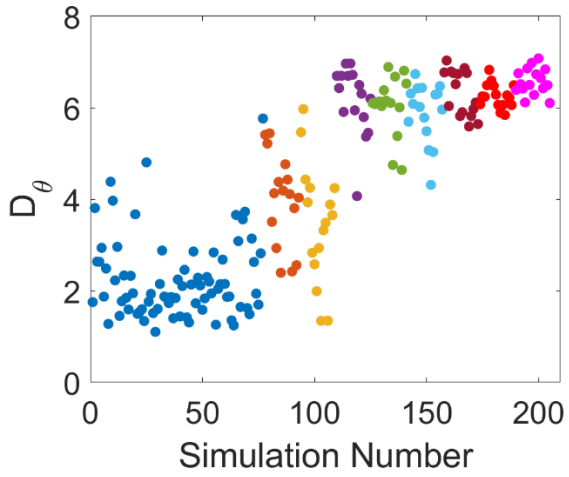

Figure 4.6: Typical optimization achieved via EGO as a function of simulation number. Each 'training group' is mapped to a color. Case 2, shown here, used 77 training simulations (blue). The algorithm then calculated expected improvement scores and sets of 16 designs were simulated and added to the training data. EGO discovered the optimal design in the third prediction (purple).

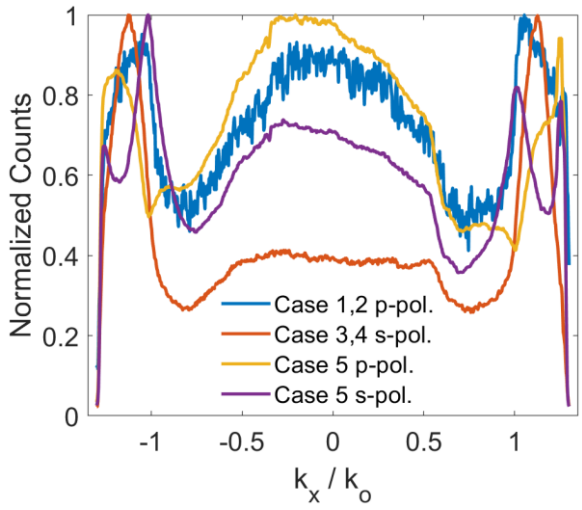

Figure 4.7: Momentum resolved emission patterns at 540 nm for the thin films from which each of the five optimized metasurfaces were fabricated.

Additional Details for Simulations in Figure 4.3a

For ease of comparison against the optimized structure, this simulation discretized the phase distribution into two nanoribbons centered exactly on a $\frac{\Delta}{2} = 241$ nm pitch. We determine the expected phase response of nanoribbons on this 241 nm pitch as a function of nanoribbon width, see Figure 4.8 and construct our unit cell such that we sample 2π radians of phase linearly across space, i.e. such the phase response of the second pillar, $\varphi_2 = \varphi_1 + \pi$. The choice of the width of the first nanoribbon is arbitrary, but again, for ease of comparison with the optimized design, we will pick the first nanoribbon to be 50 nm wide.

Additional Details for Simulations in Figure 4.3b

This simulation discretized the phase distribution into two nanoribbons centered exactly on a $\frac{\Delta}{2} = 270$ nm pitch. We determine the expected phase response of nanoribbons on this 270 nm pitch as a function of nanoribbon width sample 2π radians of phase linearly across space, i.e. such the phase response of the second pillar, $\varphi_2 = \varphi_1 + \pi$.

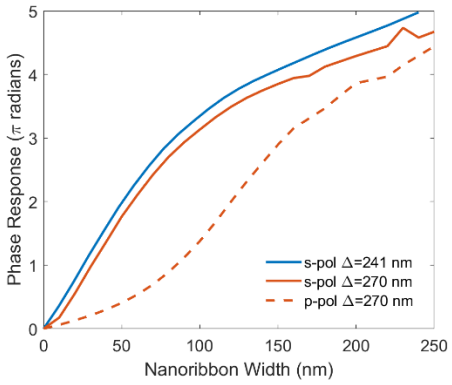

Figure 4.8: Metaelement phase response versus nanoribbon width for nanoribbons on different pitches and under different illumination polarizations. s-polarized indicates that the electric field is parallel to the semi-infinite axis, whereas p-polarized has the electric field perpendicular to the semi-infinite axis.

Chapter 5: High Efficiency Large Angle Polarization Insensitive Retroreflecting Metasurface for Magneto-Optical Traps

5.1 Abstract

Magneto-optical traps (MOTs) are integral components of atomic clocks, quantum computers and other cold-atom science applications. Conventional MOTs occupy a large volume and suffer from limited portability. Efforts to build MOTs using integrated photonics promise to dramatically reduce the size and weight of these systems allowing applications beyond the lab. However, the need for counterpropagating beams currently necessitates free-space angled mirrors that limit overall integration and add substantial size and weight to the MOT. Replacing these mirrors with planar retroreflecting metasurfaces provides a route to achieving a complete MOT within a single integrated planar package. Here, we design and demonstrate optical frequency retroreflecting metasurfaces that function at large angles and preserve the necessary circular polarization. Specifically, we utilize Bayesian optimization to design an amorphous silicon (a-Si) on gold metasurface for high efficiency polarization insensitive retroreflection of 780 nm circularly polarized light at 54.7°. Numerical simulations demonstrate maintenance of circular polarization after highly efficient retroreflection ($\epsilon_{-1} = 1.10,\ R_{-1} = 0.86$). Experimentally, we demonstrate similarly excellent performance at 736 nm at $50.3°$ and show that deviation from the target design is due to oxidation of the a-Si metaelements. We conclude by discussing mitigation strategies for future devices and propose a corrective optic for the currently fabricated device. This work represents a step

toward the miniaturization of magneto-optical traps and expansion of cold-atom science beyond the laboratory.

5.2 Introduction

Phased array metasurfaces are an integral part of next-generation optical assemblies[13,100,101]. Metasurfaces enable engineers to reduce the size and weight of various optical components while granting arbitrary and granular control over the wavefront of light[15,35]. Phased array metasurfaces have been developed as beam deflectors[76,83,102,103], lenses[81,93,104], vortex-beam generators[5,105], hologram generators[3,4,85], and more[13,72,96,97,101]. Another optical component - retroreflectors, which reflect light back along its incident path - are a critical part of modern science with applications including e.g., spectroscopy[106], telecommunications[107], and surveying[108,109].

Retroreflectors are employed in atom trapping and cooling systems such as atomic clocks[110], quantum computing[111,112], and quantum sensing[113,114] where counter-propagating beams are required. Most systems for atom trapping use free-space optics and lasers and occupy a large portion of an optics table, requiring large initial investments and regular maintenance. The eventual miniaturization of these systems may enable portability, lower cost, and improve resilience for their use in inertial navigation[113], gravity mapping[114], and space-based atomic clocks[110].

Three-dimensional magneto-optical traps (MOTs) use six counterpropagating beams to produce a balance of radiation forces at the null of a magnetic field gradient within a vacuum cell[115–118]. Past efforts to miniaturize[119] beam delivery include the use of pyramidal mirrors[120,121] and diffraction gratings[122–124] as well as metasurface beam deflectors[125,126], but

these schemes still utilize bulk optics for beam expansion, limiting the minimum size of the setup. Recently, atom trapping and cooling of ^{87}Rb was demonstrated using a fiber-coupled photonic integrated chip for beam delivery and expansion – thereby shrinking the volume required to inject three beams to a flat surface coupled to a fiber[127]. However, this design still required the alignment of individual mirrors to achieve counter propagation. Replacing these bulky mirrors with a retroreflecting metasurface would eliminate time-consuming alignment and decrease the mass and footprint of optical components to the size of the vacuum cell where injection and reflection are handled by integrated optics.

In this paper, we present the design, fabrication, and characterization of a retroreflecting metasurface to replace traditional angled mirrors and, in conjunction with a photonic integrated chip, allow for system miniaturization, as shown in Figure 5.1a. Such a retroreflecting metasurface would need to function at a large angle for circularly polarized light at optical frequencies, i.e. possess equally large reflection efficiency for p- and s-polarized light without introducing an additional relative phase delay between the polarizations. Single angle retroreflecting metasurfaces have been simulated and experimentally demonstrated at radio[128–132] and visible[102,133] frequencies for a variety of incident angles, but to the best of the authors' knowledge, there has not been demonstration of a metasurface which displays the polarization insensitivity required for retroreflection of circularly polarized light. Most demonstrations featured unique metasurface designs for each linear polarization[128,129,132,133] or demonstrated polarization conversion[130,131]. Multiangle retroreflecting metasurface has also been demonstrated[134], but that metasurface suffered dramatic efficiency loss and polarization sensitivity as incident/reflection angle grew. This work describes a single angle retroreflecting metasurface.

Here, we utilize Bayesian optimization to design a metasurface with high efficiency polarization-insensitive retroreflection of 780 nm circularly polarized light incident at 54.7°. We note that the process is largely angle and wavelength agnostic; the design parameters having been informed by a specific atomic system and existing photonic chip. After fabrication and characterization, we demonstrate excellent performance at 736 nm operating wavelength and 50.3° incidence angle and show that deviation from target design is due to oxidation of the a-Si metaelements. This work represents first steps toward improving miniaturization of MOTs through full integration of optical components within the vacuum cell.

5.3 Results and Discussion

5.3.1 Operating principle

Metasurface retroreflection is achieved via anomalous reflection. Consider an incident plane wave with normalized transverse momentum, $\frac{k_{||,i}}{k_0} = n\sin(\theta_i)$. The retroreflector imparts additional transverse momentum such that the reflected wave has normalized transverse momentum $\frac{k_{||,r}}{k_0} = n\sin(-\theta_i)$ where k_0 is the free space momentum, n is the refractive index of propagation medium, and θ_i is the angle of incidence. The normalized metasurface momentum, $k_M = k_{||,r} - k_{||,i}$, is defined by the metasurface period, Δ, such that $\frac{k_M}{k_0} = \frac{\lambda_o}{\Delta}$, where λ_o is the free space wavelength. The intended application sets $\lambda_o = 780$ nm and $\theta_i = 54.7°$, such that each of the three beams beam from the PIC are mutually orthogonal at the atom trap. Thus, we employ a metasurface with 478 nm period. The metasurface comprises two different-sized rotationally symmetric rounded square a-Si nanopillars atop a SiO_2

spacing layer atop a gold back plane (Figure 5.1b). Square nanopillars were chosen to minimize polarization sensitivity and the corners of the nanopillars were rounded with a 30 nm radius of curvature owing to fabrication limits.

5.3.2 Simulation and Optimization

We design the metasurface using an inverse design-based Efficient Global Optimization (EGO) algorithm[50]. EGO is a Bayesian optimization method which builds a surrogate model from a database of fitness observations. It then uses this surrogate model to determine which new designs should be tested. As EGO is a parametric optimization tool, we first define our metasurface parameters. We use eight parameters: the thickness of the gold back plane (h_{Au}), the thickness of the SiO_2 spacing layer (h_{SiO2}), the height of the a-Si nanopillars (h_{Si}), the side length of each of the three nanopillars (w_i), and the position of the last two nanopillars (x_i). Although there is a small loss in generality, we fixed the first nanopillar position to avoid optimization degeneracies due to translational symmetry. We further define an objective function to account for the major goals of our system: first, to maximize the reflection coefficient of the $m = -1$ diffraction order (R_{-1}),; and second, to minimize the ellipticity of the polarization ellipse of the retroreflected light, $\epsilon_{-1} = \frac{b}{a}$, where b and a are the length of the semiminor and semimajor axis of the polarization ellipse, respectively. Thus, our objective function is $f = \frac{R_{-1}}{\epsilon_{-1}}$.

The simulations and optimization were performed as described in Section 5.5. Although we began the optimization process with three-pillars per unit cell, the algorithm rapidly converged on nonsymmetric two-pillar designs, similar to other reported results[44]. Ultimately, the optimization converges to a design with $f = \frac{R_{-1}}{\epsilon_{-1}} = \frac{0.86}{1.10} = 0.78$ (metasurface

parameters are shown in Table S1). This represents a near unity retroreflection efficiency with remarkable retention of circular polarization. Given that the total reflectivity is 90% ($R_t = 0.90$), due to absorption in the gold backplane and Si nanopillars—the diffractive efficiency into the desired retroreflection mode is quite good (> 96%).

In addition to rapid convergence, a major benefit of EGO is that it provides an estimate of model sensitivity to each parameter[50] and thereby provides information regarding required fabrication tolerances. In this system, EGO indicates that the figure of merit is most sensitive to w_3, h_{Si}, and h_{SiO2}. Thus, fabrication must ensure close adherence to those parameters with greater room for error in the other parameters.

5.3.3 Characterization

Figure 5.1c shows an SEM of the fabricated optimized design. Top-down SEMs images were used to determine the metasurface nanopillar sizes and positions whereas cross sectional SEM images provide layer thickness information. The fabricated nanopillars are slightly longer in the direction perpendicular to the phase gradient than in the direction parallel to the phase gradient, i.e. the fabricated nanopillars are rounded rectangular prisms (instead of square prisms). The measured metasurface parameters are presented in Table S1. As required by EGO sensitivity analysis, w_3, h_{Si}, and h_{SiO2} are within 1% of the design values, whereas other parameters are within 10%. Performing a simulation based on these measured parameters results in a figure of merit of $f = \frac{R_{-1}}{\epsilon_{-1}} = \frac{0.87}{1.06} = 0.82$, supporting the sensitivity predictions made by EGO.

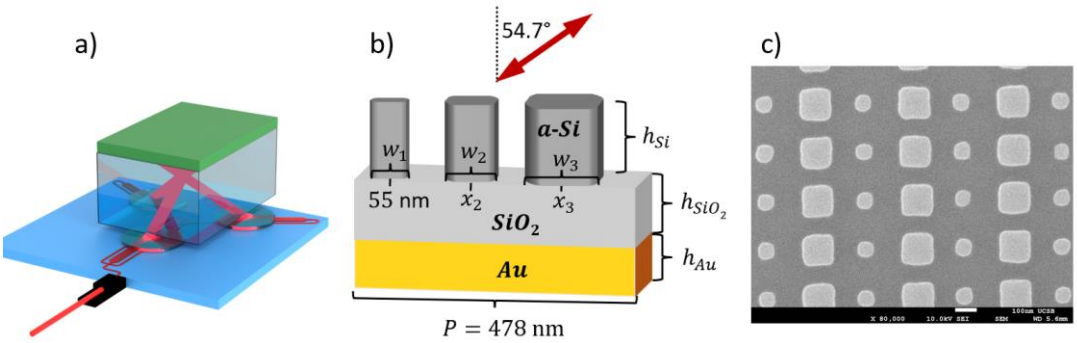

Figure 5.1: (a) Schematic of magneto-optical trap where the blue photonic integrated chip injects three red beams into a transparent vacuum cell. These beams are then retroreflected by the green metasurface allowing for six counterpropagating beams to intersect at the center of the cell. The use of flat optics integrated with the vacuum cell allow ~3 orders of magnitude volume reduction over conventional benchtop setups. (b) Schematic of metasurface for optimization featuring three amorphous Si nanopillars on a SiO_2 spacing layer on a gold back plane. The incident wavelength and angle determine the periodicity whereas the height of each layer as well as the position and width of each nanopillar are set as free parameters. (c) SEM of fabricated metasurface based on the optimized design with only two nanopillars per unit cell.

The fabricated metasurface was characterized using a custom setup detailed in Figure 5.6. For polarization-dependent intensity measurements (Figure 5.6a), 780 nm light from a supercontinuum fiber coupled laser (SuperK Select, NKT Photonics) is focused onto the metasurface which is mounted on a rotation stage setting the angle of incidence to 54.7°. Retroreflected light is recollimated by the lens and directed to a power meter by a 50/50 nonpolarizing beam splitter. A polarizer and analyzer allow for determination of s-, p, and cross-polarized retroreflection coefficients. Reflected power is normalized against a commercial silver mirror. We find the polarization dependent intensity retroreflection coefficients to be: $R^{s}_{-1} = 0.91$, $R^{p}_{-1} = 0.52$, and $R^{ps}_{-1} = R^{sp}_{-1} = 0.00$.

Next, we use polarimetry and Jones calculus to extract the phase relationships. In the most general form, we can write the Jones matrix J of any arbitrary optical component[135,136] as

$$J = \begin{bmatrix} r^p e^{i\Phi^p} & r^{ps} e^{i\Phi^{ps}} \\ r^{sp} e^{i\Phi^{sp}} & r^s e^{i\Phi^s} \end{bmatrix} \tag{5.1a}$$

where r^i is the p-, s-, and cross-polarized electric field amplitude reflection coefficient and Φ^i is the phase delay for the various polarization states. Having measured the intensity retroreflection coefficients, we are able to reduce Equation 5.1a to

$$J = \begin{bmatrix} \sqrt{R_{-1}^p} & 0 \\ 0 & \sqrt{R_{-1}^s} e^{i\Phi} \end{bmatrix}, \tag{5.1b}$$

which has only one free parameter, Φ, the relative phase delay between s- and p- polarized light.

To simplify the analysis and avoid phase artifacts from the beam splitter and focusing lens, we spatially separate the incident and 'retroreflected' beams by misaligning the metasurface by 2°. Removing the focusing lens results in overfilling the metasurface which impacts the absolute intensity, but does not affect the relative phase between polarizations, which is the measurement goal of this second experimental characterization (Figure 5.6b). 'Retroreflected' power is measured as a function of analyzer angle and fit to Equation 5.2:

$$\begin{bmatrix} E_x^f \\ E_y^f \end{bmatrix} = \frac{P}{\sqrt{2}} k \begin{bmatrix} \cos^2\alpha & \sin\alpha\cos\alpha \\ \sin\alpha\cos\alpha & \sin^2\alpha \end{bmatrix} \begin{bmatrix} \sqrt{R_{-1}^p} & 0 \\ 0 & \sqrt{R_{-1}^s} e^{i\Phi} \end{bmatrix} [QWP] \begin{bmatrix} 1 \\ 1 \end{bmatrix} \tag{5.2}$$

where P is the illumination power, k is a fitting term to account for the overfilling of the metasurface, α is the angle of the analyzer, and $[QWP]$ is the Jones matrix of a commercial quarter wave plate. The measured and fit data is displayed in Figure 5.2a. Using the amplitude values found above, the fit determines $\Phi = 14°$, that is, the metasurface introduces an additional 14° phase shift in addition to the 90° inherent to circularly polarized light. Having extracted these fitting parameters, we reconstruct the polarization ellipse corresponding to the final state of circularly polarized light after being retroreflected from the metasurface, as seen

in Figure 5.2b. We can now determine the ellipticity of retroreflected light and see that $f = \frac{R_{-1}}{\epsilon_{-1}} = \frac{0.72}{1.46} = 0.49$, reduced from the $f = 0.82$ expected in simulation.

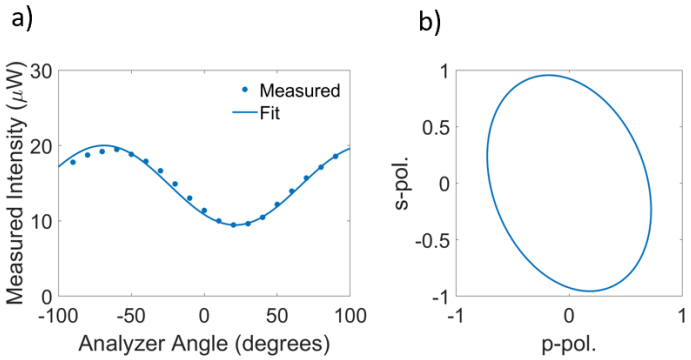

Figure 5.2: (a) Measured intensity vs analyzer angle for fabricated device along with fit line. (b) Polarization ellipse of circularly polarized light after having been retroreflected, showing a major axis 1.46 times larger than the minor axis.

The discrepancy in functionality between simulation and experiment is due to unintentional polarization sensitivity and can be traced to oxidation of the a-Si nanopillars. This mechanism becomes clear when we consider the near field profiles shown in Figure 5.3. Incident p-polarized light, driving E_x and E_z, establishes a y-oriented magnetic resonance mode within the larger nanopillar, whereas incident s-polarized light, driving E_y, produces a y-oriented electric resonance inside the oxide spacing layer beneath the smaller nanopillar. From this, we expect that p-polarized light will be more sensitive to perturbations in the nanopillar geometry than s-polarized light, explaining the larger discrepancy in p-polarized retroreflection amplitude when compared to simulations. Given the material system at play, a natural assumption is that the a-Si nanopillar has oxidized slightly[53,54], resulting in a smaller mode volume and decrease in resonant wavelength[55–57]. Such an oxide, or other low index layer may have grown during the dry etch steps[142].

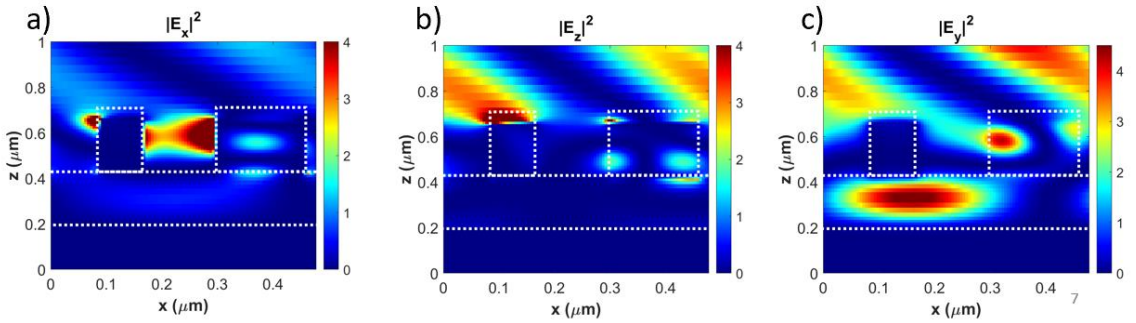

Figure 5.3: Near field electric intensity profiles for p- (a and b) and s-polarized (c) light in a unit cell of the metasurface. Dotted lines represent material boundaries. The electric field is concentrated almost entirely in the larger nanopost for p-polarized light, whereas s-polarized light establishes a resonance in the SiO_2 spacing layer.

To explore this possibility, additional simulations were performed where the outermost few nanometers of the nanopillars were replaced with oxide while maintaining the overall size and position of the metaelements as measured with SEM. In these simulations, the circularly polarized plane wave source was replaced with either p- or s- polarized light. The results of these simulations are reported in Figure 5.4a where we see that the retroreflection coefficient for s-polarized light is more resilient to SiO_2 growth than p-polarized light. In fact, we see that if 11 nm of the a-Si has oxidized, we reproduce the measured polarization specific retroreflection coefficients.

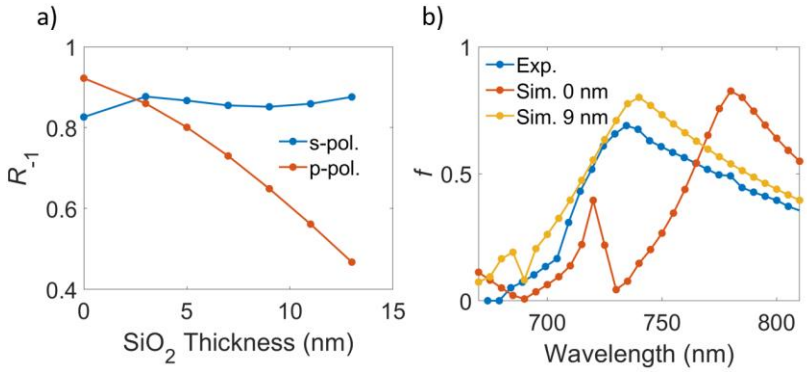

Figure 5.4: (a) Simulated retroreflection coefficients for s- and p-polarized 780 nm light vs oxide thickness. p-polarized light is highly sensitive to oxide thickness, whereas s- remains largely unaffected by oxide growth. (b) Wavelength dependent figure of merit for

fabricated metasurface shows excellent agreement with a simulated metasurface with 9 nm oxide thickness. Also see that operational wavelength decreases as the oxide grows.

We can confirm this suspicion experimentally by measuring the figure of merit as a function of wavelength. The procedure for broadband measurement and analysis is similar to the single-wavelength procedure detailed above, but the angle of incidence is changed to achieve retroreflection for each incident wavelength. The result of these measurements is displayed in Figure 5.4b where we see excellent agreement between experiment (blue) and simulation given a 9 nm oxide layer (yellow). For reference, the 0 nm SiO_2 case (red) is also shown, displaying a maximum at 780 nm as designed. Thus we conclude that as the nanopillars oxidize, the mode volume decreases resulting in shorter operational wavelengths, such that optimal performance is achieved at 736 nm where the angle of incidence is $50.3°$, $R_{-1}^{p} = 0.74$, $R_{-1}^{s} = 0.73$, $\Phi = 2°$, and $f = \frac{R_{-1}}{\epsilon_{-1}} = \frac{0.73}{1.04} = 0.70$. This figure of merit represents nearly perfect polarization insensitivity, allowing retroreflection of circularly polarized light with slight absorption in the a-Si nanopillars and gold backplane.

These results highlight the effect that oxide growth can have on silicon-based metasurfaces. Care should therefore be taken in the design to either avoid oxidation or build in tolerance. For instance, the a-Si nanopillars could be replaced with TiO_2 nanopillars, avoiding oxidation concerns entirely. Alternatively, an etch stop, like Al_2O_3 could be placed between the oxide spacing layer and the nanopillars to allow for removal of plasma induced oxide. Also the nanopillar size could be increased to account for the inevitable oxidation under ambient atmosphere. Yet another option would be to optimize the figure of merit over a broader bandwidth to minimize the sensitivity to metaelement size.

Lastly, it is worth noting that the fabricated metasurface displays a very large retroreflection coefficient for s-polarized light at 780 nm, as designed. The incorporation of an off-axis quarter waveplate as a corrective optic could see this metasurface function at the design wavelength where the off-axis quarter waveplate converts incoming and outgoing light between circular- and s- polarized before and after retroreflection. With that said, the metasurface presented here functions as a polarization-insensitive, large angle retroreflector at 736 nm. This metasurface maintains the polarization of incident light after reflection, allowing for retroreflection of circularly polarized light as required for miniaturized magneto-optical traps.

5.4 Conclusion

In summary, the further miniaturization of magneto-optical traps requires a flat optical component capable of large angle polarization-insensitive retroreflection. We have utilized inverse design to optimize such a metasurface. Simulations show excellent performance, with $f = \frac{R_{-1}}{\epsilon_{-1}} = \frac{0.86}{1.10} = 0.78$, indicating a design that maintains circular polarization after very efficient retroreflection. Experimental characterization of fabricated metasurfaces show good performance, with $f = \frac{R_{-1}}{\epsilon_{-1}} = \frac{0.73}{1.04} = 0.70$, at a shifted wavelength (736 nm) and agrees well with simulations where the a-Si meta-elements have undergone oxidation. We discuss various mitigation strategies for future metasurface retroreflectors and propose a corrective optic for the currently fabricated device. This work represents a first step toward the miniaturization of magneto-optical traps and expansion of cold-atom science beyond the laboratory.

5.5 Supporting Information

Retroreflector Simulations and Optimization

Lumerical FDTD was used for all simulations in this work. Metasurfaces representing a random sampling of parameter space were simulated under a circularly polarized 780 nm source at $54.7°$. These random points in parameter space and their figures of merit comprise the initial database of fitness observations (training data). Parameter space was constrained to avoid contact between neighboring nanopillars and to ensure that each nanopillar is successively larger. It was also constrained to only sample every 5 nm for x_i, w_i and every 10 nm for h_i to account for fabrication tolerances. A 5 nm mesh override region was placed around the nanopillars. R_{-1} was determined by multiplying the fraction of light in the retroreflected mode by the total reflection coefficient, as measured by light transmitted through a frequency-domain field and power monitor placed above the source. ϵ_{-1} was determined by dividing the major axis of the polarization ellipse of the retroreflected light by its minor axis. After the database was constructed, the EGO model was trained, then new batches of parameter sets were recommended, simulated, and added to the database. This process was repeated until the expected improvement of new recommendations dropped to less than 0.01. Later simulations with oxidized nanopillars used a 3 nm mesh override region, and changed input angle and wavelength.

Retroreflector Fabrication

Silicon substrates were sonicated in progressive baths of acetone, isopropanol, and water. After cleaning, we sputtered a titanium adhesion layer followed by a 200 nm gold layer atop the silicon substrate. We then grew a 220 nm SiO_2 layer and a 241 nm a-Si layer via

plasma enhanced chemical vapor deposition. SiO_2 and Si layer thicknesses were measured after deposition by ellipsometry whereas gold thickness is extrapolated based on a growth rate calibration. We then sputtered a 12 nm ruthenium hard mask (again preceded by a titanium adhesion layer), spun a 2% HSQ electron beam resist at 5000 rpm and baked at 110° C for 60 seconds, and performed electron beam lithography. We developed the resist in 25% TMAH and etched the ruthenium mask using an inductively coupled plasma with oxygen/chlorine chemistry. We then performed a short SiO_2 etch (CHF_3/ CF_4 inductively coupled plasma chemistry) to remove any native oxide and the exposed HSQ above the Ru hard mask. We etched the exposed Si in $C_4F_8/SF_6/CF_4$ and removed the Ru hard mask using the first etch recipe.

Table 5.1: Parameters of optimized and fabricated metasurface where fabricated nanopillars deviated from square prisms into rectangular prisms, such that nanopillar length, w_y, has been added to nanopillar width, w.

Optimized	x (nm)	w (nm)	h_{Si} (nm)	h_{SiO2} (nm)	h_{Au} (nm)
Nanopillar 1	55	0	240	220	200
Nanopillar 2	125	80			
Nanopillar 3	375	160			

Fabricated	x (nm)	w_x (nm)	w_y (nm)	h_{Si} (nm)	h_{SiO2} (nm)	h_{Au} (nm)
Nanopillar 1	55	0	0	241	220	170
Nanopillar 2	125	84.8	89.2			
Nanopillar 3	354	157.9	161.8			

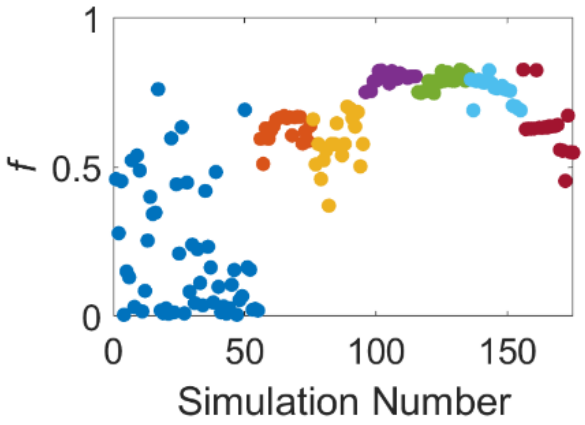

Figure 5.5: Typical optimization achieved via EGO as a function of simulation number. Each 'training group' is mapped to a color. The training data (blue) comprises 55 simulations. The algorithm then calculated expected improvement scores and sets of 16 designs were simulated and added to the training data. EGO discovered the optimal design in the third prediction (purple).

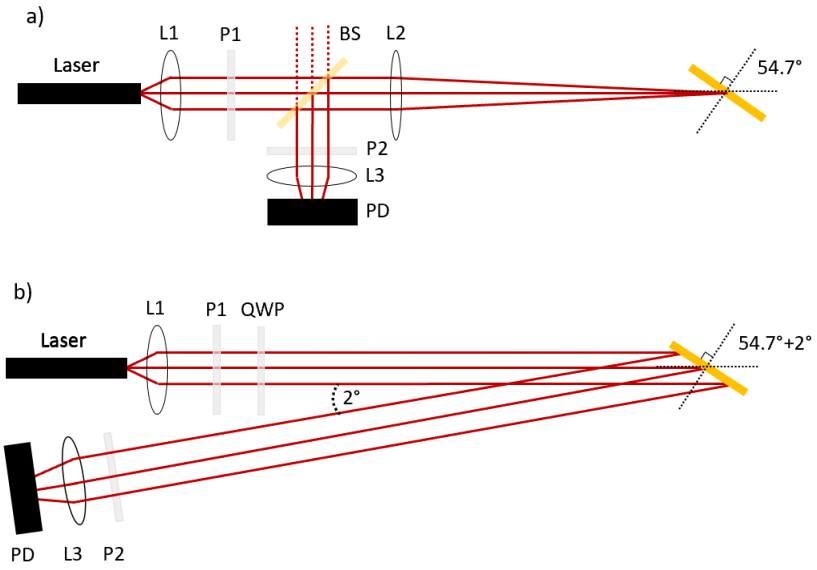

Figure 5.6: Schematic of optical setups used for metasurface characterization. (a) Light from a supercontinuum fiber coupled laser (SuperK Select, NKT Photonics) is collimated (L1, f=25 mm), passed through a polarizer (P1), then focused (L2, f=300 mm) on the off-axis metasurface. Retroreflected light is recollimated (L2), redirected by a beam splitter (BS), and then loosely focused (L3, f=30 mm) on a photodiode (PD). The polarizers (P1, P2) can be rotated to measure s-, p-, or cross-polarized retroreflection intensity coefficients. (b) As above, but the beam splitter and second lens have been removed and the metasurface has

been misaligned by 2°. These changes allow for polarimetric analysis of phase information without phase distortions from excess optics.

Off-axis Quarter Wave Plate Simulation

An off-axis quarter wave plate metasurface is a conceptually simple optic. A quarter wave plate, traditionally, is a slab of birefringent material cut to an appropriate thickness such that the ordinary and extraordinary rays accumulate $\frac{\pi}{2}$ relative phase. This can be accomplished in a dielectric metasurface by use of a periodic array of semi-infinite nanoribbons whose geometrical properties are tuned to retard s-polarized light (polarized parallel to the semi-infinite axis) $\frac{\pi}{2}$ relative p-polarized light (polarized perpendicular to the semi-infinite axis).

Owing to its relative simplicity, optimization for the off-axis quarter waveplate metasurface was achieved from a brute force search over its parameter space. Parameter space for the off-axis quarter wave plate comprised only the height and width of the metaelement, which was chosen to be a semi-infinite nanoribbon of a-Si on SiO_2 as shown in Figure 5.7. The periodicity was fixed at 160 nm, well below the free space wavelength, to prevent high order diffraction modes. Simulations were run in Lumerical FDTD with a circularly polarized 780 nm source incident at 54.7° on a metasurface unit cell using Bloch boundary conditions. We define the objective function for this metasurface to account for its major goals: first, to maximize the ellipticity of the transmitted light, ϵ_t, and second to maximize overall transmission, T_t. Thus, the objective function for this optic is $f = \left(1 - \frac{1}{\epsilon_t}\right) * T_t$, where f has been constructed to avoid a possible infinity present in the more straightforward $g = \epsilon_t T_t$.

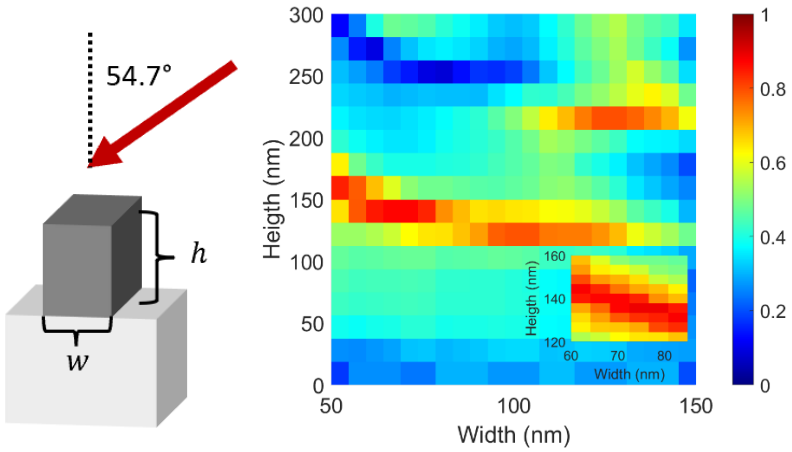

Figure 5.7: (left) Schematic representation of metasurface unit cell. (right) Brute force optimization showing figure of merit as a function of nanoribbon height and width. Inset shows a higher resolution search near a maximum.

Off-axis Quarter Wave Plate Fabrication

Fabrication of the off-axis quarter wave plate involved the same cleaning steps as for the retroreflector, but the substrate was 1 mm thick fused silica windows. A 125 nm a-Si layer was grown via plasma enhanced chemical vapor deposition and 1:2 ma-N electron resist was spun on at 5000 rpm and baked at 120° C for 60 seconds. A 10 nm layer of aluminum was thermally evaporated atop the ma-N to help dissipate charge during electron beam lithography. After exposure, the aluminum layer and resist were etched/developed in MIF300 for 60 seconds beyond the time required to etch the aluminum. The a-Si was etched in $C_4F_8/SF_6/CF_4$ inductively coupled plasma, and the remaining resist was removed using O_2 plasma.

Chapter 6: Conclusion and Outlook

In this work we have leveraged physics-based design intuition and machine learning to develop a robust design process for next-generation optical devices. We have detailed the design, simulation, fabrication, and characterization of multiple metaoptics with state-of-the-art properties. First, we detailed our work on unidirectional emitters or luminescent beam deflectors which had previously shown unexplained polarization dependent emission characteristics. We determined the polarization disparity is partially due to the difference in phase of induced dipoles from disparately oriented source dipoles. We then validated the accuracy of reciprocity-based simulations and used our new design tool to predict momentum resolved emission patterns from luminescent metasurfaces with a variety of emitter types, including out of plane electric dipoles. Finally, we identified the importance of QW position in ensuring directional emission for each polarization and emitter type.

It was discovered during validation that the simulations agreed better with experiment if the outermost 10-20 nm of each nanopillar was excluded from the integration. Physically, we suspect that the etching step may have damaged these region of the quantum well, preventing luminescence, see Appendix A. Pump power-dependent measurements were inconclusive, but we recommend cathodoluminescence measurements be made to tease out the validity of this hypothesis. Additionally, work with two-dimensional hybrid organic-inorganic perovskites has shown that butylammonium lead iodide displays strong magnetic dipole emission[143]. Attempts were made to couple and steer this unconventional emission, but no designs were found that were deemed fabricable, see Appendix D.

In Chapter 4, we combined the reciprocal simulation strategy from Chapter 3 with a Bayesian optimization algorithm to design metasurfaces capable of highly unidirectional emission for arbitrary target momentum and polarization. We then fabricated and characterized five metasurfaces, achieving a 54% improvement in directivity over previous metasurfaces for p-polarized emission and the first demonstration of highly directive s-polarized emission, including first-ever simultaneous directivity for s- and p-polarized emission. Using these optimized metasurfaces, we expand and refine intuitive design heuristics for unidirectional emitters.

The tools developed in this work can be adapted for the design of arbitrary emission patterns. Directivity has heretofore only been characterized in the direction parallel with the phase gradient. Emission in the perpendicular direction has been largely ignored. Further studies should seek to increase directivity across the whole emission space, potentially into the lasing regime. Other studies could be made to design metasurfaces with multilobe emission profiles[125]. Work has already been done to simulate[97] and optimize electroluminescent unidirectional emitters, see Appendix C and D. Further work is needed to bring the optimized designs to fruition. Fabrication challenges for electroluminescent metalenses might be overcome by using nanohole-type metasurfaces[24]. Electroluminescent metasurfaces are in many ways a more practical platform for the further development of the field and have applications from augmented reality to LiDAR.

In Chapter 5, we detailed work toward a polarization insensitive anomalous reflector for the miniaturization of magneto-optical traps. This metaoptic is capable of retroreflecting circularly polarized 736 nm light at $50.3°$ without inducing phase or amplitude distortion in the reflected light. Further work is needed to eliminate or overcome the resonance shift

induced by oxide growth. Multiple suggestions were made in Chapter 5 and will not be repeated here. Instead, we will note that trapped atom number scales with beam size[127]. Thus, to make a practical device, the metasurface array size would need to increase to ~1 cm^2, up from the current ~0.02 cm^2. A practical optical element would also benefit from having three metasurface arrays fabricated onto a single wafer, such that each beam from the photonic integrated circuit could be retroreflected using a single optical component.

Appendix A: The Reciprocity Theorem and its Applications to Luminescence Simulations

A.1 Lorentz Reciprocity

As stated in Chapter 2, reciprocity was a key facet of this work. The following is a derivation of Lorentz reciprocity[34,53,73,74,80,144–146]. Consider a region, V, bounded by S, containing two sets of sources, J_1 and J_2 which each produce fields E_1, H_1 and E_2, H_2 as seen in Figure A.1. No assumptions have yet been made about the shape, size, or topography of V.

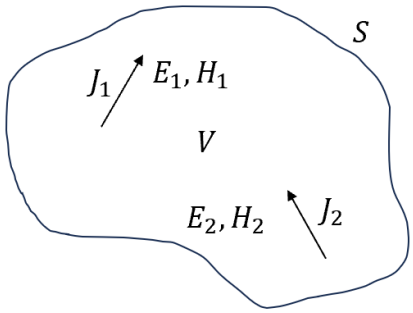

Figure A.1: A volume, V, of arbitrary size and shape bounded by a surface, S, containing two sources, J_1 and J_2

Consider the quantity:

$$\nabla \cdot (E_1 \times H_2 - E_2 \times H_1), \tag{A.1}$$

which we can expand using vector identities:

$$\nabla \cdot (E_1 \times H_2 - E_2 \times H_1) = \tag{A.2}$$

$$(\nabla \times E_1) \cdot H_2 - (\nabla \times H_2) \cdot E_1 - (\nabla \times E_2) \cdot H_1 + (\nabla \times H_1) \cdot E_2.$$

From Maxwell's equations for linear, time invariant systems

$$\nabla \times E_1 = -j\omega\mu \cdot H_1 \tag{A.3}$$

$$\nabla \times H_1 = j\omega\epsilon \cdot E_1 + J_1 \tag{A.4}$$

$$\nabla \times E_2 = -j\omega\mu \cdot H_2 \tag{A.5}$$

$$\nabla \times H_2 = j\omega\epsilon \cdot E_2 + J_2. \tag{A.6}$$

We can substitute the curl terms of Equations A.2-6 into Equation A.2 to yield:

$$\nabla \cdot (E_1 \times H_2 - E_2 \times H_1) = -j\omega H_1 \cdot \mu \cdot H_2 - j\omega E_2 \cdot \epsilon \cdot E_1 - J_2 \cdot E_1 + j\omega\mu H_2 \cdot \mu \cdot H_1 + j\omega E_1 \cdot \epsilon \cdot E_2 + J_1 \cdot E_2 \tag{A.7}$$

Assuming symmetric permittivity and permeability across V, i.e. $\mu = \mu^t$ and $\epsilon = \epsilon^t$such that $H_1 \cdot \mu \cdot H_2 = H_2 \cdot \mu \cdot H_1$ and $E_1 \cdot \epsilon \cdot E_2 = E_2 \cdot \epsilon \cdot E_1$, we can simplify Equation A.7 to:

$$\nabla \cdot (E_1 \times H_2 - E_2 \times H_1) = J_1 \cdot E_2 - J_2 \cdot E_1 . \tag{A.8}$$

Integrating Equation A.8 over V results in:

$$\iiint \nabla \cdot (E_1 \times H_2 - E_2 \times H_1)\, dV = \iiint (J_1 \cdot E_2 - J_2 \cdot E_1)\, dV , \tag{A.9}$$

and applying Gauss's divergence theorem yields:

$$\oiint (E_1 \times H_2 - E_2 \times H_1)\, ds = \iiint (J_1 \cdot E_2 - J_2 \cdot E_1)\, dV . \tag{A.10}$$

We will now recall that in the far field, E and H become spherical waves related by $H = (\hat{n} \times E)/\eta$, where $\hat{n}$ is the radial direction away from the source, and η is the impedance of free space. Thus, the left-hand side of Equation A.10 can be seen to be 0 as $S \to \infty$,

$$(E_1 \times H_2 - E_2 \times H_1) \cdot \hat{n} dS = (\hat{n} \times E_1) \cdot H_2 - (\hat{n} \times E_2) \cdot H_1 = \eta H_1 \cdot H_2 - \eta H_2 \cdot H_1 = 0. \tag{A.11}$$

We can now rearrange the right-hand side of Equation A.10 to realize the form of the reciprocity theorem often used for the analysis of antennas. This is the most usual starting point in the literature:

$$\iiint J_1 \cdot E_2 \, dV = \iiint J_2 \cdot E_1 \, dV \, . \tag{A.12}$$

If we assume that the source is a point-like dipole, i.e. $J_i = -j\omega p_i \delta(r - r_i)$, where p_i is the dipole moment, then Equation A.12 reduces to

$$p_1 * E_2(r_1) = p_2 * E_1(r_2), \tag{A.13}$$

as seen in Chapter 2. This result is based on the following assumptions: the system is linear and time invariant, the system has symmetric permittivity and permeability tensors, and that the sources are dipoles in each other's far field.

Equation A.13 is the basis of the reciprocal simulations in this work and means that the electric field at the metasurface, r_1, due to a dipole in the far field, r_2, is proportional to the electric field in the far field due to a dipole in the metasurface. In a hope that this concept is firmly understood, we will reword this to better capture the functionality of the intended application: a plane wave from the far field will excite an electric field in the metasurface proportional to the electric field that a dipole in the metasurface *would have* excited in the far field. Thus, we do not need to simulate dipoles in the metasurface and project their emission to the far field. We can instead simulate a series of plane waves from the far field and measure their effect in the metasurface.

A.2 Simulating Luminescent Metasurfaces

We will now describe in detail how reciprocity is used in simulating emission. Most details regarding the application of reciprocity emission simulation are available in the Supporting Information sections of Chapters 3 and 4. We will not repeat that information. Rather, we will discuss decisions to consider in using the build and analysis scripts.

It is worth noting that the vast majority of the simulations performed in this work are single wavelength. This was a deliberate choice made in the interest of computational efficiency. Lumerical FDTD can support simulation of a broadband angled source, supposing Bloch boundary conditions are used, but doing so requires more computation time, creates more data, and usually does not provide notable benefit. Benefit may have been realized during the simulation of electroluminescent metasurfaces[97], but it was decided to preserve the existing scripts at the cost of more simulation files.

Mesh override region and frequency domain power monitor placement determines the position of the 'hypothetical QWs'. No simulation structure has ever been instituted to try to capture the optical properties of these ultra-thin layers. Such layers, especially in the limit of a single layer as described in Chapter 4, are assumed to have a negligible effect on wave propagation. This assumption is based the fact that the thickness of the QWs is much, much smaller than the wavelength of light, $\frac{t_{Qw}}{\lambda_0} \approx 0.01$. The assumption is validated by the various comparisons between simulation and experiment in Chapters 3 and 4. Care should be taken in placing the mesh and power monitor to minimize file size while maximizing learning potential. It is generally true that maximum directivity occurs near the top of the pillars. The mesh spacing in the vertical direction (e.g. dy) determines query point of hypothetical QWs. Growth tolerances usually limit useful values of dy to about 10 nm, i.e. QWs cannot be placed with finer precision than ~10 nm.

The last critical choice in building emission simulations is the choice of the plane wave source angles. It is obviously important to span the measurable momentum space of the experimental setup, i.e. $\pm 1.3\ k_0$, but the choice of sampling density has less clear guidelines. Many early simulations were done with a 70-point linear sampling across momentum space

(as opposed to angle space, where $k_{||} = n * \sin(\theta)$). Such momentum sampling density provided a good balance between simulation number and critical feature identification. Obviously, low sampling density runs the risk of missing relatively sharp features in momentum space. Occasionally, an 'outlier' result appeared in the emission profile, i.e. a single-data-point-wide peak at an unexpected momentum. When investigated, such features were usually found to be the result of a simulation that did not converge/complete. Conversely, there are many situations that we should expect sharp momentum features, e.g. if the design is likely to cause Fabry-Perot oscillations, as was the case for electroluminescent simulations where there was a ~4 micron n-GaN layer below the metaelements[97]. There is no universal choice and sampling density will have to be chosen on a case-by-case basis. For instance, the optimizations in Chapter 4 used a nonlinear sampling with increased density increasing near the intended emission momentum. This allowed for resolving very sharp momentum features (highly directive emission) without needing to spend computational time simulating uninteresting regions of momentum space.

Further data savings (~50%) can be made by extracting the relevant data from the completed .fsp files and saving it as .mat files. In extracting the data, it is important to preserve metaelement position information in order to set the integration bounds – emission cannot occur outside of the metaelement. Two methods were developed to this end. The first, and more storage-efficient, was developed for rectangular pillars and stores a list of the minimum and maximum extent of each pillar[96]. The second, which was necessary for the tapered structures encountered electroluminescent devices, was to store the material index at all grid locations[97]. This choice affects the analysis algorithm. That said, there is no difference between them for a right-angled pillar.

While considering integration bounds, it is reasonable to assume that the emitting layer will be damaged during etching, decreasing photoluminescence efficiency near the etched regions. Such an effect could be realized with the following mechanism, though others are possible. Etching creates dangling bonds. These dangling bonds generate surface states which allow increased nonradiative recombination[147–151]. Some experiments (photoluminescence vs. pump intensity) seem to support this mechanism, but the evidence is not conclusive. Opposing the proposed mechanism is the fact that etching GaN microstructures into a thin film reduces strain in the QW. This results in both a blue shift of the spectrum and (usually) brighter emission[152–157]. A strained GaN QW thin film will experience the quantum confined stark effect – a bending of the conduction and valence bands which lowers electron-hole overlap[54]. Reducing the strain improves overlap and increases the effective bandgap. Thus, we have competing mechanisms. To the best of our knowledge, there have been no studies on nanoscale location-resolved luminescence in GaN after etching. Perhaps cathodoluminescence could be used to explore this question. Nonetheless, simulations match experimental data more closely when we treat the outer ~10-20 nm of the nanoelements as non-emissive, that is, we exclude those regions of the metaelements from the integration, see Chapter 3.5.

Directivity was calculated in substrate-angle space (as opposed to momentum space or angle in air), see Chapter 4. This decision was made to balance the conventional definition of directivity with experimental realities. Directivity is usually calculated as angle in air over the full 4π steradians. Our experimental setup can only measure one hemisphere, but it is capable of measuring evanescent modes or supercritical rays, $|k_0| > 1$. In fact, Chapters 3 and 4 were motivated by the large supercritical emission for s-polarized light seen in Iyer et

al[54]. A metric which excluded supercritical rays (which have imaginary angle in air) would have missed critical information. Thus, directivity was calculated as a function of angle in substrate.

Appendix B: Efficient Global Optimization (EGO)

Chapter 2 provided a brief synopsis of the strengths of the EGO algorithm along with an overview of the algorithm flow. This section seeks to explore more practical aspects, especially how to apply the algorithm in code and use the outputs to optimize a system. It is worth noting that open source implementations of Bayesian Optimization algorithms exist in the form of BoTorch and Ax (Adaptive Experimentation Platform).

B.1 General Considerations

The codes developed in this work for optimization of unidirectional emission and optimization of polarization-insensitive retroreflection are based on the work of Jones, et al.[55] where they lay out an algorithm to fit a model to data of arbitrary dimension (though as a rule of thumb, dimensionality should be kept below ~20) such that we can deduce input-output relationships, estimate maxima, and suggest additional evaluation points. It also establishes a model validation metric and a branch-and-bound algorithm for selecting search points. The former has been implemented in the scripts, whereas the latter was not. The reason for leaving branch-and-bound out of the scripts are explained in the comments of the example EGO code (see Appendix D), but in short, branch-and-bound would have attempted to find a 'true optimum', irrespective of fabrication tolerances. As such, parameter space was constructed with fabrication tolerances in mind and expected improvement was calculated for all candidate points in the space. This method avoided chasing after unachievable optima created by un-fabricable changes e.g. shifting a metaelement 0.5 nm.

It is worth mentioning that when generating training data, care should be taken that training data spans parameter space. A Latin hypercube is notable in this regard in that it

equally samples and fills parameter space. Unfortunately, a simple Latin hypercube is unsatisfactory as many parameters in these optimizations are dependent on other parameters, i.e. the second metaelement cannot be in the same location as the first, thus efforts were made to implement a constrained Latin hypercube[158] for training data generation, but all such efforts ended with training points that left large portions of parameter space unsampled. Thus, random points of physically relevant parameter space were chosen for the training sets in this work. It is possible that better implementation of a constrained Latin hypercube may result in better training data.

B.2 Foundational Equations of EGO

We will now explore the foundational equations and metrics of the EGO algorithm. Assume that we have sampled n points of a k dimensional function, denote sampled point i by $\boldsymbol{x}^{(i)} = \left(x_1^{(i)}, \ldots, x_k^{(i)}\right)$ where $1 \leq i \leq n$. In other words, we have simulated n combinations of k dimensional parameter space where e.g., $x_1^{(3)}$ represents the width of a metaelement (the first dimension) in the third simulation, and $x_2^{(5)}$ represents the position of a metaelement (the second dimension) in the fifth simulation. Such sampled data, $\mathrm{y}\left(\boldsymbol{x}^{(i)}\right)$, the figure of merit of these simulation, can be modeled by:

$$\mathrm{y}\left(\boldsymbol{x}^{(i)}\right) = \epsilon\left(\boldsymbol{x}^{(i)}\right) + \mu, \tag{B.1}$$

where μ is the average of the model, and $\epsilon\left(\boldsymbol{x}^{(i)}\right)$ is what Jones, et al. call the 'error' as a function of $\boldsymbol{x}^{(i)}$. This 'error' function is a stochastic process, or a set of correlated random variables. That said, no analytic expression is given for $\epsilon\left(\boldsymbol{x}^{(i)}\right)$. Constructing an approximation of $\epsilon\left(\boldsymbol{x}^{(i)}\right)$ is the purpose of this optimization.

We can, however, describe the correlation of errors, $\mathrm{Corr}\left[\epsilon\left(\boldsymbol{x}^{(i)}\right), \epsilon\left(\boldsymbol{x}^{(j)}\right)\right]$. We start by introducing the correlation matrix, $\boldsymbol{R}$, a symmetric $n \times n$ matrix whose (i, j) entry is $\mathrm{Corr}\left[\epsilon\left(\boldsymbol{x}^{(i)}\right), \epsilon\left(\boldsymbol{x}^{(j)}\right)\right]$:

$$\boldsymbol{R} = \begin{bmatrix} \mathrm{Corr}\left[\epsilon\left(\boldsymbol{x}^{(1)}\right), \epsilon\left(\boldsymbol{x}^{(1)}\right)\right] & \cdots & \mathrm{Corr}\left[\epsilon\left(\boldsymbol{x}^{(1)}\right), \epsilon\left(\boldsymbol{x}^{(n)}\right)\right] \\ \vdots & \ddots & \vdots \\ \mathrm{Corr}\left[\epsilon\left(\boldsymbol{x}^{(n)}\right), \epsilon\left(\boldsymbol{x}^{(1)}\right)\right] & \cdots & \mathrm{Corr}\left[\epsilon\left(\boldsymbol{x}^{(n)}\right), \epsilon\left(\boldsymbol{x}^{(n)}\right)\right] \end{bmatrix}, \tag{B.2}$$

where

$$\mathrm{Corr}\left[\epsilon\left(\boldsymbol{x}^{(i)}\right), \epsilon\left(\boldsymbol{x}^{(j)}\right)\right] = \exp\left[-d\left(\boldsymbol{x}^{(i)}, \boldsymbol{x}^{(j)}\right)\right], \tag{B.3}$$

and

$$d\left(\boldsymbol{x}^{(i)}, \boldsymbol{x}^{(j)}\right) = \sum_{h=1}^{k} \theta_h |x_h^{(i)} - x_h^{(j)}|^{p_h}, \tag{B.4}$$

where θ_h and p_h are fitting terms and $\theta_h > 0$.

Inspection of Equation B.3 shows that the correlation of the errors is inversely related to distance, $d\left(\boldsymbol{x}^{(i)}, \boldsymbol{x}^{(j)}\right)$. In the case where $\theta_h = 1$ and $p_h = 2$, Equation B.4 says that the distance between any two sampled points i and j is the sum of the square of the difference in each of their dimensions, i.e. their Euclidean distance. If we consider the case that $\boldsymbol{x}^{(1)}$ and $\boldsymbol{x}^{(2)}$ are 'close', i.e. that the first and second sampled point have similar values for all dimensions, then Equations B.3-4 indicate the errors should be highly correlated and Equation B.1 indicates that $\mathrm{y}\left(\boldsymbol{x}^{(1)}\right)$ and $\mathrm{y}\left(\boldsymbol{x}^{(2)}\right)$ are similar, as we intuitively expect.

θ_h is one of the most important variables to keep in mind during optimization. Functionally, θ_h describes how sensitive the model is to different dimensions, with larger values of θ_h indicating the system has a greater sensitivity to the h^{th} dimension. This is the foundation of the interpretability mentioned in Chapter 2 and exploited in Chapter 5. Assume that $\theta_1 = 5$ and $\theta_2 = 0.1$, and the first dimension corresponds to the width of a metaelement,

and the second dimension represents the position of a metaelement. In this case, we can relax the fabrication tolerances on the position of the metaelement, but not on the metaelement width which is predicted to be very important. As an additional note, larger values of p_h indicate smoother variation in the correlation. Although p_h can have any value for each dimension, Jones, et al. find success even when they fixed the value to 1 or 2 for all dimensions. All optimizations in this work found best performance for $p = 1$. It is possible that quicker optimization convergence or more accurate models could be achieved by allowing p_h to vary across all dimensions, but this would come at the cost of potential model instabilities due to overfitting. That said, the remainder of this analysis will assume that $p = 1$.

As presented in Equations B.3-4 and used in this work, $\mathrm{Corr}\left[\epsilon\left(\boldsymbol{x}^{(i)}\right), \epsilon\left(\boldsymbol{x}^{(j)}\right)\right]$ is a gaussian-like expression. This is generally useful as we expect dissimilar metasurfaces to respond differently. That is, we do not expect the measured value to have long range order in parameter space. One could, however, imagine a case where the measured value should be, e.g. periodic across parameter space. In this case, $\mathrm{Corr}\left[\epsilon\left(\boldsymbol{x}^{(i)}\right), \epsilon\left(\boldsymbol{x}^{(j)}\right)\right]$ should be represented by a sinusoidal expression instead.

So far, we have k fitting terms for k dimensions. Traditional Bayesian optimization of noiseless systems includes two additional 'fitting terms': μ and σ^2, the mean and uncertainty of our model, respectively. Fortunately, Jones et al. provides analytic solutions to these assuming a good fit between model and data:

$$\mu = \frac{\mathbf{1}'\boldsymbol{R}^{-1}\mathrm{y}(\boldsymbol{x})}{\mathbf{1}'\boldsymbol{R}^{-1}\mathbf{1}} \tag{B.5}$$

where $\mathbf{1}$ is an $n \times 1$ vector of ones, and $\mathbf{1}'$ is the transpose of $\mathbf{1}$ (a $1 \times n$ vector of ones), $\boldsymbol{R}^{-1}$ is the inverse of $\boldsymbol{R}$ (Equation B.2), and $\mathrm{y}(\boldsymbol{x})$ is an $n \times 1$ vector of the values of sampled data (Equation B.1). The uncertainty is:

$$\sigma^2 = \frac{[y(\boldsymbol{x}) - \mathbf{1}\mu]'\boldsymbol{R}^{-1}[y(\boldsymbol{x}) - \mathbf{1}\mu]}{n}. \tag{B.6}$$

where μ and σ^2 are each scalar values of known magnitude so they will not be considered fitting parameters in the remainder of this analysis. This leaves k fitting parameters: one for each of the scalar correlation terms, θ_h. We now have the question: what are the values of θ_h and how do we find them?

Jones, et al. does not address this directly, instead saying that the best value of θ_h maximizes a likelihood function, $\mathcal{L}\big(\theta, \boldsymbol{x}, \mathrm{y}(\boldsymbol{x})\big)$, (see Equation B.7-8). It revealed in their acknowledgement section that they used a different optimization algorithm to find the fitting terms, which presents a chicken and egg problem. The optimization algorithm needs an optimization algorithm. This is frustrating, but not insurmountable. Although we do not know the behavior of the likelihood function with respect to θ_h, i.e. is it differentiable, is it convex, etc., we have been able to find good values of θ_h using a modified multi-start 'gradient ascent' algorithm.

Owing to the highly variable size of $\mathcal{L}$ (over 100 orders of magnitude across various design systems and over 20 orders of magnitude during any given search for optimal θ_h), true gradient ascent was found to be unstable, often resulting in negative values of θ_h. The issue is thought to be related to the relative scale of $\mathcal{L}$ and θ_h. It proved difficult to determine a good choice of step size, γ, because $\mathcal{L}$ is so highly variable while θ_h is usually on the order of 1. We observed that large changes in θ_h (e.g. a factor of 2 in a single step) often resulted in reduction of $\mathcal{L}$ and the termination of the fitting parameter optimization. Thus, the algorithm

does not use a true gradient, rather taking steps of a fixed fraction of θ_h along the ascending direction. That is, if $\theta = 1$ during search step 1, then $\mathcal{L}(1, \boldsymbol{x}, \mathrm{y}(\boldsymbol{x}))$ and $\mathcal{L}(1.02, \boldsymbol{x}, \mathrm{y}(\boldsymbol{x}))$ will be calculated and depending on the relative values of $\mathcal{L}$, θ will be set to either $0.98, 1,$ or 1.02 for search step 2. This avoids the aforementioned instability at the cost of convergence speed. It is likely that efficiency gains can be made by revising this algorithm, see open source codes, but the current algorithm runs in less than a minute.

We now will introduce the likelihood function:

$$\mathcal{L}\big(\theta, \boldsymbol{x}, \mathrm{y}(\boldsymbol{x})\big) = \frac{1}{(2\pi)^{n/2}(\sigma^2)^{n/2}|\boldsymbol{R}|^{1/2}} \exp\left[-\frac{[y(\boldsymbol{x}) - \mathbf{1}\mu]'\boldsymbol{R}^{-\mathbf{1}}[y(\boldsymbol{x}) - \mathbf{1}\mu]}{2\sigma^2}\right] \tag{B.7}$$

where $|\boldsymbol{R}|$ is the determinant of $\boldsymbol{R}$. Using Equation B.6, this can be simplified and rearranged to

$$\mathcal{L}\big(\theta, \boldsymbol{x}, \mathrm{y}(\boldsymbol{x})\big) = \frac{1}{\sqrt{(2\pi\sigma^2 e)^n |\boldsymbol{R}|}}. \tag{B.8}$$

The above discussion and Equation B.8 indicate that good values for θ_h minimize the determinate of the correlation matrix and model uncertainty. Assuming that the multi-start 'gradient ascent' algorithm found good values of θ_h, i.e. the model fits the data, we can now make predictions for the values of unsampled points, $y(\boldsymbol{x}^+)$, where $\boldsymbol{x}^+$ represents m combinations of k dimensional parameter space.

The notation in the next section is similar to, but critically different from the notation introduced in Equation B.1-8. To avoid confusion, we will restate their meanings: $\boldsymbol{x}^{(i)}$ is the i^{th} of n sampled points for which we have a measured figure of merit, $y(\boldsymbol{x}^{(i)})$. $\boldsymbol{x}^{+(i)}$ is the i^{th} of m points for which we will predict the figure of merit, $y(\boldsymbol{x}^{+(i)})$. $\boldsymbol{x}$ and $\boldsymbol{x}^+$ are $n \times k$ and $m \times k$ matrixes, respectively, of points in k dimensional parameter space. It is important to note that Jones et al. only considers predicting the value of a single point, i.e. $m = 1$ because

of their use of the branch-and-bound algorithm. We have generalized the algorithm for any integer value of m. Thus, there will be changes in notation between Jones et al. and this analysis.

In order to make predictions of $y(\boldsymbol{x}^+)$, we must first introduce an analogue of Equation B.2, accounting for the correlation of errors between $\boldsymbol{x}$ and $\boldsymbol{x}^+$:

$$\boldsymbol{r} = \begin{bmatrix} \mathrm{Corr}\left[\epsilon\left(\boldsymbol{x}^{(1)}\right), \epsilon\left(\boldsymbol{x}^{+(1)}\right)\right] & \cdots & \mathrm{Corr}\left[\epsilon\left(\boldsymbol{x}^{(1)}\right), \epsilon\left(\boldsymbol{x}^{+(m)}\right)\right] \\ \vdots & \ddots & \vdots \\ \mathrm{Corr}\left[\epsilon\left(\boldsymbol{x}^{(n)}\right), \epsilon\left(\boldsymbol{x}^{+(1)}\right)\right] & \cdots & \mathrm{Corr}\left[\epsilon\left(\boldsymbol{x}^{(n)}\right), \epsilon\left(\boldsymbol{x}^{+(m)}\right)\right] \end{bmatrix} \tag{B.9}$$

which is an $n \times m$ matrix where the (i, j) entry is analogous to Equation B.3:

$$\mathrm{Corr}\left[\epsilon\left(\boldsymbol{x}^{(i)}\right), \epsilon\left(\boldsymbol{x}^{+(j)}\right)\right] = \exp\left[-d\left(\boldsymbol{x}^{(i)}, \boldsymbol{x}^{+(j)}\right)\right], \tag{B.10}$$

which is analogous to Equation B.4:

$$d\left(\boldsymbol{x}^{(i)}, \boldsymbol{x}^{+(j)}\right) = \sum_{h=1}^{k} \theta_h \left| x_h^{(i)} - x_h^{+(j)} \right|. \tag{B.11}$$

Keeping in mind that we have already found values for θ_h and set $p_h = 1$, we can now predict the m elements of $y(\boldsymbol{x}^+)$ as

$$y(\boldsymbol{x}^+) = \mu + \boldsymbol{r}'\boldsymbol{R}^{-1}[y(\boldsymbol{x}) - \mathbf{1}\mu] \tag{B.12}$$

where μ is the same as was found during fitting parameter optimization using Equation B.5 and $\mathbf{1}$ is still an $n \times 1$ vector of ones. We can also estimate the uncertainty of this prediction, $s^2(\boldsymbol{x}^+)$:

$$s^2(\boldsymbol{x}^+) = \sigma^2 \left[1 - \boldsymbol{r}'\boldsymbol{R}^{-1}\boldsymbol{r} + \frac{(1 - \mathbf{1}'\boldsymbol{R}^{-1}\boldsymbol{r})^{\mathbf{2}}}{\mathbf{1}'\boldsymbol{R}^{-1}\mathbf{1}}\right], \tag{B.13}$$

where σ^2 is the same as was found during fitting parameter optimization using Equation B.6. As currently formulated, s^2 is an $m \times m$ matrix. The uncertainty corresponding to $y\left(\boldsymbol{x}^{+(i)}\right)$, is found along the diagonal (or trace) of $s^2(\boldsymbol{x}^+)$ at entry (i, i).

As a sanity check of Equation B.12, we will set $\boldsymbol{x}^+ = \boldsymbol{x}$. Here, we are asking the question: 'what does the algorithm predict when it already 'knows' the answers?'. Inspection of Equation B.9 given $\boldsymbol{x}^+ = \boldsymbol{x}$ shows that $\boldsymbol{r} = \boldsymbol{R}$. Thus, Equation B.12 reduces to

$$y(\boldsymbol{x}^+ = \boldsymbol{x}) = \mu + \boldsymbol{I}[y(\boldsymbol{x}) - \mathbf{1}_m\mu] = \mu + y(\boldsymbol{x}) - \mu = y(\boldsymbol{x})$$

As we should expect. Keeping in mind that the diagonal entries of $\boldsymbol{R}$ and $\boldsymbol{r}$ are 1, we use the same sanity check on Equation B.13 to reveal that,

$$s^2(\boldsymbol{x}^+ = \boldsymbol{x}) = \sigma^2\left[1 - \boldsymbol{r}'\boldsymbol{I} + \frac{(1 - \mathbf{1}'\boldsymbol{I})^2}{\mathbf{1}'\boldsymbol{R}^{-1}\mathbf{1}}\right] = \sigma^2\left[1 - \mathbf{1} + \frac{(0)^2}{\mathbf{1}'\boldsymbol{R}^{-1}\mathbf{1}}\right] = \mathbf{0}$$

as we should expect. Thus, when predicting values for the points that we have already sampled, we recover the sampled values with no uncertainty.

Knowledge of $y(\boldsymbol{x}^+)$ is insufficient for optimization. In most systems, the coordinates of the maximum predicted value will be the same as the coordinates of the maximum measured value, i.e. the model usually does not predict better values than it starts with. We could sort $y(\boldsymbol{x}^+)$ and measure/simulate the highest unmeasured point, but such a search would never explore parameter space – high scoring points are likely to be near the maximum scoring point. We need a metric that will balance exploitation and exploration. Jones et al. provide a variant of the following expression, terming it the expected improvement of the prediction, $EI(\boldsymbol{x}^+)$:

$$EI(\boldsymbol{x}^+) = \big(y(\boldsymbol{x}^+) - y_{max}(\boldsymbol{x})\big)\Phi\left(\frac{y(\boldsymbol{x}^+) - y_{max}(\boldsymbol{x})}{s(\boldsymbol{x}^+)}\right) + Zs(\boldsymbol{x}^+)\phi\left(\frac{y(\boldsymbol{x}^+) - y_{max}(\boldsymbol{x})}{s(\boldsymbol{x}^+)}\right) \tag{B.14}$$

where $y_{max}(\boldsymbol{x})$ is the maximum value of sampled data, $\Phi(\cdot)$ is a cumulative distribution function (also known as a standard normal density function), $s(\boldsymbol{x}^+)$ is the square root of $s^2(\boldsymbol{x}^+)$, Z is a scaling factor, and $\phi(\cdot)$ is a probability density function (also known as a

distribution function). We can intuitively understand Equation B.14 as balancing exploration vs. exploitation. The first term tries to quantify how much better any $\boldsymbol{x}^{+(i)}$ will be than the current best whereas the second term tries to factor in the uncertainty of that prediction (and the scaling factor can be changed to prioritize exploration or exploitation). A point with a low expected value (far from the maximum measured point) can still have a large expected improvement if the uncertainty near that point is large (the model has not sampled that region). Conversely, if we use the sanity check again, we find that $EI(\boldsymbol{x}^+ = \boldsymbol{x}) = \mathbf{0}$. Thus, EI automatically filters out previously measured points/simulated structures.

The combination of parameters with maximum EI is chosen to measure/simulate next. However, given practical concerns, we often choose to simulate a distribution of points with large $EI(\boldsymbol{x}^+)$. This is computationally wasteful but is more efficient from a man-hour perspective. The distribution of sampled points is generated by mapping a cumulative distribution function onto the sorted list of points with EI above some threshold, e.g. $EI(\boldsymbol{x}^+) > y_{max}(\boldsymbol{x})/1000$. This samples more points with high expected improvement and fewer points with lower expected improvement. After simulating/measuring these proposed points, they are added to the data set and the model is retrained and more predictions are made until the maximum of $EI(\boldsymbol{x}^+)$ falls below some threshold, e.g. $y_{max}(\boldsymbol{x})/100$.

B.3 Toy Optimization Problem

Consider a toy system where the objective function (usually unknown) is a 1-dimensional sum of gaussian functions, as seen in Figure B.1a (solid blue line), and we have sampled it as shown by the blue dots, $y(\boldsymbol{x})$. Here we will use EGO to find the maximum of this function using the following steps: (1) train the model (find good values for θ_h), (2) use

that model to predict new values and their expected improvement, $y(\boldsymbol{x}^+)$ and $EI(\boldsymbol{x}^+)$, (3) add those points to $y(\boldsymbol{x})$, and (4) repeat (2-3) until convergence.

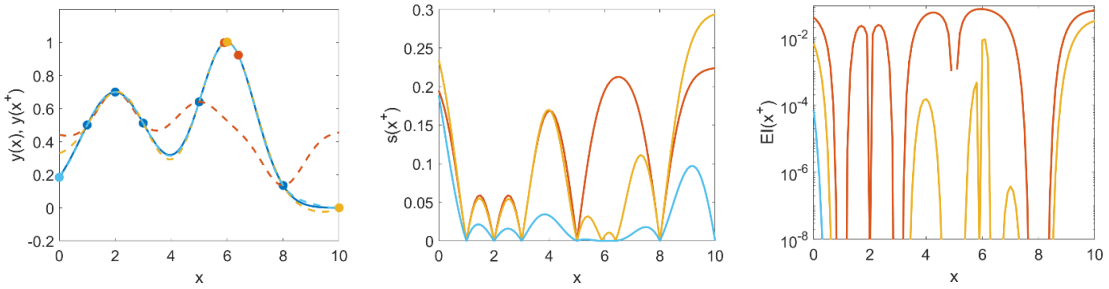

(a) (b) (c)

Figure B.1: Plots showing (a) the objective function (solid blue), sampled points (dots), and predicted values (dashed lines) for 3 training-prediction cycles (red, yellow, sky blue). (b, c) Uncertainty and expected improvement, respectively, for those same 3 cycles. We see that the algorithm balances exploration and exploitation.

We can see that the first training-prediction cycle yields a prediction (red dashed line, Figure B.1a) that crosses through all 5 training points. Having very few sampled points, EGO is generally predicting values for all points around the expected mean, $\mu \approx 0.5$. In truth, there is little to be gained by comparing the objective function against the model, as in general, we do not know the objective function. That said, we can see that the model captures the first gaussian and predicts maximum values around $x = 2$. Looking at Figure B.1b (red line), we see that these predictions have large uncertainty near $x = 4, 6, \text{and } 10$ with very little uncertainty near $x = 2$. This is a direct result of the model having very little information near $x = 4, 6, \text{and } 10$. Looking now at the expected improvement in Figure B.1c, which is on a log scale, we see that the first cycle (red) show a maximum near $x = 6$. This is despite the fact that the predicted value was relatively small there (Figure B.1a, red dashed line near $x = 2$ shows the maximum). This demonstrates the algorithm exploring instead of exploiting and is the end of cycle 1.

We calculate values for (simulate/measure) the parameters corresponding to the maximum expected improvement and add those measurements to $y(\boldsymbol{x})$. They show up in Figure B.1a as red dots. We can now repeat the cycle, yielding predicted values corresponding to yellow lines. We see that the predictions (yellow dashed line) now expect a maximum near $x = 6$ and a minimum near $x = 10$. Nonetheless, maximum uncertainty (Figure B.1b, yellow line) occurs near $x = 10$ and this causes maximum expected improvement (Figure B.1c, yellow line) to occur near $x = 10$. Another maximum expected improvement occurs near $x = 6$. The algorithm recommends those 2 points to measure. This shows a balance between exploration and exploitation.

We calculate those values and add them to $y(\boldsymbol{x})$. They show up in Figure B.1a as yellow dots. We repeat the cycle and predict values for all points in parameter space yielding predictions (sky blue line) that show a maxima near $x = 6$, and large uncertainty (sky blue line) near $x = 0,\ 9$. That said, the predicted value of $x = 6$ is greater than the predited value of $x = 9$, so the expected improvement of $x = 0$ is larger than for $x = 9$. Thus, $x = 0$ is recommended. Looking back at Figure B.1a, we see that the predictions after the third cycle (sky blue dotted line) match the objective function. Thus, our model which only knows 9 points has accurately fit a system with 6 degrees of freedom. This demonstrates the power of the EGO algorithm.

B.4 Model Validation

The last aspect to consider is model validation. This is critical, given that we will never know the objective function in practice (else we could find the maximum using a first derivative or similar). Model validation asks the question: ‘are the values of θ_h good?’. It

works by removing the i^{th} entry of $\mathrm{y}(\boldsymbol{x})$ and, given the other $n-1$ entries, predicting the value and uncertainty of the i^{th} entry, $\mathrm{y}\left(\boldsymbol{x}^{+(i)}\right)$ and $\mathrm{s}\left(\boldsymbol{x}^{+(i)}\right)$. We can then compare $\mathrm{y}\left(\boldsymbol{x}^{+(i)}\right)$ to $\mathrm{y}\left(\boldsymbol{x}^{(i)}\right)$ and verify that

$$-3 \leq \frac{y\left(\boldsymbol{x}^{(i)}\right) - y\left(\boldsymbol{x}^{+(i)}\right)}{\mathrm{s}\left(\boldsymbol{x}^{+(i)}\right)} \leq 3 \tag{B.15}$$

that is, that the prediction does not deviate from the measured value by more than 3 standard deviations. In the ideal case, $y\left(\boldsymbol{x}^{(i)}\right) = y\left(\boldsymbol{x}^{+(i)}\right)$, but the model does not know the value of the point that we removed and must guess. Importantly, $\mathrm{s}\left(\boldsymbol{x}^{+(i)}\right) \neq 0$ because $\boldsymbol{x}^{+(i)}$ is not an element of $\boldsymbol{x}^{(i)}$. Figure B.2 shows model validation for a real system based on retroreflectors during the first cycle (top) and during the last cycle (bottom). Two visualization methods are included, though they have nominally identical information. The plots on the left show a direct representation of Equation B.15 whereas the plots on the right show a more intuitive representation of predicted values vs measured values with error bars representing $3 * \mathrm{s}\left(\boldsymbol{x}^{+(i)}\right)$. A yellow line is included to guide the eye to $\mathrm{y}\left(\boldsymbol{x}^{+(i)}\right) = \mathrm{y}\left(\boldsymbol{x}^{(i)}\right)$.

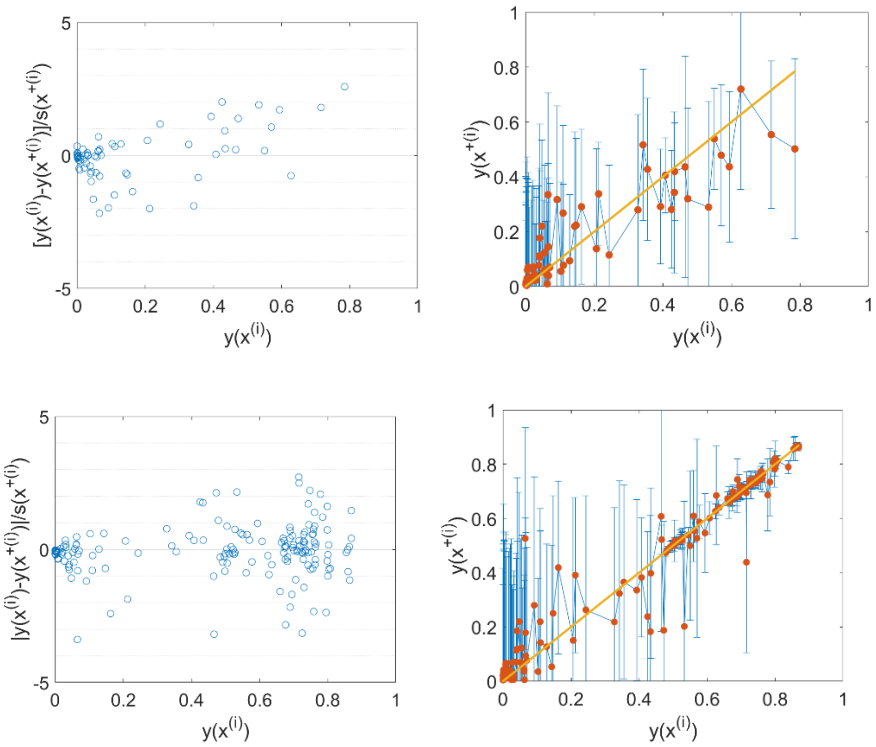

Figure B.2: Visualizations of model validation (top) during the first training-prediction cycle and (bottom) during the last training-prediction cycle. The same information is conveyed between (left) and (right). Both are included here, and the user can choose which to use as a matter of preference. Over the course of the optimization, we see that the model discovers better designs and becomes more certain of high performing designs.

We will focus our analysis of the optimization from the perspective of the right-hand plots, as a matter of preference. During the first training set (top), we see that the model underestimates (overestimates) high (low) performing designs. This is typical and is a result of the model predicting values around the expected mean. We also see that the uncertainties are quite large across the board. These uncertainties are typical of all optimizations we have seen in this work – parameter space is enormous, and the model is only ever trained on ~100 points. We should not expect results like in the toy system.

As the optimization nears its end, EGO has discovered new, better, designs (Figure B.2, bottom right) and we see that it has exploited (thoroughly sampled) those regions of

parameter space such that the uncertainty near these points drops significantly. Naturally, the model is also doing a better job of predicting these values. The fixation on the high performing designs comes at the cost of less certain modeling the low performing designs, as demonstrated by increasing uncertainty in that region. In fact, in some optimizations, the model will 'forget' about the low performing designs and predict them to be exactly the mean value.

At all points in the optimization, the model was validated because the predictions fell within three standard deviations of the measured value. In the cases where the model does not validate, it is most likely that the values of θ_h are incorrect. In this case, change the scale of the initial values of θ by, for example, multiplying the starting values by 10. It is also possible to transform the inputs by, for example, setting the transformed inputs equal to the log or negative reciprocal of inputs, i.e. $\mathrm{y}'(\boldsymbol{x}) = -\frac{1}{\mathrm{y}(\boldsymbol{x})}$, $\mathrm{y}'(\boldsymbol{x}) = \log_{10}(\mathrm{y}(\boldsymbol{x}))$.

Appendix C: Optimization of Multiple Outputs: Choice of Figure of Merit

We will also briefly comment on the figure of merit used to simultaneously optimize p- and s-polarized unidirectional emission from GaN QW metasurfaces. EGO, as implemented in this work, accepts one value for each combination of parameters, see Equation B.1. Attempting to optimize directivity of both polarizations is therefore impossible using EGO. Rather, we must construct a figure of merit that tries to capture and quantify the idea of 'directive emission of both polarizations. The figure of merit used in Chapter 4 was:

$$\max\left(\frac{D_{p,\theta_t}(y)}{D_{p,max}}+\frac{D_{s,\theta_t}(y)}{D_{s,max}}\right), \tag{C.1a}$$

where D_{i,θ_t} is the directivity at the target angle for the specified polarization and $D_{i,max}$ is the maximum directivity found during an optimization of only that polarization. Although this figure of merit was sufficient for that application (the directivity of both polarizations grew simultaneously), later work on electroluminescent devices found the optimization excessively prioritized p-polarized emission at the expense of attempting to improve s-. This section explains why that optimization initially failed and how it was overcome.

If we simplify Equation C.1a to its critical features, we can rewrite it as:

$$F = D_p + D_s, \tag{C.1b}$$

which we have plotted in Figure C.1a. The gradient of Equation C.1b is a constant value over all (D_p, D_s), i.e. $\nabla F = \begin{bmatrix}1\\1\end{bmatrix}$. Thus, improving either D_p or D_s, either together or in isolation, will increase the value of F. The EGO algorithm has no knowledge of the formulation, gradient, or intention of F. Rather it simply seeks to increase its value. EGO will do this in

the ‘easiest’ manner possible. If it were the case that there are more combinations of parameters that will improve single polarization directivity than combinations that will improve directive emission of both polarizations, then EGO will recommend a combination from the latter. If there were some error in the simulation or analysis code that caused larger measured values, then EGO would try to exploit that error.

In the case of electroluminescent metasurfaces, it seems that EGO was finding sufficient success exploring/exploiting only the p-directive designs. Although EGO is designed to balance exploration and exploitation, as discussed in Section 2, it can fixate on exploiting a promising region of parameter space, as discussed in Appendix B.4. If other regions of parameter space are underperforming, it will slowly stop attempting to model them in favor of modeling the high performers. The problem of exploitation vs. exploration can be solved given near infinite optimization time (impractical) or it may be addressed by changing the scaling factor, see Equation B.14, to encourage exploration, but such an ad-hoc solution does not address the root cause of the problem in this case. The problem was that EGO was improving exclusively p- directivity. The solution is to change the figure of merit to reward only concurrent improvement.

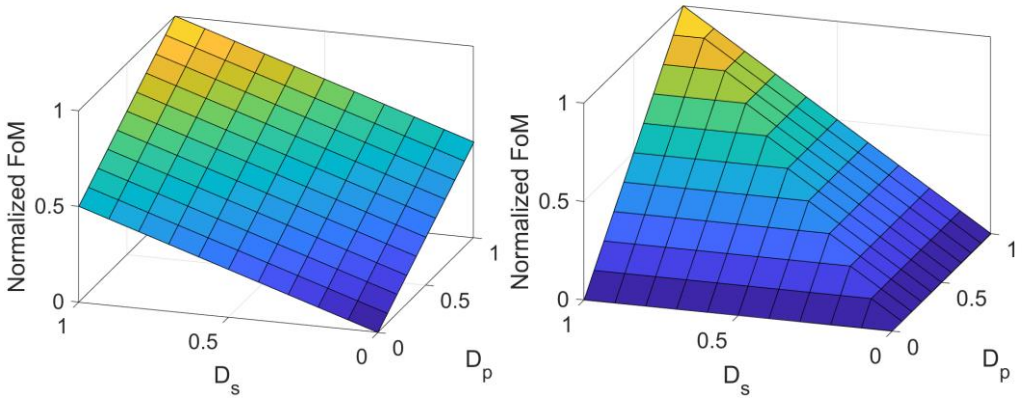

Figure C.1: Normalized figure of merit as described in Equations C.1b (left) and C.2b (right) as a function of normalized polarization specific directivity. Equation C.1

allows for optimization along a single axis, whereas Equation C.2 forces optimization along both axes simultaneously.

An improved figure of merit was developed for 'unpolarized' emission from electroluminescent metasurfaces:

$$\max\left(\frac{D_{p,\theta_t}(y)}{D_{p,max}}+\frac{D_{s,\theta_t}(y)}{D_{s,max}}-\left|\frac{D_{p,\theta_t}(y)}{D_{p,max}}-\frac{D_{s,\theta_t}(y)}{D_{s,max}}\right|\right), \tag{C.2a}$$

or, simplifying it as we did to find Equation C.1b,

$$G=\left(D_p+D_s-\left|D_p-D_s\right|\right). \tag{C.2b}$$

which is plotted in Figure C.1b. We see that like Equation C.1b, Equation C.2b has a maximum at $(D_p=1,D_s=1)$. Thus, in the limit of infinite optimization time and full access to 'figure of merit' space, the choice between C.1a and C.2a is immaterial – optimization on either will tend toward $(D_p=1,D_s=1)$. Of course, we do not have infinite optimization time and we have no reason to expect that we could propose a design that would be measured to have arbitrary combination (D_p,D_s). Admittedly, we do not have a rigorous proof of the latter claim, but we have yet to observe $(1,1)$ despite considerable effort. It is worth noting however, that these limitations: 'finite optimization time' and 'inaccessible regions of figure of merit space', would have the same impact on the usefulness of either figure of merit.

The unique aspect of Equation C.2b is its gradient, which is tri-modal, such that $\nabla G=\begin{bmatrix}1\\1\end{bmatrix}$ when $D_p=D_s$, $\nabla G=\begin{bmatrix}1\\0\end{bmatrix}$ when $D_p<D_s$, and $\nabla G=\begin{bmatrix}0\\1\end{bmatrix}$ when $D_p>D_s$. This change to the figure of merit forces concurrent growth between the two polarizations. Improving p- does not increase the figure of merit if p- is outperforming s- and visa versa, allowing for the same optimization algorithm to converge to a design that displays directional emission of both polarizations.

Again, we stress that the EGO algorithm has no direct access to the expression used for figure of merit, much less a derivative on the figure of merit. Rather, it attempts to approximate the figure of merit as a function of the metasurface parameters. Thus, choice of figure of merit is critical as the construction of the figure encodes the desired end state and optimization path.

Appendix D: Simulation Generation, Analysis, and Optimization Codes

Many distinct scripts were written in trying to understand and optimize various unidirectional emitters. The script that builds and analyzes reciprocal simulations for unidirectional photoluminescence in GaN will be necessarily different from the scripts for electroluminescence. Simulating magnetic dipole emission will necessitate yet a different script. Considering the above, we will only include 'base versions' of the codes here. This section will also provide directories for the various projects that I have worked on.

The simulations generally required 4 types of scripts. The first built the simulations (usually *Build*.lsp), the second extracted the useful information from completed simulations (usually *Output*.lsp), the third script conglomerated and visualized the data (usually *Analysis*.m), and the fourth performs the optimization (usually *EGO*.m) where * represents a wild card character. Example files of each of these have been thoroughly commented and saved as UniEmit_Opt_* in "*Drive*\UCSB\Schuller Lab\Lumerical Data" for future reference.

These example scripts were taken specifically from the project to optimize directivity of p-polarized light from 2 pillar GaN QWs. There are different scripts for the 3-pillar case and matching files for the s- and both-polarized cases. You should not expect to be able to apply the example code outside of its niche. That said, I hope the example scripts can serve as teaching tools and springboards for additional work. Below are tables of projects and associated directories.

Table D1: A list of projects and their associated directories, bolded entries might be of particular interest.

Base File	"*Drive*\UCSB\Schuller Lab\Lumerical Data\MetasurfaceSims\ BeamDeflector\"
3D Nanopillars	Most folders in Base
Theory Paper	Base+ "DataForV3Paper"
Theory Paper Exp. Data	Base+ "ExperimentalData"
HBN emitters	Base+ "Caps"
2D EL Nanorods	Base+ "NanoRods"
2D EL Paper	Base+ "NanoRods\Trapazoid\ELPaper-January2023"
2D MD emitters	Base+ "NanoRods\Perovskite"
2D Phase map multipliers	Base+ "NanoRods\PillarWidthSweep\DoublePhase"
2D Optimization Paper	Base+ "NanoRods\PillarWidthSweep\EGO-cLHS"
Metalenses	Base+"Lenses-NG"
Retroreflectors	Base+"RetroReflector"
Quarter wave plate	Base+"RetroReflector\QWP"

Table D2: A list of projects and their associated directories, bolded entries resulted in publications. These are short term projects, usually collaborations.

Base File	"*Drive*\UCSB\Schuller Lab\Projects"
Chiral Emitters	Base+"BrokenSymmetry-Shaimaa"
Low H-SiN	Base+"Debapam-SiN"
Topotactic phase transition	Base+"LSCO"
InAsSb sensor FTIR	Base+"Raytheon Collab"
Band structure V2O3-CdS	Base+"V2O3-CdS HeteroStrucutre"
Experimental MD emitters	Base+"Projects\Perov on MS"

Bibliography

(1) Chen, W. T.; Zhu, A. Y.; Sanjeev, V.; Khorasaninejad, M.; Shi, Z.; Lee, E.; Capasso, F. A Broadband Achromatic Metalens for Focusing and Imaging in the Visible. *Nature Nanotech* **2018**, *13* (3), 220–226. https://doi.org/10.1038/s41565-017-0034-6.

(2) Shrestha, S.; Overvig, A.; Lu, M.; Stein, A.; Yu, N. Multi-Element Metasurface System for Imaging in the near-Infrared. *Applied Physics Letters* **2023**, *122* (20), 201701. https://doi.org/10.1063/5.0141881.

(3) Jiang, Q.; Hu, L.; Geng, G.; Li, J.; Wang, Y.; Huang, L. Arbitrary Amplitude and Phase Control in Visible by Dielectric Metasurface. *Opt. Express* **2022**, *30* (8), 13530. https://doi.org/10.1364/OE.454967.

(4) Yamada, N.; Saito, H.; Ikezawa, S.; Iwami, K. Demonstration of a Multicolor Metasurface Holographic Movie Based on a Cinematographic Approach. *Opt. Express* **2022**, *30* (10), 17591. https://doi.org/10.1364/OE.457460.

(5) Devlin, R. C.; Ambrosio, A.; Rubin, N. A.; Mueller, J. P. B.; Capasso, F. Arbitrary Spin-to–Orbital Angular Momentum Conversion of Light. *Science* **2017**, *358* (6365), 896–901. https://doi.org/10.1126/science.aao5392.

(6) Yang, Y.; Wang, W.; Moitra, P.; Kravchenko, I. I.; Briggs, D. P.; Valentine, J. Dielectric Meta-Reflectarray for Broadband Linear Polarization Conversion and Optical Vortex Generation. *Nano Lett.* **2014**, *14* (3), 1394–1399. https://doi.org/10.1021/nl4044482.

(7) Tan, Q.; Zheng, B.; Cai, T.; Qian, C.; Zhu, R.; Li, X.; Chen, H. Broadband Spin-Locked Metasurface Retroreflector. *Advanced Science* **2022**, 2201397. https://doi.org/10.1002/advs.202201397.

(8) Lee, H.; Kwon, D.-H. Microwave Metasurface Cloaking for Freestanding Objects. *Phys. Rev. Applied* **2022**, *17* (5), 054012. https://doi.org/10.1103/PhysRevApplied.17.054012.

(9) Kamali, S. M.; Arbabi, E.; Arbabi, A.; Faraon, A. A Review of Dielectric Optical Metasurfaces for Wavefront Control. *Nanophotonics* **2018**, *7* (6), 1041–1068. https://doi.org/10.1515/nanoph-2017-0129.

(10) Chen, H.-T.; Taylor, A. J.; Yu, N. A Review of Metasurfaces: Physics and Applications. *Rep. Prog. Phys.* **2016**, *79* (7), 076401. https://doi.org/10.1088/0034-4885/79/7/076401.

(11) Overvig, A.; Alù, A. Diffractive Nonlocal Metasurfaces. *Laser & Photonics Reviews* **2022**, 2100633. https://doi.org/10.1002/lpor.202100633.

(12) Badloe, T.; Mun, J.; Rho, J. Metasurfaces-Based Absorption and Reflection Control: Perfect Absorbers and Reflectors. *Journal of Nanomaterials* **2017**, *2017*, 1–18. https://doi.org/10.1155/2017/2361042.

(13) Kim, I.; Martins, R. J.; Jang, J.; Badloe, T.; Khadir, S.; Jung, H.-Y.; Kim, H.; Kim, J.; Genevet, P.; Rho, J. Nanophotonics for Light Detection and Ranging Technology. *Nat. Nanotechnol.* **2021**, *16* (5), 508–524. https://doi.org/10.1038/s41565-021-00895-3.

(14) Shaltout, A. M.; Shalaev, V. M.; Brongersma, M. L. Spatiotemporal Light Control with Active Metasurfaces. *Science* **2019**, *364* (6441), eaat3100. https://doi.org/10.1126/science.aat3100.

(15) Hong, Y.-H.; Hsu, W.-C.; Tsai, W.-C.; Huang, Y.-W.; Chen, S.-C.; Kuo, H.-C. Ultracompact Nanophotonics: Light Emission and Manipulation with Metasurfaces. *Nanoscale Res Lett* **2022**, *17* (1), 41. https://doi.org/10.1186/s11671-022-03680-w.

(16) Alaee, R.; Filter, R.; Lehr, D.; Lederer, F.; Rockstuhl, C. A Generalized Kerker Condition for Highly Directive Nanoantennas. *Opt. Lett.* **2015**, *40* (11), 2645. https://doi.org/10.1364/OL.40.002645.

(17) Decker, M.; Staude, I.; Falkner, M.; Dominguez, J.; Neshev, D. N.; Brener, I.; Pertsch, T.; Kivshar, Y. S. High-Efficiency Dielectric Huygens' Surfaces. *Advanced Optical Materials* **2015**, *3* (6), 813–820. https://doi.org/10.1002/adom.201400584.

(18) Yu, N.; Genevet, P.; Kats, M. A.; Aieta, F.; Tetienne, J.-P.; Capasso, F.; Gaburro, Z. Light Propagation with Phase Discontinuities: Generalized Laws of Reflection and Refraction. *Science* **2011**, *334* (6054), 333–337. https://doi.org/10.1126/science.1210713.

(19) Lin, D.; Fan, P.; Hasman, E.; Brongersma, M. L. Dielectric Gradient Metasurface Optical Elements. *Science* **2014**, *345* (6194), 298–302. https://doi.org/10.1126/science.1253213.

(20) Genevet, P.; Yu, N.; Aieta, F.; Lin, J.; Kats, M. A.; Blanchard, R.; Scully, M. O.; Gaburro, Z.; Capasso, F. Ultra-Thin Plasmonic Optical Vortex Plate Based on Phase Discontinuities. *Applied Physics Letters* **2012**, *100* (1), 013101. https://doi.org/10.1063/1.3673334.

(21) Aieta, F.; Genevet, P.; Kats, M. A.; Yu, N.; Blanchard, R.; Gaburro, Z.; Capasso, F. Aberration-Free Ultrathin Flat Lenses and Axicons at Telecom Wavelengths Based on Plasmonic Metasurfaces. *Nano Lett.* **2012**, *12* (9), 4932–4936. https://doi.org/10.1021/nl302516v.

(22) Wang, H.; Yu, S.; Kou, N.; Ding, Z.; Zhang, Z. Cylindrical Holographic Impedance Metasurface for OAM Vortex Wave Generation. *Appl. Phys. Lett.* **2022**, *120* (14), 143504. https://doi.org/10.1063/5.0082907.

(23) Díaz-Rubio, A.; Li, J.; Shen, C.; Cummer, S. A.; Tretyakov, S. A. Power Flow–Conformal Metamirrors for Engineering Wave Reflections. *Sci. Adv.* **2019**, *5* (2), eaau7288. https://doi.org/10.1126/sciadv.aau7288.

(24) Yang, Q.; Kruk, S.; Xu, Y.; Wang, Q.; Srivastava, Y. K.; Koshelev, K.; Kravchenko, I.; Singh, R.; Han, J.; Kivshar, Y.; Shadrivov, I. Mie-Resonant Membrane Huygens' Metasurfaces. *Adv. Funct. Mater.* **2020**, *30* (4), 1906851. https://doi.org/10.1002/adfm.201906851.

(25) Choudhury, S.; Guler, U.; Shaltout, A.; Shalaev, V. M.; Kildishev, A. V.; Boltasseva, A. Pancharatnam–Berry Phase Manipulating Metasurface for Visible Color Hologram Based on Low Loss Silver Thin Film. *Advanced Optical Materials* **2017**, *5* (10), 1700196. https://doi.org/10.1002/adom.201700196.

(26) Luo, W.; Sun, S.; Xu, H.-X.; He, Q.; Zhou, L. Transmissive Ultrathin Pancharatnam-Berry Metasurfaces with Nearly 100% Efficiency. *Phys. Rev. Applied* **2017**, *7* (4), 044033. https://doi.org/10.1103/PhysRevApplied.7.044033.

(27) Berry, M. V. The Adiabatic Phase and Pancharatnam's Phase for Polarized Light. *Journal of Modern Optics* **1987**, *34* (11), 1401–1407. https://doi.org/10.1080/09500348714551321.

(28) Zhou, J.; Qian, H.; Chen, C.-F.; Zhao, J.; Li, G.; Wu, Q.; Luo, H.; Wen, S.; Liu, Z. Optical Edge Detection Based on High-Efficiency Dielectric Metasurface. *Proc.*

Natl. Acad. Sci. U.S.A. **2019**, *116* (23), 11137–11140. https://doi.org/10.1073/pnas.1820636116.

(29) Deng, Y.; Cai, Z.; Ding, Y.; Bozhevolnyi, S. I.; Ding, F. Recent Progress in Metasurface-Enabled Optical Waveplates. *Nanophotonics* **2022**, *0* (0). https://doi.org/10.1515/nanoph-2022-0030.

(30) Cui, Y.; Wang, X.; Ren, B.; Jiang, H.; Jiang, Y. High-Efficiency and Tunable Circular Polarization Selectivity in Photosensitive Silicon-Based Zigzag Array Metasurface. *Optics & Laser Technology* **2022**, *156*, 108453. https://doi.org/10.1016/j.optlastec.2022.108453.

(31) Lee, Y.-H.; Tan, G.; Zhan, T.; Weng, Y.; Liu, G.; Gou, F.; Peng, F.; Tabiryan, N. V.; Gauza, S.; Wu, S.-T. Recent Progress in Pancharatnam–Berry Phase Optical Elements and the Applications for Virtual/Augmented Realities. *Optical Data Processing and Storage* **2017**, *3* (1). https://doi.org/10.1515/odps-2017-0010.

(32) Luo, X. Subwavelength Optical Engineering with Metasurface Waves. *Advanced Optical Materials* **2018**, *6* (7), 1701201. https://doi.org/10.1002/adom.201701201.

(33) So, S.; Mun, J.; Park, J.; Rho, J. Revisiting the Design Strategies for Metasurfaces: Fundamental Physics, Optimization, and Beyond. *Advanced Materials* **2023**, 2206399. https://doi.org/10.1002/adma.202206399.

(34) Vaskin, A.; Kolkowski, R.; Koenderink, A. F.; Staude, I. Light-Emitting Metasurfaces. *Nanophotonics* **2019**, *8* (7), 1151–1198. https://doi.org/10.1515/nanoph-2019-0110.

(35) Yu, N.; Capasso, F. Flat Optics with Designer Metasurfaces. *Nature Mater* **2014**, *13* (2), 139–150. https://doi.org/10.1038/nmat3839.

(36) Zheng, Z.; Rocco, D.; Ren, H.; Sergaeva, O.; Zhang, Y.; Whaley, K. B.; Ying, C.; De Ceglia, D.; De-Angelis, C.; Rahmani, M.; Xu, L. Advances in Nonlinear Metasurfaces for Imaging, Quantum, and Sensing Applications. *Nanophotonics* **2023**, *12* (23), 4255–4281. https://doi.org/10.1515/nanoph-2023-0526.

(37) Bucher, T.; Vaskin, A.; Mupparapu, R.; Löchner, F. J. F.; George, A.; Chong, K. E.; Fasold, S.; Neumann, C.; Choi, D.-Y.; Eilenberger, F.; Setzpfandt, F.; Kivshar, Y. S.; Pertsch, T.; Turchanin, A.; Staude, I. Tailoring Photoluminescence from MoS_2 Monolayers by Mie-Resonant Metasurfaces. *ACS Photonics* **2019**, *6* (4), 1002–1009. https://doi.org/10.1021/acsphotonics.8b01771.

(38) Lozano, G.; Grzela, G.; Verschuuren, M. A.; Ramezani, M.; Rivas, J. G. Tailor-Made Directional Emission in Nanoimprinted Plasmonic-Based Light-Emitting Devices. *Nanoscale* **2014**, *6* (15), 9223–9229. https://doi.org/10.1039/C4NR01391C.

(39) Dong, Z.; Gorelik, S.; Paniagua-Dominguez, R.; Yik, J.; Ho, J.; Tjiptoharsono, F.; Lassalle, E.; Rezaei, S. D.; Neo, D. C. J.; Bai, P.; Kuznetsov, A. I.; Yang, J. K. W. Silicon Nanoantenna Mix Arrays for a Trifecta of Quantum Emitter Enhancements. *Nano Lett.* **2021**, *21* (11), 4853–4860. https://doi.org/10.1021/acs.nanolett.1c01570.

(40) Klein, M.; Wang, Y.; Tian, J.; Ha, S. T.; Paniagua-Domínguez, R.; Kuznetsov, A. I.; Adamo, G.; Soci, C. Polarization-Tunable Perovskite Light-Emitting Metatransistor. *Advanced Materials* **2023**, *35* (1), 2207317. https://doi.org/10.1002/adma.202207317.

(41) Knudson, M. P.; Li, R.; Wang, D.; Wang, W.; Schaller, R. D.; Odom, T. W. Polarization-Dependent Lasing Behavior from Low-Symmetry Nanocavity Arrays. *ACS Nano* **2019**, *13* (7), 7435–7441. https://doi.org/10.1021/acsnano.9b01142.

(42) Asamoah, B. O.; Partanen, H.; Mohamed, S.; Heikkinen, J.; Halder, A.; Koivurova, M.; Nečada, M.; Setälä, T.; Turunen, J.; Friberg, A. T.; Hakala, T. K. Polarization Dependent Beaming Properties of a Plasmonic Lattice Laser. *New J. Phys.* **2021**, *23* (6), 063037. https://doi.org/10.1088/1367-2630/ac0286.

(43) Lin, Y.-T.; Hassanfiroozi, A.; Jiang, W.-R.; Liao, M.-Y.; Lee, W.-J.; Wu, P. C. Photoluminescence Enhancement with All-Dielectric Coherent Metasurfaces. *Nanophotonics* **2022**, *11* (11), 2701–2709. https://doi.org/10.1515/nanoph-2021-0640.

(44) Muscarella, L. A.; Cordaro, A.; Krause, G.; Pal, D.; Grimaldi, G.; Antony, L. S. D.; Langhorst, D.; Callies, A.; Bläsi, B.; Höhn, O.; Koenderink, A. F.; Polman, A.; Ehrler, B. Nanopatterning of Perovskite Thin Films for Enhanced and Directional Light Emission. *ACS Appl. Mater. Interfaces* **2022**, *14* (33), 38067–38076. https://doi.org/10.1021/acsami.2c09643.

(45) Liu, S.; Vaskin, A.; Addamane, S.; Leung, B.; Tsai, M.-C.; Yang, Y.; Vabishchevich, P. P.; Keeler, G. A.; Wang, G.; He, X.; Kim, Y.; Hartmann, N. F.; Htoon, H.; Doorn, S. K.; Zilk, M.; Pertsch, T.; Balakrishnan, G.; Sinclair, M. B.; Staude, I.; Igal Brener. Light-Emitting Metasurfaces: Simultaneous Control of Spontaneous Emission and Far-Field Radiation. *Nano Lett.* **2018**, *18* (11), 6906–6914. https://doi.org/10.1021/acs.nanolett.8b02808.

(46) Ha, S. T.; Fu, Y. H.; Emani, N. K.; Pan, Z.; Bakker, R. M.; Paniagua-Domínguez, R.; Kuznetsov, A. I. Directional Lasing in Resonant Semiconductor Nanoantenna Arrays. *Nature Nanotech* **2018**, *13* (11), 1042–1047. https://doi.org/10.1038/s41565-018-0245-5.

(47) Bailly, E.; Hugonin, J.-P.; Coudevylle, J.-R.; Dabard, C.; Ithurria, S.; Vest, B.; Greffet, J.-J. 2D Silver-Nanoplatelets Metasurface for Bright Directional Photoluminescence, Designed with the Local Kirchhoff's Law. **2023**. https://doi.org/10.48550/ARXIV.2309.17374.

(48) Khaidarov, E.; Liu, Z.; Paniagua-Domínguez, R.; Ha, S. T.; Valuckas, V.; Liang, X.; Akimov, Y.; Bai, P.; Png, C. E.; Demir, H. V.; Kuznetsov, A. I. Control of LED Emission with Functional Dielectric Metasurfaces. *Laser & Photonics Reviews* **2020**, *14* (1), 1900235. https://doi.org/10.1002/lpor.201900235.

(49) Xie, Y.-Y.; Ni, P.-N.; Wang, Q.-H.; Kan, Q.; Briere, G.; Chen, P.-P.; Zhao, Z.-Z.; Delga, A.; Ren, H.-R.; Chen, H.-D.; Xu, C.; Genevet, P. Metasurface-Integrated Vertical Cavity Surface-Emitting Lasers for Programmable Directional Lasing Emissions. *Nat. Nanotechnol.* **2020**, *15* (2), 125–130. https://doi.org/10.1038/s41565-019-0611-y.

(50) Huang, J.; Hu, Z.; Gao, X.; Xu, Y.; Wang, L. Unidirectional-Emitting GaN-Based Micro-LED for 3D Display. *Opt. Lett.* **2021**, *46* (14), 3476. https://doi.org/10.1364/OL.430021.

(51) Huang, H.; Zheng, S.; Sun, W. Beam Manipulation for Quantum Dot Light-Emitting Diode with an Ag Grating and a Phase-Gradient Metasurface. *Opt. Express* **2022**, *30* (16), 28345. https://doi.org/10.1364/OE.463772.

(52) Wang, M.; Xu, F.; Lin, Y.; Cao, B.; Chen, L.; Wang, C.; Wang, J.; Xu, K. Metasurface Integrated High Energy Efficient and High Linearly Polarized InGaN/GaN Light Emitting Diode. *Nanoscale* **2017**, *9* (26), 9104–9111. https://doi.org/10.1039/C7NR00539C.

(53) Wang, X.; Li, Y.; Toufanian, R.; Kogos, L. C.; Dennis, A. M.; Paiella, R. Geometrically Tunable Beamed Light Emission from a Quantum-Dot Ensemble Near a Gradient Metasurface. *Adv. Optical Mater.* **2020**, *8* (8), 1901951. https://doi.org/10.1002/adom.201901951.

(54) Iyer, P. P.; DeCrescent, R. A.; Mohtashami, Y.; Lheureux, G.; Butakov, N. A.; Alhassan, A.; Weisbuch, C.; Nakamura, S.; DenBaars, S. P.; Schuller, Jon. A. Unidirectional Luminescence from InGaN/GaN Quantum-Well Metasurfaces. *Nat. Photonics* **2020**, *14* (9), 543–548. https://doi.org/10.1038/s41566-020-0641-x.

(55) Jones, D. R.; Schonlau, M.; Welch, W. J. Efficient Global Optimization of Expensive Black-Box Functions. *Journal of Global Optimization* **1998**, *13* (4), 455–492. https://doi.org/10.1023/A:1008306431147.

(56) Schneider, P.-I.; Garcia Santiago, X.; Soltwisch, V.; Hammerschmidt, M.; Burger, S.; Rockstuhl, C. Benchmarking Five Global Optimization Approaches for Nano-Optical Shape Optimization and Parameter Reconstruction. *ACS Photonics* **2019**, *6* (11), 2726–2733. https://doi.org/10.1021/acsphotonics.9b00706.

(57) Cressie, N. The Origins of Kriging. *Math Geol* **1990**, *22* (3), 239–252. https://doi.org/10.1007/BF00889887.

(58) Arbabi, A.; Horie, Y.; Bagheri, M.; Faraon, A. Dielectric Metasurfaces for Complete Control of Phase and Polarization with Subwavelength Spatial Resolution and High Transmission. *Nature Nanotech* **2015**, *10* (11), 937–943. https://doi.org/10.1038/nnano.2015.186.

(59) Khorasaninejad, M.; Zhu, W.; Crozier, K. B. Efficient Polarization Beam Splitter Pixels Based on a Dielectric Metasurface. *Optica* **2015**, *2* (4), 376. https://doi.org/10.1364/OPTICA.2.000376.

(60) Khorasaninejad, M.; Chen, W. T.; Devlin, R. C.; Oh, J.; Zhu, A. Y.; Capasso, F. Metalenses at Visible Wavelengths: Diffraction-Limited Focusing and Subwavelength Resolution Imaging. *Science* **2016**, *352* (6290), 1190–1194. https://doi.org/10.1126/science.aaf6644.

(61) Liu, M.; Zhu, W.; Huo, P.; Feng, L.; Song, M.; Zhang, C.; Chen, L.; Lezec, H. J.; Lu, Y.; Agrawal, A.; Xu, T. Multifunctional Metasurfaces Enabled by Simultaneous and Independent Control of Phase and Amplitude for Orthogonal Polarization States. *Light Sci Appl* **2021**, *10* (1), 107. https://doi.org/10.1038/s41377-021-00552-3.

(62) Ni, X.; Kildishev, A. V.; Shalaev, V. M. Metasurface Holograms for Visible Light. *Nat Commun* **2013**, *4* (1), 2807. https://doi.org/10.1038/ncomms3807.

(63) Liu, M.; Huo, P.; Zhu, W.; Zhang, C.; Zhang, S.; Song, M.; Zhang, S.; Zhou, Q.; Chen, L.; Lezec, H. J.; Agrawal, A.; Lu, Y.; Xu, T. Broadband Generation of Perfect Poincaré Beams via Dielectric Spin-Multiplexed Metasurface. *Nat Commun* **2021**, *12* (1), 2230. https://doi.org/10.1038/s41467-021-22462-z.

(64) Curto, A. G.; Volpe, G.; Taminiau, T. H.; Kreuzer, M. P.; Quidant, R.; van Hulst, N. F. Unidirectional Emission of a Quantum Dot Coupled to a Nanoantenna. *Science* **2010**, *329* (5994), 930–933. https://doi.org/10.1126/science.1191922.

(65) Kosako, T.; Kadoya, Y.; Hofmann, H. F. Directional Control of Light by a Nano-Optical Yagi–Uda Antenna. *Nature Photon* **2010**, *4* (5), 312–315. https://doi.org/10.1038/nphoton.2010.34.

(66) Langguth, L.; Schokker, A. H.; Guo, K.; Koenderink, A. F. Plasmonic Phase-Gradient Metasurface for Spontaneous Emission Control. *Phys. Rev. B* **2015**, *92* (20), 205401. https://doi.org/10.1103/PhysRevB.92.205401.

(67) Hancu, I. M.; Curto, A. G.; Castro-López, M.; Kuttge, M.; van Hulst, N. F. Multipolar Interference for Directed Light Emission. *Nano Lett.* **2014**, *14* (1), 166–171. https://doi.org/10.1021/nl403681g.

(68) Vaskin, A.; Liu, S.; Addamane, S.; Vabishchevich, P. P.; Yang, Y.; Balarishnan, G.; Sinclair, M. B.; Pertsch, T.; Brener, I.; Staude, I. Manipulation of Quantum Dot Emission with Semiconductor Metasurfaces Exhibiting Magnetic Quadrupole Resonances. *Opt. Express* **2021**, *29* (4), 5567. https://doi.org/10.1364/OE.414011.

(69) Vaskin, A.; Bohn, J.; Chong, K. E.; Bucher, T.; Zilk, M.; Choi, D.-Y.; Neshev, D. N.; Kivshar, Y. S.; Pertsch, T.; Staude, I. Directional and Spectral Shaping of Light Emission with Mie-Resonant Silicon Nanoantenna Arrays. *ACS Photonics* **2018**, *5* (4), 1359–1364. https://doi.org/10.1021/acsphotonics.7b01375.

(70) Luo, S.; Li, Q.; Yang, Y.; Chen, X.; Wang, W.; Qu, Y.; Qiu, M. Controlling Fluorescence Emission with Split-Ring-Resonator-Based Plasmonic Metasurfaces: Controlling Fluorescence Emission with Split-Ring-Resonator-Based Plasmonic Metasurfaces. *Laser & Photonics Reviews* **2017**, *11* (3), 1600299. https://doi.org/10.1002/lpor.201600299.

(71) Laux, F.; Bonod, N.; Gérard, D. Single Emitter Fluorescence Enhancement with Surface Lattice Resonances. *J. Phys. Chem. C* **2017**, *121* (24), 13280–13289. https://doi.org/10.1021/acs.jpcc.7b04207.

(72) Mohtashami, Y.; DeCrescent, R. A.; Heki, L. K.; Iyer, P. P.; Butakov, N. A.; Wong, M. S.; Alhassan, A.; Mitchell, W. J.; Nakamura, S.; DenBaars, S. P.; Schuller, Jon. A. Light-Emitting Metalenses and Meta-Axicons for Focusing and Beaming of Spontaneous Emission. *Nat Commun* **2021**, *12* (1), 3591. https://doi.org/10.1038/s41467-021-23433-0.

(73) Zhang, S.; Martins, E. R.; Diyaf, A. G.; Wilson, J. I. B.; Turnbull, G. A.; Samuel, I. D. W. Calculation of the Emission Power Distribution of Microstructured OLEDs Using the Reciprocity Theorem. *Synthetic Metals* **2015**, *205*, 127–133. https://doi.org/10.1016/j.synthmet.2015.03.035.

(74) Rau, U. Superposition and Reciprocity in the Electroluminescence and Photoluminescence of Solar Cells. *IEEE J. Photovoltaics* **2012**, *2* (2), 169–172. https://doi.org/10.1109/JPHOTOV.2011.2179018.

(75) Elsawy, M. M. R.; Lanteri, S.; Duvigneau, R.; Brière, G.; Mohamed, M. S.; Genevet, P. Global Optimization of Metasurface Designs Using Statistical Learning Methods. *Sci Rep* **2019**, *9* (1), 17918. https://doi.org/10.1038/s41598-019-53878-9.

(76) Lin, C.-H.; Chen, Y.-S.; Lin, J.-T.; Wu, H. C.; Kuo, H.-T.; Lin, C.-F.; Chen, P.; Wu, P. C. Automatic Inverse Design of High-Performance Beam-Steering Metasurfaces via Genetic-Type Tree Optimization. *Nano Lett.* **2021**, *21* (12), 4981–4989. https://doi.org/10.1021/acs.nanolett.1c00720.

(77) Sell, D.; Yang, J.; Doshay, S.; Yang, R.; Fan, J. A. Large-Angle, Multifunctional Metagratings Based on Freeform Multimode Geometries. *Nano Lett.* **2017**, *17* (6), 3752–3757. https://doi.org/10.1021/acs.nanolett.7b01082.

(78) Cong, L.; Singh, R. Spatiotemporal Dielectric Metasurfaces for Unidirectional Propagation and Reconfigurable Steering of Terahertz Beams. *Adv. Mater.* **2020**, *32* (28), 2001418. https://doi.org/10.1002/adma.202001418.

(79) Mansouree, M.; McClung, A.; Samudrala, S.; Arbabi, A. Large-Scale Parametrized Metasurface Design Using Adjoint Optimization. *ACS Photonics* **2021**, *8* (2), 455–463. https://doi.org/10.1021/acsphotonics.0c01058.

(80) Arbabi, A.; Horie, Y.; Ball, A. J.; Bagheri, M.; Faraon, A. Subwavelength-Thick Lenses with High Numerical Apertures and Large Efficiency Based on High-Contrast Transmitarrays. *Nat Commun* **2015**, *6* (1), 7069. https://doi.org/10.1038/ncomms8069.

(81) Bayati, E.; Pestourie, R.; Colburn, S.; Lin, Z.; Johnson, S. G.; Majumdar, A. Inverse Designed Metalenses with Extended Depth of Focus. *ACS Photonics* **2020**, *7* (4), 873–878. https://doi.org/10.1021/acsphotonics.9b01703.

(82) Phan, T.; Sell, D.; Wang, E. W.; Doshay, S.; Edee, K.; Yang, J.; Fan, J. A. High-Efficiency, Large-Area, Topology-Optimized Metasurfaces. *Light Sci Appl* **2019**, *8* (1), 48. https://doi.org/10.1038/s41377-019-0159-5.

(83) Lin, D.; Fan, P.; Hasman, E.; Brongersma, M. L. Dielectric Gradient Metasurface Optical Elements. *Science* **2014**, *345* (6194), 298–302. https://doi.org/10.1126/science.1253213.

(84) Zheng, G.; Mühlenbernd, H.; Kenney, M.; Li, G.; Zentgraf, T.; Zhang, S. Metasurface Holograms Reaching 80% Efficiency. *Nature Nanotech* **2015**, *10* (4), 308–312. https://doi.org/10.1038/nnano.2015.2.

(85) Backer, A. S. Computational Inverse Design for Cascaded Systems of Metasurface Optics. *Opt. Express* **2019**, *27* (21), 30308. https://doi.org/10.1364/OE.27.030308.

(86) Iwanaga, M.; Hironaka, T.; Ikeda, N.; Sugasawa, T.; Takekoshi, K. Metasurface Biosensors Enabling Single-Molecule Sensing of Cell-Free DNA. *Nano Lett.* **2023**, *23* (12), 5755–5761. https://doi.org/10.1021/acs.nanolett.3c01527.

(87) Wang, L.; Wang, T.; Yan, R.; Yue, X.; Wang, H.; Wang, Y.; Zhang, J.; Yuan, X.; Zeng, J.; Wang, J. Color Printing and Encryption with Polarization-Switchable Structural Colors on All-Dielectric Metasurfaces. *Nano Lett.* **2023**, *23* (12), 5581–5587. https://doi.org/10.1021/acs.nanolett.3c01007.

(88) Hughes, T. W.; Minkov, M.; Williamson, I. A. D.; Fan, S. Adjoint Method and Inverse Design for Nonlinear Nanophotonic Devices. *ACS Photonics* **2018**, *5* (12), 4781–4787. https://doi.org/10.1021/acsphotonics.8b01522.

(89) Li, Z.; Dai, Q.; Mehmood, M. Q.; Hu, G.; Yanchuk, B. L.; Tao, J.; Hao, C.; Kim, I.; Jeong, H.; Zheng, G.; Yu, S.; Alù, A.; Rho, J.; Qiu, C.-W. Full-Space Cloud of Random Points with a Scrambling Metasurface. *Light Sci Appl* **2018**, *7* (1), 63. https://doi.org/10.1038/s41377-018-0064-3.

(90) Yu, N.; Genevet, P.; Kats, M. A.; Aieta, F.; Tetienne, J.-P.; Capasso, F.; Gaburro, Z. Light Propagation with Phase Discontinuities: Generalized Laws of Reflection and Refraction. *Science* **2011**, *334* (6054), 333–337. https://doi.org/10.1126/science.1210713.

(91) Iyer, P. P.; Karl, N.; Addamane, S.; Gennaro, S. D.; Sinclair, M. B.; Brener, I. Sub-Picosecond Steering of Ultrafast Incoherent Emission from Semiconductor

Metasurfaces. *Nat. Photon.* **2023**, *17* (7), 588–593. https://doi.org/10.1038/s41566-023-01172-6.

(92) Iyer, P. P.; Desai, S.; Addamane, S.; Dingreville, R.; Brener, I. Learning Incoherent Light Emission Steering From Metasurfaces Using Generative Models. *Proceedings of the IEEE/CVF Winter Conference on Applications of Computer Vision (WACV)* **2023**, 3770–3777.

(93) Shih, K.-H.; Renshaw, C. K. Broadband Metasurface Aberration Orrectors for Hybrid Meta/Refractive MWIR Lenses. *Opt. Express* **2022**, *30* (16), 28438. https://doi.org/10.1364/OE.460941.

(94) Van Der Burgt, J. S.; Dieleman, C. D.; Johlin, E.; Geuchies, J. J.; Houtepen, A. J.; Ehrler, B.; Garnett, E. C. Integrating Sphere Fourier Microscopy of Highly Directional Emission. *ACS Photonics* **2021**, *8* (4), 1143–1151. https://doi.org/10.1021/acsphotonics.1c00010.

(95) Chen, W.-Q.; Zhang, D.-S.; Long, S.-Y.; Liu, Z.-Z.; Xiao, J.-J. Nearly Dispersionless Multicolor Metasurface Beam Deflector for near Eye Display Designed by a Physics-Driven Deep Neural Network. *Appl. Opt.* **2021**, *60* (13), 3947. https://doi.org/10.1364/AO.421901.

(96) Heki, L.; Mohtashami, Y.; DeCrescent, R. A.; Alhassan, A.; Nakamura, S.; DenBaars, S. P.; Schuller, J. A. Designing Highly Directional Luminescent Phased-Array Metasurfaces with Reciprocity-Based Simulations. *ACS Omega* **2022**, *7* (26), 22477–22483. https://doi.org/10.1021/acsomega.2c01654.

(97) Mohtashami, Y.; Heki, L. K.; Wong, M. S.; Smith, J. M.; Ewing, J. J.; Mitchell, W. J.; Nakamura, S.; DenBaars, S. P.; Schuller, J. A. Metasurface Light-Emitting

Diodes with Directional and Focused Emission. *Nano Lett.* **2023**, *23* (22), 10505–10511. https://doi.org/10.1021/acs.nanolett.3c03272.

(98) Leung, M. M. Y.; Djurišić, A. B.; Li, E. H. Refractive Index of InGaN/GaN Quantum Well. *Journal of Applied Physics* **1998**, *84* (11), 6312–6317. https://doi.org/10.1063/1.368954.

(99) *III-Nitride Based Light Emitting Diodes and Applications*; Seong, T.-Y., Han, J., Amano, H., Morkoc, H., Eds.; Topics in Applied Physics; Springer Netherlands: Dordrecht, 2013; Vol. 126. https://doi.org/10.1007/978-94-007-5863-6.

(100) Chen, H.-T.; Taylor, A. J.; Yu, N. A Review of Metasurfaces: Physics and Applications. *Rep. Prog. Phys.* **2016**, *79* (7), 076401. https://doi.org/10.1088/0034-4885/79/7/076401.

(101) He, Q.; Sun, S.; Xiao, S.; Zhou, L. High-Efficiency Metasurfaces: Principles, Realizations, and Applications. *Advanced Optical Materials* **2018**, *6* (19), 1800415. https://doi.org/10.1002/adom.201800415.

(102) Cheng, J.; Inampudi, S.; Mosallaei, H. Optimization-Based Dielectric Metasurfaces for Angle-Selective Multifunctional Beam Deflection. *Sci Rep* **2017**, *7* (1), 12228. https://doi.org/10.1038/s41598-017-12541-x.

(103) Akram, M. R.; Ding, G.; Chen, K.; Feng, Y.; Zhu, W. Ultrathin Single Layer Metasurfaces with Ultra-Wideband Operation for Both Transmission and Reflection. *Adv. Mater.* **2020**, *32* (12), 1907308. https://doi.org/10.1002/adma.201907308.

(104) Born, B.; Lee, S.-H.; Song, J.-H.; Lee, J. Y.; Ko, W.; Brongersma, M. L. Off-Axis Metasurfaces for Folded Flat Optics. *Nat Commun* **2023**, *14* (1), 5602. https://doi.org/10.1038/s41467-023-41123-x.

(105) Murtaza Rind, Y.; Mahmood, N.; Javed, I.; Gao, L.; Tauqeer, T.; Cabrera, H.; Zubair, M.; Massoud, Y.; Mehmood, M. Q. Broadband Multifunctional Metasurfaces Enabling Polarization Multiplexed Focused Vortex Array Generation. *Materials Today Communications* **2024**, *38*, 107648. https://doi.org/10.1016/j.mtcomm.2023.107648.

(106) *Advances in Spectroscopic Monitoring of the Atmosphere*; Elsevier, 2021. https://doi.org/10.1016/C2017-0-02805-7.

(107) Rabinovich, W. S.; Moore, C. I.; Burris, H. R.; Murphy, J. L.; Suite, M. R.; Mahon, R.; Ferraro, M. S.; Goetz, P. G.; Thomas, L. M.; Font, C.; Gilbreath, G. C.; Xu, B.; Binari, S.; Hacker, K.; Reese, S.; Freeman, W. T.; Frawley, S.; Saint-Georges, E.; Uecke, S.; Sender, J. Free Space Optical Communications Research at the U.S. Naval Research Laboratory; Hemmati, H., Ed.; San Francisco, California, USA, 2010; p 758702. https://doi.org/10.1117/12.843682.

(108) Sośnica, K.; Thaller, D.; Dach, R.; Steigenberger, P.; Beutler, G.; Arnold, D.; Jäggi, A. Satellite Laser Ranging to GPS and GLONASS. *J Geod* **2015**, *89* (7), 725–743. https://doi.org/10.1007/s00190-015-0810-8.

(109) Strugarek, D.; Sośnica, K.; Jäggi, A. Characteristics of GOCE Orbits Based on Satellite Laser Ranging. *Advances in Space Research* **2019**, *63* (1), 417–431. https://doi.org/10.1016/j.asr.2018.08.033.

(110) Liu, L.; Lü, D.-S.; Chen, W.-B.; Li, T.; Qu, Q.-Z.; Wang, B.; Li, L.; Ren, W.; Dong, Z.-R.; Zhao, J.-B.; Xia, W.-B.; Zhao, X.; Ji, J.-W.; Ye, M.-F.; Sun, Y.-G.; Yao, Y.-Y.; Song, D.; Liang, Z.-G.; Hu, S.-J.; Yu, D.-H.; Hou, X.; Shi, W.; Zang, H.-G.; Xiang, J.-F.; Peng, X.-K.; Wang, Y.-Z. In-Orbit Operation of an Atomic Clock Based on Laser-

Cooled 87Rb Atoms. *Nat Commun* **2018**, *9* (1), 2760. https://doi.org/10.1038/s41467-018-05219-z.

(111) Ladd, T. D.; Jelezko, F.; Laflamme, R.; Nakamura, Y.; Monroe, C.; O'Brien, J. L. Quantum Computers. *Nature* **2010**, *464* (7285), 45–53. https://doi.org/10.1038/nature08812.

(112) Bloch, I. Quantum Coherence and Entanglement with Ultracold Atoms in Optical Lattices. *Nature* **2008**, *453* (7198), 1016–1022. https://doi.org/10.1038/nature07126.

(113) Bongs, K.; Holynski, M.; Vovrosh, J.; Bouyer, P.; Condon, G.; Rasel, E.; Schubert, C.; Schleich, W. P.; Roura, A. Author Correction: Taking Atom Interferometric Quantum Sensors from the Laboratory to Real-World Applications. *Nat Rev Phys* **2021**, *3* (12), 814–814. https://doi.org/10.1038/s42254-021-00396-1.

(114) Stray, B.; Lamb, A.; Kaushik, A.; Vovrosh, J.; Rodgers, A.; Winch, J.; Hayati, F.; Boddice, D.; Stabrawa, A.; Niggebaum, A.; Langlois, M.; Lien, Y.-H.; Lellouch, S.; Roshanmanesh, S.; Ridley, K.; De Villiers, G.; Brown, G.; Cross, T.; Tuckwell, G.; Faramarzi, A.; Metje, N.; Bongs, K.; Holynski, M. Quantum Sensing for Gravity Cartography. *Nature* **2022**, *602* (7898), 590–594. https://doi.org/10.1038/s41586-021-04315-3.

(115) Chu, S.; Hollberg, L.; Bjorkholm, J. E.; Cable, A.; Ashkin, A. Three-Dimensional Viscous Confinement and Cooling of Atoms by Resonance Radiation Pressure. *Phys. Rev. Lett.* **1985**, *55* (1), 48–51. https://doi.org/10.1103/PhysRevLett.55.48.

(116) Steane, A. M.; Chowdhury, M.; Foot, C. J. Radiation Force in the Magneto-Optical Trap. *J. Opt. Soc. Am. B* **1992**, *9* (12), 2142. https://doi.org/10.1364/JOSAB.9.002142.

(117) Metcalf, H. J.; Van Der Straten, P. Laser Cooling and Trapping of Neutral Atoms. In *The Optics Encyclopedia*; Brown, T. G., Creath, K., Kogelnik, H., Kriss, M. A., Schmit, J., Weber, M. J., Eds.; Wiley, 2007. https://doi.org/10.1002/9783527600441.oe005.

(118) Ashkin, A.; Gordon, J. P. Cooling and Trapping of Atoms by Resonance Radiation Pressure. *Opt. Lett.* **1979**, *4* (6), 161. https://doi.org/10.1364/OL.4.000161.

(119) Rushton, J. A.; Aldous, M.; Himsworth, M. D. Contributed Review: The Feasibility of a Fully Miniaturized Magneto-Optical Trap for Portable Ultracold Quantum Technology. *Review of Scientific Instruments* **2014**, *85* (12), 121501. https://doi.org/10.1063/1.4904066.

(120) Kohel, J. M.; Ramirez-Serrano, J.; Thompson, R. J.; Maleki, L.; Bliss, J. L.; Libbrecht, K. G. Generation of an Intense Cold-Atom Beam from a Pyramidal Magneto-Optical Trap: Experiment and Simulation. *J. Opt. Soc. Am. B* **2003**, *20* (6), 1161. https://doi.org/10.1364/JOSAB.20.001161.

(121) Lee, K. I.; Kim, J. A.; Noh, H. R.; Jhe, W. Single-Beam Atom Trap in a Pyramidal and Conical Hollow Mirror. *Opt. Lett.* **1996**, *21* (15), 1177. https://doi.org/10.1364/OL.21.001177.

(122) Vangeleyn, M.; Griffin, P. F.; Riis, E.; Arnold, A. S. Laser Cooling with a Single Laser Beam and a Planar Diffractor. *Opt. Lett.* **2010**, *35* (20), 3453. https://doi.org/10.1364/OL.35.003453.

(123) Nshii, C. C.; Vangeleyn, M.; Cotter, J. P.; Griffin, P. F.; Hinds, E. A.; Ironside, C. N.; See, P.; Sinclair, A. G.; Riis, E.; Arnold, A. S. A Surface-Patterned Chip as a Strong Source of Ultracold Atoms for Quantum Technologies. *Nature Nanotech* **2013**, *8* (5), 321–324. https://doi.org/10.1038/nnano.2013.47.

(124) McGilligan, J. P.; Griffin, P. F.; Elvin, R.; Ingleby, S. J.; Riis, E.; Arnold, A. S. Grating Chips for Quantum Technologies. *Sci Rep* **2017**, *7* (1), 384. https://doi.org/10.1038/s41598-017-00254-0.

(125) Zhu, L.; Liu, X.; Sain, B.; Wang, M.; Schlickriede, C.; Tang, Y.; Deng, J.; Li, K.; Yang, J.; Holynski, M.; Zhang, S.; Zentgraf, T.; Bongs, K.; Lien, Y.-H.; Li, G. A Dielectric Metasurface Optical Chip for the Generation of Cold Atoms. *Sci. Adv.* **2020**, *6* (31), eabb6667. https://doi.org/10.1126/sciadv.abb6667.

(126) McGehee, W. R.; Zhu, W.; Barker, D. S.; Westly, D.; Yulaev, A.; Klimov, N.; Agrawal, A.; Eckel, S.; Aksyuk, V.; McClelland, J. J. Magneto-Optical Trapping Using Planar Optics. *New J. Phys.* **2021**, *23* (1), 013021. https://doi.org/10.1088/1367-2630/abdce3.

(127) Isichenko, A.; Chauhan, N.; Bose, D.; Wang, J.; Kunz, P. D.; Blumenthal, D. J. Photonic Integrated Beam Delivery for a Rubidium 3D Magneto-Optical Trap. *Nat Commun* **2023**, *14* (1), 3080. https://doi.org/10.1038/s41467-023-38818-6.

(128) Dong, S.; Hu, G.; Wang, Q.; Jia, Y.; Zhang, Q.; Cao, G.; Wang, J.; Chen, S.; Fan, D.; Jiang, W.; Li, Y.; Alù, A.; Qiu, C.-W. Loss-Assisted Metasurface at an Exceptional Point. *ACS Photonics* **2020**, *7* (12), 3321–3327. https://doi.org/10.1021/acsphotonics.0c01440.

(129) Wong, A. M. H.; Christian, P.; Eleftheriades, G. V. Binary Huygens' Metasurfaces: Experimental Demonstration of Simple and Efficient Near-Grazing Retroreflectors for TE and TM Polarizations. *IEEE Trans. Antennas Propagat.* **2018**, *66* (6), 2892–2903. https://doi.org/10.1109/TAP.2018.2816792.

(130) Yepes, C.; Faenzi, M.; Maci, S.; Martini, E. Perfect Non-Specular Reflection with Polarization Control by Using a Locally Passive Metasurface Sheet on a Grounded Dielectric Slab. *Appl. Phys. Lett.* **2021**, *118* (23), 231601. https://doi.org/10.1063/5.0048970.

(131) Dong, Y.; Kang, W.; Sima, B.; Wu, W. Retroreflector with Polarization Isolation Based on Nonreciprocal Metasurface. *Antennas Wirel. Propag. Lett.* **2022**, 1–5. https://doi.org/10.1109/LAWP.2022.3186334.

(132) Liu, C.; He, J.; Zhou, J.; Xu, J.; Bi, K.; Chen, J.; Qiao, L.; Bai, Y. Broadband, High-Efficiency and Wide-Incident-Angle Anomalous Reflection in Groove Metagratings. *Annalen der Physik* **2021**, *533* (9), 2100149. https://doi.org/10.1002/andp.202100149.

(133) Estakhri, N. M.; Neder, V.; Knight, M. W.; Polman, A.; Alù, A. Visible Light, Wide-Angle Graded Metasurface for Back Reflection. *ACS Photonics* **2017**, *4* (2), 228–235. https://doi.org/10.1021/acsphotonics.6b00965.

(134) Arbabi, A.; Arbabi, E.; Horie, Y.; Kamali, S. M.; Faraon, A. Planar Metasurface Retroreflector. *Nature Photon* **2017**, *11* (7), 415–420. https://doi.org/10.1038/nphoton.2017.96.

(135) Rubin, N. A.; Shi, Z.; Capasso, F. Polarization in Diffractive Optics and Metasurfaces. *Adv. Opt. Photon.* **2021**, *13* (4), 836. https://doi.org/10.1364/AOP.439986.

(136) Shi, Z.; Zhu, A. Y.; Li, Z.; Huang, Y.-W.; Chen, W. T.; Qiu, C.-W.; Capasso, F. Continuous Angle-Tunable Birefringence with Freeform Metasurfaces for Arbitrary Polarization Conversion. *Sci. Adv.* **2020**, *6* (23), eaba3367. https://doi.org/10.1126/sciadv.aba3367.

(137) Raider, S. I.; Flitsch, R.; Palmer, M. J. Oxide Growth on Etched Silicon in Air at Room Temperature. *J. Electrochem. Soc.* **1975**, *122* (3), 413–418. https://doi.org/10.1149/1.2134225.

(138) Morita, M.; Ohmi, T.; Hasegawa, E.; Kawakami, M.; Ohwada, M. Growth of Native Oxide on a Silicon Surface. *Journal of Applied Physics* **1990**, *68* (3), 1272–1281. https://doi.org/10.1063/1.347181.

(139) Evlyukhin, A. B.; Novikov, S. M.; Zywietz, U.; Eriksen, R. L.; Reinhardt, C.; Bozhevolnyi, S. I.; Chichkov, B. N. Demonstration of Magnetic Dipole Resonances of Dielectric Nanospheres in the Visible Region. *Nano Lett.* **2012**, *12* (7), 3749–3755. https://doi.org/10.1021/nl301594s.

(140) Nagasaki, Y.; Suzuki, M.; Hotta, I.; Takahara, J. Control of Si-Based All-Dielectric Printing Color through Oxidation. *ACS Photonics* **2018**, *5* (4), 1460–1466. https://doi.org/10.1021/acsphotonics.7b01467.

(141) Baek, K.; Kim, Y.; Mohd-Noor, S.; Hyun, J. K. Mie Resonant Structural Colors. *ACS Appl. Mater. Interfaces* **2020**, *12* (5), 5300–5318. https://doi.org/10.1021/acsami.9b16683.

(142) Taylor, S.; Zhang, J. F.; Eccleston, W. A Review of the Plasma Oxidation of Silicon and Its Applications. *Semicond. Sci. Technol.* **1993**, *8* (7), 1426–1433. https://doi.org/10.1088/0268-1242/8/7/037.

(143) DeCrescent, R. A.; Venkatesan, N. R.; Dahlman, C. J.; Kennard, R. M.; Zhang, X.; Li, W.; Du, X.; Chabinyc, M. L.; Zia, R.; Schuller, J. A. Bright Magnetic Dipole Radiation from Two-Dimensional Lead-Halide Perovskites. *Sci. Adv.* **2020**, *6* (6), eaay4900. https://doi.org/10.1126/sciadv.aay4900.

(144) Hum, S. Lorentz Reciprocity Theorem. In *Radio and Microwave Wireless Systems*; University of Ontario.

(145) Reciprocity Theorem; ECE 604; Purdue.

(146) Seo, I. C.; Lim, Y.; An, S.-C.; Woo, B. H.; Kim, S.; Son, J. G.; Yoo, S.; Park, Q.-H.; Kim, J. Y.; Jun, Y. C. Circularly Polarized Emission from Organic–Inorganic Hybrid Perovskites *via* Chiral Fano Resonances. *ACS Nano* **2021**, *15* (8), 13781–13793. https://doi.org/10.1021/acsnano.1c05421.

(147) Chen, Y.; Wang, T.; Li, Z.; Li, H.; Ye, T.; Wetzel, C.; Li, H.; Shi, S.-F. Communicating Two States in Perovskite Revealed by Time-Resolved Photoluminescence Spectroscopy. *Sci Rep* **2018**, *8* (1), 16482. https://doi.org/10.1038/s41598-018-34645-8.

(148) Sankaranarayanan, S.; Chouksey, S.; Saha, P.; Pendem, V.; Udai, A.; Aggarwal, T.; Ganguly, S.; Saha, D. Determination of Strain Relaxation in InGaN/GaN Nanowalls from Quantum Confinement and Exciton Binding Energy Dependent Photoluminescence Peak. *Sci Rep* **2018**, *8* (1), 8404. https://doi.org/10.1038/s41598-018-26725-6.

(149) Shibata, H.; Sakai, M.; Yamada, A.; Matsubara, K.; Sakurai, K.; Tampo, H.; Ishizuka, S.; Kim, K.-K.; Niki, S. Excitation-Power Dependence of Free Exciton Photoluminescence of Semiconductors. *Jpn. J. Appl. Phys.* **2005**, *44* (8R), 6113. https://doi.org/10.1143/JJAP.44.6113.

(150) He, H.; Yu, Q.; Li, H.; Li, J.; Si, J.; Jin, Y.; Wang, N.; Wang, J.; He, J.; Wang, X.; Zhang, Y.; Ye, Z. Exciton Localization in Solution-Processed Organolead Trihalide Perovskites. *Nat Commun* **2016**, *7* (1), 10896. https://doi.org/10.1038/ncomms10896.

(151) Reshchikov, M. A. Measurement and Analysis of Photoluminescence in GaN. *Journal of Applied Physics* **2021**, *129* (12), 121101. https://doi.org/10.1063/5.0041608.

(152) Zhou, Q.; Xu, M.; Wang, H. Internal Quantum Efficiency Improvement of InGaN/GaN Multiple Quantum Well Green Light-Emitting Diodes. *Opto-Electronics Review* **2016**, *24* (1), 1–9. https://doi.org/10.1515/oere-2016-0004.

(153) Albert, S.; Bengoechea-Encabo, A.; Sabido-Siller, M.; Müller, M.; Schmidt, G.; Metzner, S.; Veit, P.; Bertram, F.; Sánchez-García, M. A.; Christen, J.; Calleja, E. Growth of InGaN/GaN Core–Shell Structures on Selectively Etched GaN Rods by Molecular Beam Epitaxy. *Journal of Crystal Growth* **2014**, *392*, 5–10. https://doi.org/10.1016/j.jcrysgro.2014.01.030.

(154) Park, S. -H.; Liu, C.; Gu, E.; Dawson, M. D.; Watson, I. M.; Bejtka, K.; Edwards, P. R.; Martin, R. W. Membrane Structures Containing InGaN/GaN Quantum Wells Fabricated by Wet Etching of Sacrificial Silicon Substrates. *Phys. Status Solidi (c)* **2006**, *3* (6), 1949–1952. https://doi.org/10.1002/pssc.200565188.

(155) Tsai, S.-C.; Lu, C.-H.; Liu, C.-P. Piezoelectric Effect on Compensation of the Quantum-Confined Stark Effect in InGaN/GaN Multiple Quantum Wells Based Green Light-Emitting Diodes. *Nano Energy* **2016**, *28*, 373–379. https://doi.org/10.1016/j.nanoen.2016.08.061.

(156) Yuh-Renn Wu; Chinghua Chiu; Cheng-Yu Chang; Peichen Yu; Hao-Chung Kuo. Size-Dependent Strain Relaxation and Optical Characteristics of InGaN/GaN Nanorod LEDs. *IEEE J. Select. Topics Quantum Electron.* **2009**, *15* (4), 1226–1233. https://doi.org/10.1109/JSTQE.2009.2015583.

(157) Chen, H.-S.; Yeh, D.-M.; Lu, Y.-C.; Chen, C.-Y.; Huang, C.-F.; Tang, T.-Y.; Yang, C. C.; Wu, C.-S.; Chen, C.-D. Strain Relaxation and Quantum Confinement in InGaN/GaN Nanoposts. *Nanotechnology* **2006**, *17* (5), 1454–1458. https://doi.org/10.1088/0957-4484/17/5/048.

(158) Petelet, M.; Iooss, B.; Asserin, O.; Loredo, A. Latin Hypercube Sampling with Inequality Constraints. *AStA Adv Stat Anal* **2010**, *94* (4), 325–339. https://doi.org/10.1007/s10182-010-0144-z.